Seismic Modeling for Geothermal Reservoir Characterization

Annie Elisabeth Jerkins

Thesis for the degree
Master of Science

Department of Earth Science
University of Bergen
May 31, 2016

Abstract

The world's energy demand is increasing, and there is a need for alternative energy sources to replace depleting fossil fuels. Geothermal energy could be an important part of these new sources of energy. For efficient and reliable geothermal energy production, characterization of geothermal reservoirs is needed. Characterization of reservoir properties is for a large part obtained using geophysical methods. In this thesis I develop a new seismic modeling method that can be used in geothermal reservoir characterization.

In passive seismics the amount of seismic data obtained at a geothermal reservoir can be quite large. For example, at The Geysers in California, over a period of about 30 years, hundreds of thousands of microseismic events have been recorded by about a hundred receivers. Efficient seismic modeling using, for example ray tracing, is therefore essential. In this thesis the main focus was on ray tracing. The goal was to develop a ray tracing algorithm, that is both fast and accurate. Ray tracing was implemented using three different numerical methods: Euler's method, the midpoint method and fourth order Runge-Kutta. From a systematic comparison for realistic geothermal reservoir models and their overburdens, it was found that the midpoint method with a small time step is the preferred numerical method.

When performing ray tracing for e.g. source characterization it is essential to have reliable seismic velocity models. In this thesis an overview of velocity models at 15 enhanced geothermal systems was made. 1D velocity models exist at almost all the geothermal reservoirs. However, 3D velocity models, which tends to be much more accurate, only exist for half of these reservoirs. In this thesis the ray tracing algorithms were used for efficient waveform modeling, using both 1D and 3D velocity models, in order to check trade-offs in terms of travel times, amplitudes and waveforms. The velocity models used were a 1D velocity model of the The Geysers as given in the literature. The 3D model consisted of this 1D model on which were superimposed 3D perturbations. The modeling was done using two different seismic sources: a double couple source and a non-double couple source. The results showed that there were significant differences between the 1D and 3D modeling. The most significant deviations were differences in amplitudes and amplitude polarities for the calculated synthetic seismograms. Also, it was found that the results depend upon the seismic source, where there were large differences between the double couple and

non-double couple source. Thus, the use of 1D velocity models for geothermal reservoir characterization, can lead to wrong results about permeability of fractures. It is recommended that 3D seismic velocity models are used, and if necessary developed, when studying microseismicity and especially when inverting for source mechanisms.

Acknowledgements

First of all I would like to give a special thanks to my supervisor associate professor Henk Keers. This thesis could not have been written without you.

Further, I would like to thank my cosupervisor professor Inga Berre for the helpful ideas and expertise on geothermal energy.

Also, my fellow students have been important when writing this thesis. The lunch breaks, cheap exam dinners and cake fridays have made my time as a student unforgettable.

I would also like to express my gratitude to my roommates Stine, Dersim and Vera during my time as a master student. You have helped me relax during stressful times.

Last but not least I would like to thank my mom, dad and twin sister Katinka. You have always supported me.

Contents

1 Indroduction

The world's energy demands are increasing, while CO_2 emissions and climate change are still as big a problem as ever. Today, the main sources of energy are coal and natural gas as shown in Figure 1. The figure also shows the world's power generation between 1970 and 2010, and contains a prediction on how the energy consumption is expected to increase until 2030.

The depleting hydrocarbon resources, as well as the rapidly growing population and global warming increase the need for alternative energy sources to replace fossil fuels (Ehrlich 2013). Ehrlich (2013), as well as other reports by MIT (2006) and BP (2013) therefore suggest that much of the energy demand in the future should be covered by renewable sources of energy.

Renewable energy is energy provided by natural resources, which can be regenerated over a short period of time. Renewable energy can for example be from sources relying on the sun (e.g. solar, wind, hydropower, ocean and biomass) or from other natural processes such as tides (tidal energy) and the Earth's heat (geothermal energy). Geothermal energy can continuously supply energy without being affected by external factors (Ehrlich 2013). In 2006 a group of scientists at MIT (Massachusetts Institute of technology) wrote a report called "The future of geothermal energy". This report provides detailed information on how technology development and investments in geothermal energy production might help cover the future energy demands and suggests that the geothermal energy resources are enormous. However, in order to efficiently produce geothermal energy in large quantities over a long period of time still a large amount of research is needed. In particular, more detailed characterization of geothermal reservoirs is needed. This is in a large part obtained using geophysical and especially seismic methods. The main focus of this thesis is to further develop seismic methods for geothermal reservoir characterization.

World power generation

Thousand TWh

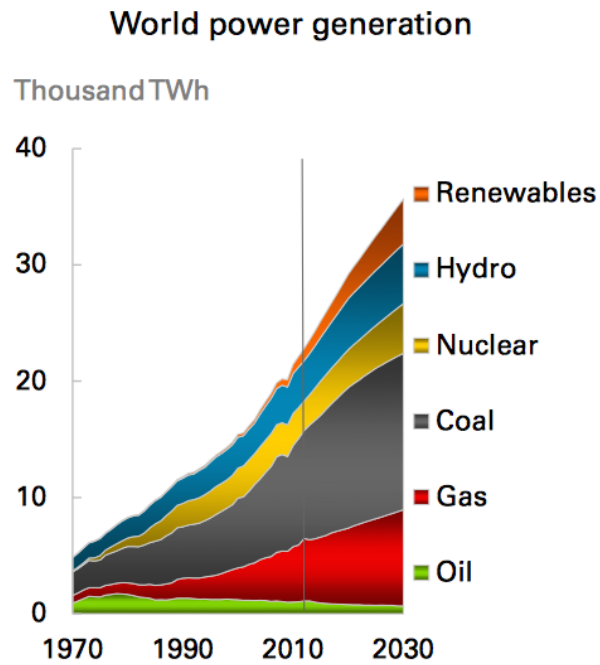- Renewables
- Hydro
- Nuclear
- Coal
- Gas
- Oil

Figure 1: This figure shows how energy demands are expected to increase until 2030. From the figure it can be seen that fossil fuels clearly dominate the current energy consumption (red, green and black). Also, it can be seen that one expects an increase in renewable energy (orange). The figure is retrieved from the BP energy outlook 2030 report.

1.1   Geothermal Systems

1.1.1   Definition

A geothermal field is an area below the Earth's surface with significant thermal energy reserves. The heat can, for example, come from magmatic intrusions or decay of radioactive elements (e.g. Thorium, Uranium and Potassium). Thermal energy of a geothermal field is distributed between fluids natural occurring in pores and fractures, and the host rock. The fluid most often is water in either fluid or steam phase (or both), depending on temperature, or magma (Tester et al. 2005).

Geothermal resources have been in use for a long period of time, even before recorded history (e.g. for hot baths and cooking). Geothermal energy production on the other hand, was first utilized at Lardarello (Italy) in 1902 (Tester et al. 2005). For geothermal energy production one wants to exploit the stored thermal energy in the Earth's crust. This is done using fluid/steam that is naturally occurring or using an injected fluid, both of which are heated by the geothermal field. By drilling wells the heated water/steam can be extracted, and is used to drive turbines in a power plant. The turbines produce electricity (MIT 2006).

Geothermal energy resources are usually divided into four different categories: magmatic, geopressured systems, enhanced geothermal systems and hydrothermal (Tester et al. 2005).

In the case of magmatic systems one exploits energy directly from magma. This is challenging because instruments need to be able to withstand extremely high temperatures. Currently, there is only one magmatic geothermal energy field in the world. This system is in Iceland, and was first utilized in 2014 (Scott et al. 2015). Geopressured systems are systems where the confining pressure is larger than the hydrostatic pressure. This is often the case when water is trapped under an impermeable layer, with a thick layer of sediments on top. The heavy weight of the sediments increases the pressure. The advantage of these high pressures is that not much energy is needed for pumping during the production. An example of such a system is in Texas. The system was utilized between 1989-1990 (U.S department of energy 2010). The two other types of systems, the focus of this thesis, will be discussed in more detail in the next two subsections.

1.1.2 Hydrothermal Systems

Hydrothermal systems are ideal for geothermal energy extraction. These systems have high permeability, large amounts of stored heat and sufficient recharge of natural water. Figure 2 shows a typical hydrothermal system. The reservoir is a confined aquifer, where an impermeable layer keeps the heat trapped in the reservoir. Also, for the hydrothermal system sketched in the figure, heat is continuously supplied from a magmatic intrusion beneath the reservoir. This is often the case for hydrothermal systems. Because of the magmatic intrusions hydrothermal reservoirs are usually shallow, making it easy to access the stored thermal resources (Tester et al. 2005).

Hydrothermal reservoirs are most commonly found close to plate boundaries. Plate boundaries are often associated with faults and fractures, giving relatively high permeability. These faults also often provide a travel path between the surface and reservoir, helping the reservoir to recharge from natural sources, such as precipitation, as seen in Figure 2. Water can also be recharged through fissures and sediments.

Examples of hydrothermal systems are The Geysers in California, Larderello in Italy, Wairakei in New Zealand, Hellisheidi in Iceland and Matsuwaka in Japan (Tester et al. 2005).
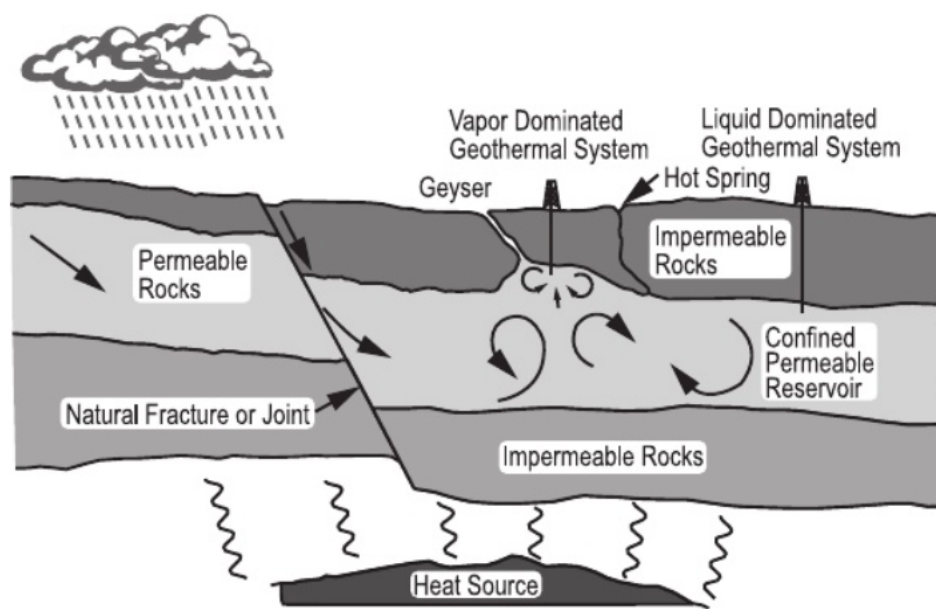
Figure 2: A typical hydrothermal system. Retrieved from Tester et al. (2005).

1.1.3 Enhanced Geothermal Systems

Well drilling related to oil, gas and geothermal energy extraction shows that the largest geothermal resources available often occur in areas with relatively low permeability, or absence of natural water recharge. Permeability and fluid flow are crucial for the extraction of geothermal energy, and the absence of one of these properties makes it difficult to access the stored thermal resources. However, In 1974 Los Alamos National Laboratory developed techniques, which made it possible to extract energy from such areas. These technologies were first tested at Fenton hill in New Mexico, and showed great potential (MIT 2006).

The concept is built on drilling a well (injection well) to reach rocks with a certain temperature. Once the well is drilled, permeability is created by hydraulically fracturing the rock (or stimulating the natural fracture system) as shown in Figure 3. This can for example be done, injecting large amounts of water through the injection well to increase pressure. Once pressure is above a certain level, fractures are created/stimulated. More wells (production wells), intersecting the fracture system, are often also drilled. Water circulation in the hot rock fracture system between the injection and production well heats the water. The heated water/steam is further extracted through the production well, and used to drive turbines in a power plant. This kind of system is called an enhanced geothermal system (EGS). Enhanced geothermal systems drastically increase the number of possible geothermal energy production sites (MIT 2006).

In 2013 worldwide there were 31 EGS projects, and the number is increasing (Breede et al. 2013). Figure 4 shows 25 of the projects as well as their depths and temperatures. Most of the projects are located in Europe. The projects in Europe have a much lower temperature, than projects in America, Australia and Asia (Breede et al. 2013). EGS systems are the main focus of this thesis and are therefore discussed in more detail in the next three subsections.
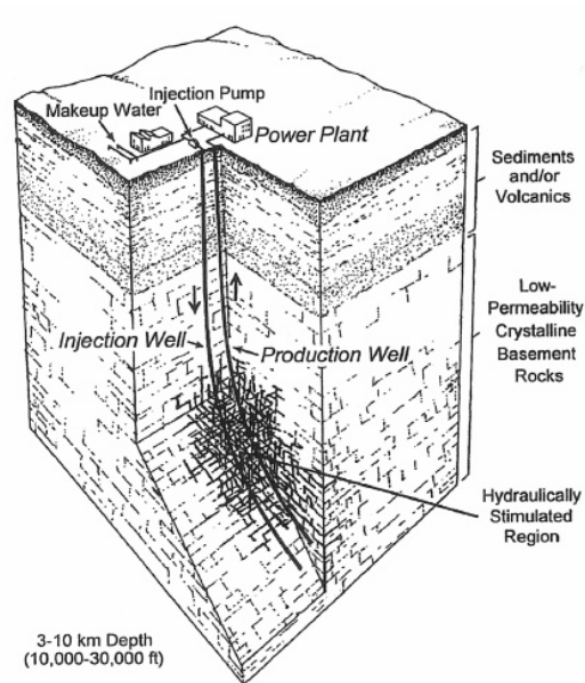
Figure 3: An enhanced geothermal (EGS). By hydraulically fracturing the rock, permeability is improved. Retrieved from Tester et al. (2005).
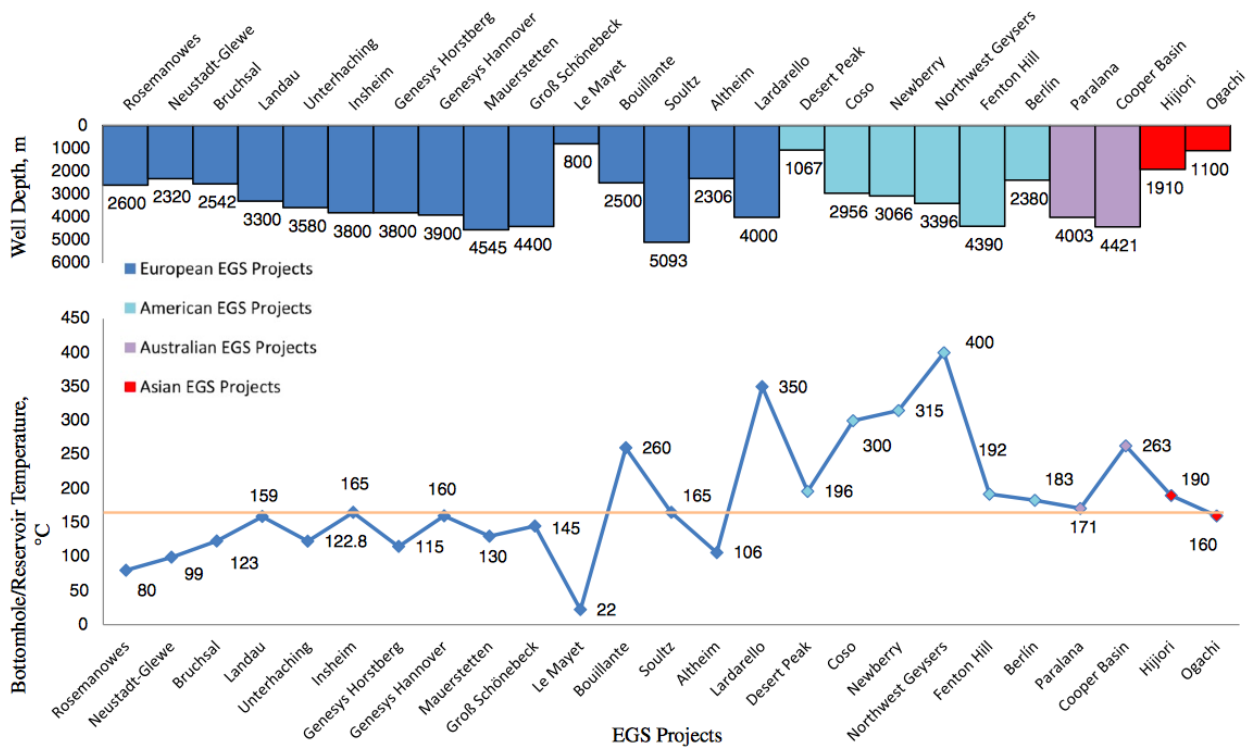
Figure 4: The figure shows both temperature and well depths of most EGS systems. The yellow line shows the average temperature. Retrieved from Breede et al. (2013).

1.2   Reservoir Potential and Lifetime

1.2.1   Geothermal Energy Potential

When considering potential geothermal energy reservoirs, it is essential that the geothermal field produce enough energy to be profitable. Hence, it is important to be able to calculate the energy potential of the reservoir.

Estimation of geothermal energy potential (H_G) from a geothermal field can be done using the following equation (Bundschuh & Arriga 2010):

$$H_G = \rho_s c_p V_b \Delta T. \tag{1.1}$$

Here c_p is heat capacity of the rock (the amount of energy that is needed to raise a volume of rock of $1cm^3$ by 1 degree Celsius), ρ_s is the rock density, V_b is rock volume (including pores) and ΔT is the temperature difference within the reservoir. An example illustrating the large potential of geothermal energy is given in the MIT report using equation (1.1).

If both the width and length of the rock are 14km, and the rock thickness is 1km, assuming an initial temperature of $250\,^{\circ}C$, which is lowered, due to production, to a temperature of $50\,^{\circ}C$ ($\Delta T = 200\,^{\circ}C$), and if the average density is assumed to be $2550\frac{kg}{m^3}$ and with a heat capacity of $1000\frac{J}{kg\,^{\circ}C}$. Then the potential reservoir energy is (MIT 2006):

$$H_G = (2550\frac{kg}{m^3})(1000\frac{J}{kg\,^{\circ}C})(14km \times 14km \times 1km)(200\,^{\circ}C) = 100 \times 10^{18}J \tag{1.2}$$

This is more energy than is consumed every year in the United States. Even though potentially only a small amount ($< 10\%$) of the calculated energy is accessible, this number shows the enormous potential for geothermal energy (MIT 2006).

1.2.2   Recovery Time

Recovery time of a geothermal system is the time the geothermal field would use to recover back to its original state after energy production is ended, while the lifetime of a geothermal system describes how many years energy can be extracted from a reservoir before it becomes unprofitable (MIT 2006).

If too large amounts of heat are extracted from the reservoirs, the recovery time of geothermal systems are considerably longer than for other source of renewable

energy (e.g. solar, wind or biomass), and in some cases might be as large as a 100 years (MIT 2006). However, if energy is extracted at low rates, the systems has time to recover, extending the lifetime of the reservoir significantly. If as much heat is extracted as regenerated by natural processes the system could in theory produce energy for millions of years (Ehrlich 2013). The lifetime also depends upon the characteristics of the reservoir. Some areas use longer time to recover than other areas. For example at the Larderello field in Italy some wells have been producing energy for over 70 years, while other wells only last a few years (Tester et al. 2005).

1.3   Challenges Related to Geothermal Energy

Even though geothermal energy provides great potential, there are many challenges related to EGS (and hydrothermal systems), and success is not guaranteed. Many of the challenges lie in the extremely hot environment and large depths at which one extracts geothermal energy.

1.3.1   Instrumentation and Drilling Issues

For geothermal areas instruments and technology need to be able to withstand high temperatures, deep depths (i.e. high pressures) and high salinity levels/corrosion. Currently, instruments from the oil and gas industry are often used. However, since hydrocarbons are produced under less challenging conditions (lower depths and temperatures) development of instruments adapted for geothermal settings is needed (MIT 2006).

For example for temperatures above $225°C$, imaging tools used to gain information on fractures and the stress regime do not exist. This makes it difficult to image the reservoir without pre-cooling the borehole. Drilling wells related to geothermal energy are expensive, and accounts for approximately 60% of initial investments. The rest of the investments are usually used for building the power plant (Ehrlich 2013). The major expense of the drilling costs lies in the large depths at which a well needs to be drilled to reach rock with the correct temperature, especially for enhanced geothermal systems. As one goes deeper, the reservoir gets hotter, increasing the risk of the drill bit getting stuck and being significantly worn. If in the worst case the bit is worn, the time associated with changing the bit is long, since it first has to be hauled out from the deep bore hole. Another difficulty is removing debris from the borehole, which has to be transported to the Earth's surface (Ehrlich 2013).

Table 1 shows an overview of well depths, production wells and injection wells for

15 EGS systems. From the table it can be seen that the depth interval at which the reservoirs produce is 1067-5093m. Also, the number of wells at each EGS varies. At Genesys-Hannover a combined well which works as both production and injection well is used (Breede et al. 2013).

EGS	Well depth	Production wells	Injection Wells
Rosemanowes	2600m[1]	-	-
Landau	3300m[1]	1[5]	1[5]
Soultz	5093m[1]	2[6]	1[6]
Basel	5000m[2]	2[2]	1[2]
Coso	2956m[1]	-	-
Berlin	2380m[1]	8[4]	10[4]
Cooper-Basin	4421m[1]	-	-
Genesys-Hannover	3900m[1]	1[6] (Production+ injection well)	0
NorthWest Geysers	3396m[1]	3[8]	2[7]
St.Gallen	4450m[1]	-	-
Insheim	3800m[1]	1[9]	2[3]
Groß-Schönebeck	4400m[1]	-	-
Paralana	4003 m[1]	-	-
Larderello	4000m[1]	-	-
Desert Peak	1067m[1]	-	-

Table 1: Table showing maximum well depth and number of wells used for injection and production related to EGS. The "-" sign indicates that no studies were found. In Genesys-Hannover a single well concept is tested, using the same well as both production and injection well (Breede et al. 2013).

References: 1: (Breede et al. 2013) 2: (Häring et al. 2007) 3: (Kwiatek et al. 2012) 4: (Monterrosa, M. 2012)

5: (Heimlich et al 2015) 6: (Fritsch & Lutz 2006) 7: (Johnson 2014) 8: (Garcia et al. 2012)

1.3.2   Seismic Reflection and VSP Surveys

Seismic reflection studies can be performed at geothermal reservoirs. The reasons for doing these studies vary. For example, for geothermal energy extraction of seismic reflection data can be used to map the main structures of the geothermal field, giving an indication on where wells should be placed to make the reservoir commercially feasible. Acquisition of seismic reflection data at geothermal areas is more challenging than for the oil and gas industry. One problem is related to the large depths at which one extracts geothermal energy. Mapping deeper structures require larger offsets, which is often a challenge. If the offsets are not large enough then this results in low resolution images. Also, often geothermal areas are more complex than areas used for oil and gas extraction. This is mainly due to the large fracture system used for geothermal energy extraction, but can also be due to a heterogeneous overburden (Majer 2003).

Reflection seismic data for investigation of geothermal reservoirs is expensive, and often not performed (if these techniques first are performed success is not guaranteed). 4D reflection seismics could theoretically be used to investigate possible changes of reservoir properties with time (e.g. pressure, heat and porosity), but is also often considered to be too expensive. High temperatures and presence of steam might also affect the resolution in a negative manner, but are not as significant as problems related to depth and structural/reservoir complexity (Crosby & Calman 1996).

Since it is often difficult to perform high resolution seismic refection surveys at geothermal fields, VSP (Vertical seismic profiles) are often used to gain important information close to boreholes. For a VSP investigation geophones are located inside the borehole and a seismic source at the surface close to the well is used. The main goal is to image fractures and possible permeable zones close to the well. The VSP can also be used to test the accuracy of the velocity model and may also give a better indication when interpreting results obtained from seismic reflection acquisition. Results for VSP are varying, for example at the Soultz geothermal field VSP gave disappointing results due to the difficult granite environment. Moreover, the image quality of VSP is relatively low compared to reflection seismics because of lack of illumination. VSP are also rarely performed due to the high costs (DECC 2013).

Table 2 shows seismic studies done on 15 EGS systems. From the table it can be seen that reflection studies and VSP were only done at approximately half of the EGS systems, and are in most cases only performed once. In the table "yes" shows successful studies (managed to map structures), while "no" indicates unsuccessful

studies.

EGS	Refl. seismics	VSP	1D vel. model	2D/3D vel. model
Rosemanowes	yes[19]	yes[19]	-	-
Landau	-	-	x[12]	-
Soultz	yes[16]	no[11]	x[2]	x(3D)[2] (tomography)
Basel	-	yes[20]	x[3]	x(3D)[3] (reflection)
Coso	yes[17]	-	x[4]	x(3D)[4] (tomography)
Berlin	-	-	x[15]	-
Cooper-Basin	yes[18]	yes[21]	x[14]	-
Genesys-Hannover	-	-	-	-
The Geysers	yes(Not EGS)[6]	no[22]	x[1]	x(3D) [5] (tomography)
St.Gallen	yes[23]	-	x[7]	-
Insheim	-	yes[12]	x[12]	-
Groß-Schönebeck	yes[8]	-	x[8]	x(2D)[8] (tomography/reflection)
Paralana	-	-	x[9]	x(3D)[9] (tomography)
Larderello	unknown[11]	yes[24]	x[10]	x(3D)[10] (tomography)
Desert Peak	yes[13]	yes[25]	-	-

Table 2: Table showing seismic studies done on EGS (Enhanced geothermal systems).
I chose to only look at the EGS systems where the largest seismic events are known,
see Figure 5. In the table "x" indicates that there exists velocity models for the
systems, while the "-" sign indicates that no velocity models were found. Also, for
the reflection seismic data and VSP: "yes" indicates successful studies, while "no"
indicates unsuccessful studies.

References: 1: (Guilhem et al. 2014) 2: (Charlety et al. 2006) 3: (Kind et al. 2001) 4: (Yang et al. 2010)

5: (Hutchings et al. 2014) 6: (Denlinger & Kovach 1981) 7: (Oberman et al. 2015) 8: (Bauer et al. 2010) 9: (Oye et al. 2012)

10: (Matteis et al. 2003) 11: (DECC 2013) 12: (Küperkoch 2014) 13: (Drakos 2010) 14: (CRIEPI 2006)

15: (Kwiatek et al. 2012) 16: (Place et al. 2008) 17: (Unruh et al. 2001) 18: (Khair et al. 2015) 19: (Baria 2012)

20: (Häring et al. 2008) 21: (Asanuma et al. 2005) 22: (Majer et al. 1988) 23: (Hirschberg et al. 2015) 24: (Brogia et al. 2003)

25: (Davatzes et al. 2013)

1.3.3   Production Induced Changes

Rock-fluid interactions during production can lead to unwanted changes in reservoir properties. As a result of long term operations at a geothermal field, dissolution and precipitation of minerals often changes the connectivity between fractures as well as permeability of the individual fractures. These changes can lead to short-circuiting of fractures, hence reducing the residence time of water in the fractures, giving the water less time to heat. These changes are crucial, and can even change the commercial viability of the reservoir (MIT 2006).

Too high water injection rates can also lead to short-circuiting. Pressures higher than critical pressure for fracture growth can extend the reservoir beyond the desired reservoir region. Due to these changes, there is a large chance of water circulation in non-productive regions within the reservoir, reducing the amount of energy produced. Therefore, it is useful to manage the water injection rates to reduce the risks of short-circuiting. Currently, there is no method developed to repair short circuits (MIT 2006).

1.3.4   Hazards and Environmental Problems

Another concern is contamination of groundwater, which for example is used as drinking water. Still in most cases no harmful chemicals are used for EGS exploitation. Also for deep geothermal systems, fractures related to the reservoir rarely interact with groundwater systems, which reduce the probability of pollution (Breede et al 2013).

Yet another concern is related to dissolution of radioactive elements from rocks. This is more likely to occur in the case of hot environments. High concentrations of radioactive elements may therefore be present in the fluid, which can lead to health and environmental issues. These numbers are however small compared to radioactivity related to exploitation of oil and gas (Breede et al. 2013).

Subsidence is another known problem connected to geothermal reservoirs. If fluid injection rates are lower than the extraction rate, consolidation of rock might occur, which leads to lowering of the surface (subsidence) (MIT 2006). Subsidence occurred at the Wairakei geothermal field in New Zealand, where reinjection was not performed after extracting geothermal energy. At one area of the field, the subsidence rates were as high as 0.45m per year. In order to avoid subsidence, one should therefore inject water into the reservoir to maintain reservoir pressure (MIT 2006).

A disadvantage of water injection is that it can cause micro-seismicity. A project in Basel (Switzerland) was stopped due to concerns from the population when a magnitude 3.4 event occurred. The largest event recorded at an EGS system was for the Berlin project in El Salvador. The event had a magnitude of 4.4 on the Richter scale (Breede et al. 2013). An overview of the largest events recorded at enhanced geothermal systems is given in Figure 5. Table 3 shows an overview of micro-seismicity recordings at 15 EGS systems (both induced and natural seismicity). The table shows that induced seismicity monitoring exists at most EGS systems. Also, we see that there is no recorded induced micro-seismicity at Genesys-Hannover and Groß-Schönebeck.
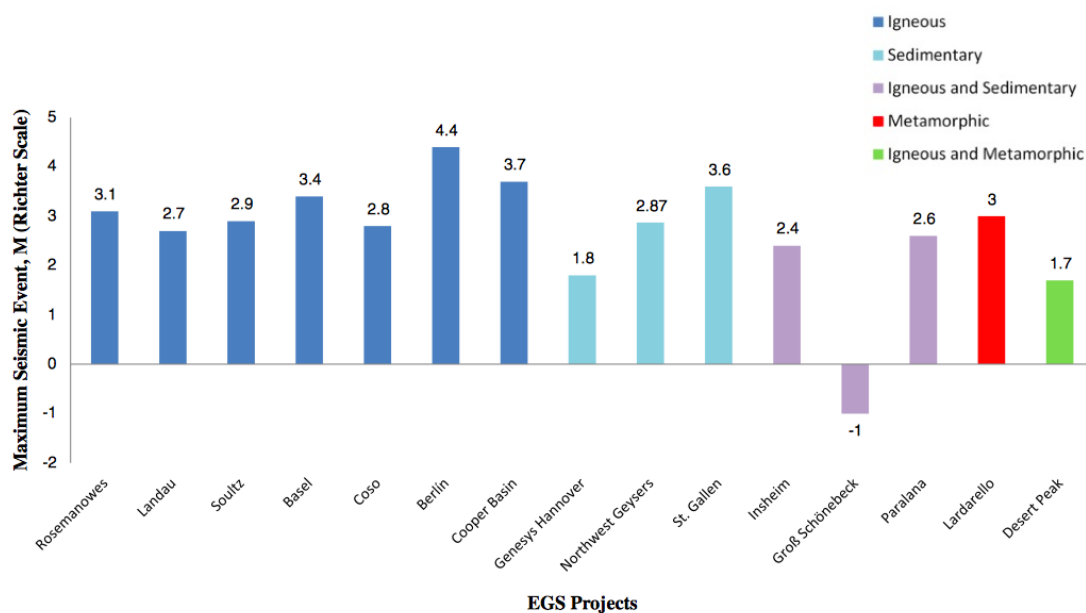

Figure 5:   An overview of the largest microseismic events recorded at the different EGS projects. The different colors represent rock type in the reservoir. In the figure one event has the magnitude -1. This is possible when using the Richter scale. Retrieved from Breede et al. (2013).

EGS	Induced Seismicity	Natural Seismicity	Largest event
Rosemanowes	-	x[15]	3.1[10]
Landau	x[9]	Production stopped[16]	2.7[16]
Soultz	x[6]	-	2.9[10]
Basel	x[1]	Production stopped[10]	3.4[10]
Coso	x[7]	-	2.8[10]
Berlin	x[5]	-	4.4[10]
Cooper-Basin	x[6]	-	3.7[10]
Genesys-Hannover	No observed induced seismicity[12]	x[12]	1.8[10]
NorthWest Geysers	x[3]	x[3]	2.87[10]
St.Gallen	-	-	3.6[10]
Insheim	x[4]	x[4]	2.4[16]
Groß-Schönebeck	No observed induced seismicity[10]	x[10]	-1[10]
Paralana	x[2]	-	2.6[10]
Larderello	x[14]	x[14]	3[10]
Desert Peak	-	x[13]	1.7[10]

Table 3: Table showing for which EGS systems natural and induced events are measured. The largest events are measured using the Richter scale. "x" indicates found studies, while − indicates no studies. For Groß-Schöenbeck and Genesys-Hannover no induced seismic events have been recorded. The table also shows the largest recorded events.

References: 1: (Häring et al. 2007) 2: (Oye et al. 2012) 3: (Guilhem et al. 2014) 4: (Küperkoch 2014)

5: (Kwiatek et al. 2012) 6: (Cuenot et al. 2008) 7: (Feng & Lee 1998) 8: (Asanuma et al. 2005) 9: (Vasterling et al. 2016)

10: (Breede et al. 2013) 11: (Kwiatek et al. 2010) 12: (Bischoff et al.2012) 13: (Drakos 2010) 14: (Batini et al 1985)

15: (Cornwall Council 2012) 16: (Gross et al. 2013) 17: (Heimlich et al 2015)

1.4   Micro-Seismicity and Seismics

As mentioned in the last subsection, injection of fluids into the subsurface and exploitation at geothermal fields cause microseismic activity. Micro-seismicity of a geothermal field can be a hazard, but also of great interest. It can be used for geothermal reservoir characterization (e.g. Guilhem et al. 2014).

It is important to distinguish between naturally occurring seismicity and induced seismicity. At the north west of The Geysers geothermal field in California, the abandoned Prati-32 well was reopened in 2010. Water was injected into the well at different rates. The project showed a clear connection between water injection and the number of micro-seismic earthquakes (Johnson 2014). Results from this injection experiment are displayed in Figure 6. Prior to injection there is only a small amount of naturally occurring events up to about 5 a day, with an isolated peak of 12 events on one day. When the injection rates are increased the number of micro-seismic events increases significantly to about 10-20 a day.
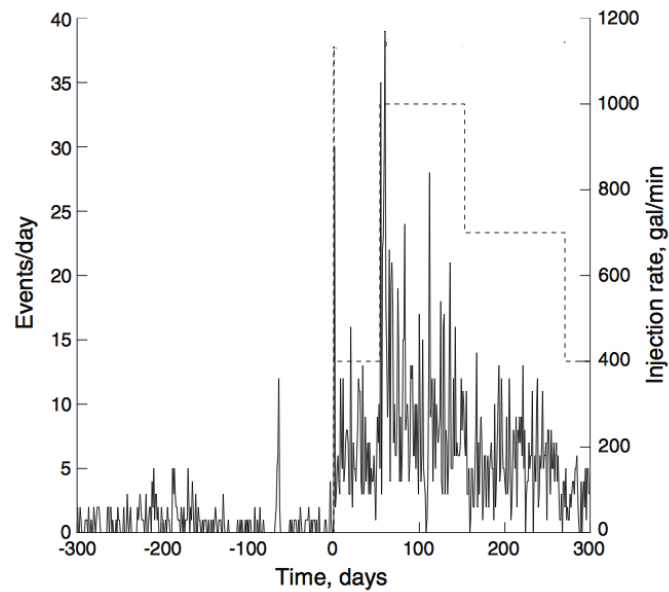
Figure 6: This figure shows the connection between micro-seismicity and water-injection. On the x-axis days are displayed. The minus sign indicate days prior to injection. Number of microseismic events are displayed on the y-axis at the left, while injection rates are displayed on the y-axis at the right. Modified figure from Johnson (2014).

1.4.1   Seismic Tomography

Tomography mainly uses travel times of seismic waves from micro-seismic earthquakes to gain information on reservoir and overburden properties. If enough microseismic events are recorded and processed, it is possible to make 3D models of for example velocity models and attenuation (Hutchings et al. 2014). From table 2 it can be seen that for only about half of the EGS systems 3D velocity models are available. This indicates that tomography studies are not always performed at geothermal systems.

An example of seismic tomography is given by Hutchings et al. (2014). At The Geysers Hutchings et al. (2014) performed tomography using the microseismic earthquakes related to the Prati-32 injection test. The main goal was to investigate difference in reservoir properties before and during injection for P and S-wave velocity, Possion's ratio, P- and S wave attenuation (Lamés second constant and bulks modulus). Figure 7 shows results from the P-wave tomography. It can be seen that there is a decrease in velocity close to the well after performing water injection for two months.
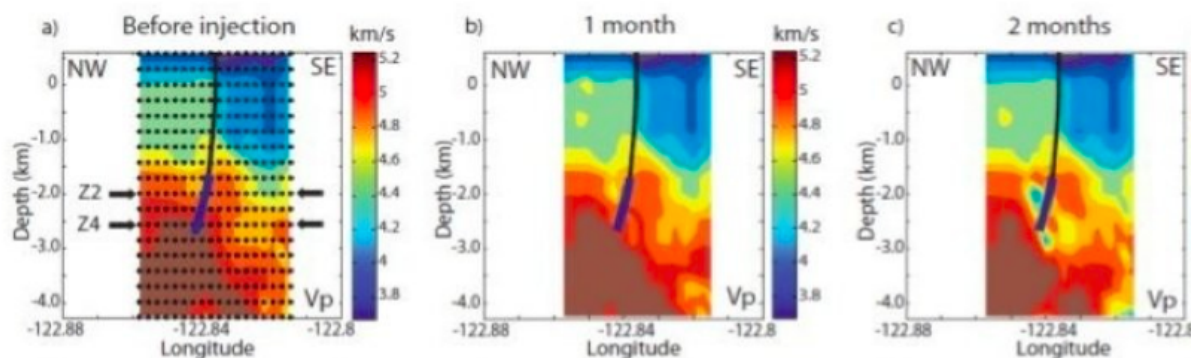

Figure 7: P-wave tomography results performed for the Prati-32 injection test. Retrieved from Hutchings et al. (2014).

1.4.2   Moment Tensor Inversion

The forces acting on fractures of microseismic earthquakes at geothermal fields can be found using moment tensor inversion. Moment tensors give the fault/fracture orientation and slip direction by calculating a corresponding focal mechanism. Moment

tensor inversion is also used to find seismic moment, which helps estimate moment magnitude (Stein & Wysession 2003). By calculating moment tensors in combination with earthquake locations for microseismic events at geothermal reservoirs, it is possible to predict possible permeable zones and orientation of fractures. Johnson (2014) investigated micro-seismic earthquakes related to fluid injection at the northern area of The Geysers geothermal fields in California. By investigating different moment tensors he made a source model for induced earthquakes. The source model aimed at predicting whether fractures are being opened or closed.

1.5   Contents of this Thesis

This thesis will go into further depth on moment tensor inversion and different aspects of waveform modeling as discussed in the previous sections. In order to estimate moment tensors one needs recorded seismograms (ground displacement) and Green's tensors in elastic media. Green's tensors represent the impulse response of the velocity model, and can be estimated using ray tracing.

The main focus of this thesis is ray tracing. At The Geysers geothermal field in California, 1D ray tracing is used when estimating moment tensors. However, the velocity model is known to be 3D. Therefore 3D modeling, rather than 1D modeling is needed. A crucial part of 3D (elastic isotropic) seismic waveform modeling is done using ray tracing. Therefore, I have developed 3D ray tracing algorithms, which can be used for heterogeneous 3D media. I also investigate trade of between 1D and 3D ray tracing, to see if there are any major differences in obtained results.

Most ray tracing algorithms are performed using a numerical method called fourth order Runge-Kutta. In this thesis I implement the fourth order Runge-Kutta method, but I also implement ray tracing using two other numerical methods: Euler and mid-point method. A systematic comparison between the 3 ray tracing methods is done. These methods will be compared in terms of accuracy and numerical costs.

Finally, I use the ray tracing to compute seismic waveforms for a synthetic model of a geothermal reservoir and in particular look at differences between 1D and 3D modeling and the effect of these models on different seismic sources. Chapter 2 gives a summary of the wave theory of seismic wave propagation. Chapter 3 gives a detailed overview of the 3 ray tracing algorithms. The ray tracing algorithms are then

compared in detail in Chapter 4. For the comparison 3 velocity models of geothermal reservoirs and its overburden were used: one 1D and 2 3D models. The ray tracing is then used in Chapter 5 to compute seismic waveforms for the velocity models and study differences in the modeling.

2 Theory: Seismic Wave Propagation

2.1 Overview

Seismic forward modeling is used to compute travel times, amplitudes and whole waveforms. These waveforms provide valuable information for structure and sources (e.g. moment tensor inversion). Therefore, in this chapter I discuss theory related to seismic wave propagation. This is important for understanding the concepts used in this thesis.

2.2 Acoustic Wave Propagation

Seismic waves are best modeled using elastic wave theory (see e.g. Aki & Richards (1980), Ben-Menahem & Singh (1981) and Chapman (2004)). However, several important aspects of elastic wave propagation and the much simpler acoustic wave propagation are very similar. Therefore, in this section I discuss acoustic wave propagation.

The acoustic wave equation describes how the pressure field U behaves away from a source S (see e.g. Morse & Feshbach (1953), DeSanto (1992)) and is given by:

$$\Delta U(\mathbf{x}, t) - \frac{1}{c^2(\mathbf{x})} \frac{\partial^2 U(\mathbf{x}, t)}{\partial t^2} = -S(\mathbf{x}, t). \tag{2.1}$$

Here $\mathbf{x}$ is the position vector. Its Cartesian coordinates will be denoted by (x, y, z) or (x_1, x_2, x_3) in this thesis. t is time, $c(\mathbf{x})$ is velocity at $\mathbf{x}$ and Δ is the Laplace operator. The source satifies $S(\mathbf{x}, t) = 0$ for $t < 0$. To solve the acoustic wave equation (2.1) some initial conditions are needed, such as the pressure field $U(\mathbf{x}, 0)$ and its first time derivative $\frac{dU(\mathbf{x}, 0)}{dt}$. In this thesis, as in seismology/seismics in general, one wants to solve equation (2.1), i.e. find $U(\mathbf{x}, t)$ for given $\mathbf{x}$ and all t for a given velocity c and source S. This is called seismological/seismic modeling.

It is convenient first to choose S to be a point source in space and time:

$$S(\mathbf{x}, t) = \delta(\mathbf{x} - \mathbf{x}_s)\delta(t). \tag{2.2}$$

Here $\mathbf{x}_s$ is the source of the pressure field and δ is the Dirac-delta function. For our purposes the Dirac-delta function is zero everywhere, except at $t = 0$, when the function value is one. This is represented as a spike in Figure 8.
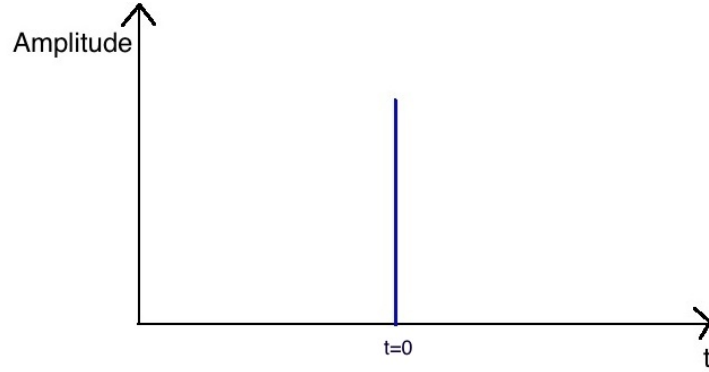
Figure 8: The Dirac-delta function is zero, except at $t = 0$. This is presented as a spike in the figure.

The solution of the acoustic wave equation (2.1) for a delta-function source, as in (2.2) is called the Green's function G and it satisfies:

$$\Delta G(\mathbf{x}, t) - \frac{1}{c^2(\mathbf{x})} \frac{\partial^2 G(\mathbf{x}, t)}{\partial t^2} = -\delta(\mathbf{x} - \mathbf{x}_s)\delta(t). \tag{2.3}$$

Once the Green's function is known, it can be used to express the solution of a general source $S(\mathbf{x}, t)$ using superposition:

$$U(\mathbf{x}, t) = \int G(\mathbf{x}, \mathbf{x}_s, t)S(\mathbf{x}, t)d\mathbf{x}_s dt. \tag{2.4}$$

It is often useful to express the wave equation in the frequency domain instead of the time domain. This is done by applying a Fourier transform to U:

$$f(\omega) = \int F(t)e^{i\omega t}\, \mathrm{d}t \leftrightarrow F(t) = \frac{1}{2\pi} \int f(\omega)e^{-i\omega t}\, \mathrm{d}\omega, \tag{2.5}$$

where $\omega = 2\pi f$ is angular frequency.
Applying a Fourier transform to the wave equation (2.1) gives the Helmholtz equation:

$$\Delta u(\mathbf{x}, \omega) + \frac{\omega^2}{c^2(\mathbf{x})} u(\mathbf{x}, \omega) = -S(\mathbf{x}, \omega). \tag{2.6}$$

2.2.1 Eikonal and Transport Equation

As noted in the previous section it is important to be able to solve the wave equation (2.1) for a general source S and velocity c. For a homogeneous medium this can be

done analytically and this gives (e.g. Cerveny 2001):

$$G(\mathbf{x}, t) = \frac{1}{4\pi|\mathbf{x} - \mathbf{x}_s|} \delta\left(t - \frac{|\mathbf{x} - \mathbf{x}_s|}{c}\right), \tag{2.7}$$

with $T = \frac{|\mathbf{x} - \mathbf{x}_s|}{c}$ the travel time and $\frac{1}{4\pi|\mathbf{x} - \mathbf{x}_s|}$ is the amplitude A. For a general heterogeneous medium exact analytical methods do not exist and solving the wave equation is done using fully numerical solutions (such as finite difference, finite element or pseudo spectral elements) or using approximate methods such as asymptotic and scattering or a combination of the two in combination with numerical methods (e.g. Cerveny 2001).

In this thesis the focus will be on a very popular approximate method: ray theory. In ray theory one assumes that:

$$g = Ae^{i\omega T}, \tag{2.8}$$

where ω is large. Note the similarity between equation (2.8) and the Green's function for a homogenous medium (2.7): one still assumes that there is a travel time T and amplitude A, which describe the wave propagation well. This turns out to be the case as long as c is smooth and ω is large. More details on ray theory can be found in the books by Chapman (2004) and Cerveny (2001).

(2.7) is replaced as a starting point and one look for a modified travel time T and amplitude A. Note that in the time domain one looks for $G = A(\mathbf{x})\delta(t - T(\mathbf{x}))$.

One assumes that $S(\mathbf{x}, \omega) = 0$:

$$\Delta g(\mathbf{x}, \omega) + \frac{\omega^2}{c^2(\mathbf{x})} g(\mathbf{x}, \omega) = 0 \tag{2.9}$$

For the derivation (2.8) is inserted into (2.9). First the gradient of G is computed:

$$\nabla g(\mathbf{x}, \omega) = \left(\nabla A(\mathbf{x}) + i\omega A(\mathbf{x})\nabla T(\mathbf{x})\right) e^{i\omega T(\mathbf{x})}. \tag{2.10}$$

Then the Laplacian of G is computed:

$$\Delta g(\mathbf{x}, \omega) = [\Delta A(\mathbf{x}) + 2i\omega\nabla A(\mathbf{x}) \cdot \nabla T(\mathbf{x}) + i\omega A(\mathbf{x})\Delta T(\mathbf{x}) - \omega^2 A(\mathbf{x})\nabla T(\mathbf{x})]e^{i\omega T(\mathbf{x})}. \tag{2.11}$$

Inserting the obtained terms into the wave equation, and dividing by $A(\mathbf{x})$ gives:

$$\frac{\Delta A(\mathbf{x})}{A(\mathbf{x})} + i\omega\left(\frac{2}{A(\mathbf{x})}\nabla A(\mathbf{x}) \cdot \nabla T(\mathbf{x}) + \Delta T(\mathbf{x})\right) - \omega^2\left(\Delta T(\mathbf{x}) - \frac{1}{c^2(\mathbf{x})}\right) = 0. \tag{2.12}$$

For this to be zero for all $\mathbf{x}$ and ω, all ω terms are put equal to zero. To highest order in ω this gives:

$$\Delta T(\mathbf{x}) = \frac{1}{c^2(\mathbf{x})}. \tag{2.13}$$

This is the eikonal equation. To next order in ω one finds the transport equation:

$$2\nabla A(\mathbf{x}) \cdot \nabla T(\mathbf{x}) + A(\mathbf{x})\Delta T(\mathbf{x}) = 0. \tag{2.14}$$

The eikonal equation is a first order non-linear partial differential equation. Its solutions are the wavefronts as they emanate from the source. The eikonal equation can be solved numerically (see e.g. Sethian 1999). Solving the eikonal equation this way has a number of disadvantages. For example it does not take into account multipathing. Therefore, rather than solving it directly it is solved indirectly. Instead of the wavefronts one looks for the lines perpendicular to the wavefront. These lines are called characteristics or rays and they are given by a set off ordinary differential equations, called the ray equations (e.g. Chapman 2004).

2.2.2   Ray Tracing

As noted the ray equations are a set of ordinary differential equations used to solve the non-linear eikonal equation. The ray equations predict the position $\mathbf{x}(t)$ of a ray at a certain time, for a known velocity model c and source position $\mathbf{x}_s$ (e.g. Cerveny 2001). The ray equations are:

$$\frac{d\mathbf{x}}{dt} = c^2\mathbf{p}, \tag{2.15}$$

$$\frac{d\mathbf{p}}{dt} = -\frac{1}{c}\nabla c, \tag{2.16}$$

where $\mathbf{p}$ is slowness, c is velocity, and $\mathbf{x}$ is position along the ray. The slowness is defined as $\mathbf{p} = \nabla T$ and therefore has length $\frac{1}{c}$ (see equation 2.13). To solve the equations initial conditions for the source position ($\mathbf{x}_s$) and take-off angles at the source must be specified. The slowness vector $\mathbf{p}(t)$ gives the direction of the ray, and is parallel to the ray path $\mathbf{x}(t)$. The initial conditions for slowness can be specified in terms of the velocity at the source:

$$c_0 = c(\mathbf{x}_s), \tag{2.17}$$

and the take-off angles. In the 2D case the initial conditions for slowness can be given in polar coordinates (see Figure 9):

$$\mathbf{p}_0 = \left(\frac{\cos\theta}{c_0}, \frac{\sin\theta}{c_0} \right), \tag{2.18}$$

with $\theta \in [0, 2\pi)$. While for the 3D case spherical coordinates are used instead of polar coordinates (see Figure 10):

$$\mathbf{p}_0 = \left(\frac{\sin\theta\cos\phi}{c_0}, \frac{\sin\theta\sin\phi}{c_0}, \frac{\cos\theta}{c_0} \right), \tag{2.19}$$

with $\theta \in [0, \pi]$ and $\phi \in [0, 2\pi]$. θ is the angle between the vertical and the ray path, while ϕ is the azimuth. An important part of this thesis is devoted to numerical solution of the ray equations (2.15) and (2.16), subject to the appropriate initial conditions (see e.g. Chapters 3 and 4).
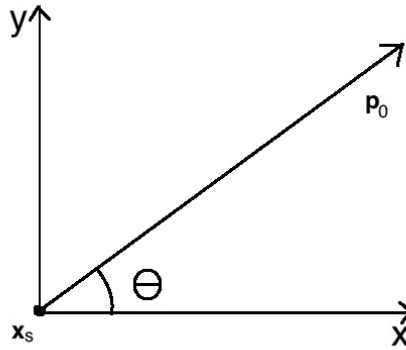
Figure 9: Polar coordinates are used to define the initial conditions for the ray in 2D.
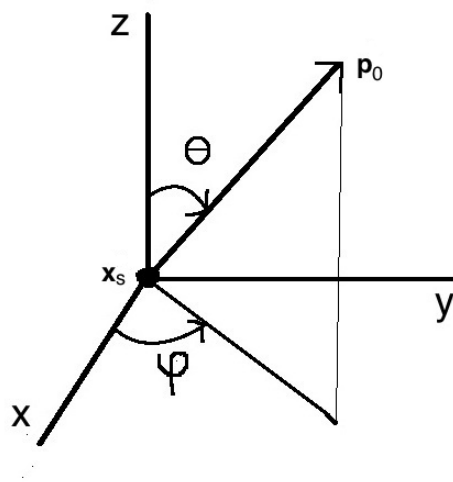
Figure 10: Spherical coordinates are used to define the initial conditions for the ray in 3D.

2.2.3   Amplitudes

Amplitudes for the asymptotic Green's function $A(\mathbf{x})\delta(t - t(\mathbf{x}))$ can be obtained solving the transport equation (2.14):

$$2\nabla A(\mathbf{x}) \cdot \nabla T(\mathbf{x}) + A(\mathbf{x})\Delta T(\mathbf{x}) = 0. \tag{2.20}$$

(This was derived in section 2.2.1). In principle this equation can be solved using Smirnov's lemma (see e.g. Chapman 2004). It is found that in 3D A is proportional to $J^{-1/2}$:

$$J = \frac{\partial \mathbf{x}(t, \theta, \phi)}{\partial(t, \theta, \phi)}, \tag{2.21}$$

where one now considers the ray paths $\mathbf{x}$ also as a function of the take-off angles θ and ϕ. Note that in the case of a homogenous medium $A(\mathbf{x}) = \frac{1}{|\mathbf{x}-\mathbf{x}_s|}$. In other words: A is inversely proportional to the ray length. Therefore it is often reasonable to take $A = 1/\text{raylength}$ as long as the velocity does not vary widely. This is what is done in this thesis.

2.3 Elastic Wave Propagation

2.3.1 The Elastic Wave Equation

The acoustic wave equation works well for describing P-wave propagation in gasses and fluids. For elastic media on the other hand, conditions are different. Still many aspects of acoustic wave propagation are also valuable when studying elastic wave propagation. For example the eikonal equation is the same for both acoustic and isotropic elastic media. Hence, performing ray tracing in an acoustic medium, is the same as performing ray tracing for an elastic medium. Other aspects, such as polarization of the waves and the (seismic) source are quite different.

Elasticity theory describes how a material deforms when stress is applied, and assumes that material goes back to its original state when the stress is released (Snieder 2001). For an infinitesimal surface with surface area ds and a normal vector $\hat{\mathbf{n}}$, the forces acting on ds are:

$$\mathbf{T} = \boldsymbol{\tau} \cdot \hat{\mathbf{n}}. \tag{2.22}$$

Here $\mathbf{T}$ is traction and $\boldsymbol{\tau}$ is stress . Additional forces, which might also be acting in the elastic media, are gravitational forces or a seismic source. All these forces can be described using Newton's second law of motion ($\mathbf{F} = m\mathbf{a}$):

$$\int \rho \ddot{\mathbf{u}} \, dV = \oint \mathbf{T} \, dS + \int \mathbf{f} \, dV. \tag{2.23}$$

Here ρ denotes density, $\ddot{\mathbf{u}}$ is acceleration and $\mathbf{f}$ is the source density.

To find the forces acting on an infinitesimal volume dV Gauss' theorem is applied to equation (2.23):

$$\oint \mathbf{T} \, dS = \int \nabla \cdot \boldsymbol{\tau} \, dV. \tag{2.24}$$

This gives:

$$\int \rho \ddot{\mathbf{u}} \, dV = \int \nabla \cdot \boldsymbol{\tau} \, dV + \int \mathbf{f} \, dV. \tag{2.25}$$

Equation (2.25) holds for an arbitrary volume, and the integrals can be eliminated:

$$\rho \ddot{\mathbf{u}} = \nabla \cdot \boldsymbol{\tau} + \mathbf{f} \tag{2.26}$$

In an elastic medium strain (deformation) is related to applied stress in a complicated way. By looking at only small elastic deformations in the medium, the problem is linearized, and can be described using Hooke's law:

$$\tau_{ij} = c_{ijkl}\epsilon_{kl}, \quad i,j,k,l = 1,2,3. \tag{2.27}$$

Here c_{ijkl} are the components of the elasticity tensor (not to be confused with c, which denotes velocity in the rest of this thesis. The elasticity tensor $\mathbf{c}$ is only used in this section) and ϵ_{kl} are the components of the strain tensor $\boldsymbol{\epsilon}$ (deformation). In elastic media infinitesimal deformation is caused by wave propagation. The relationship between deformation $\boldsymbol{\epsilon}$ and wave displacement $\mathbf{u}$ is:

$$\epsilon_{ij} = \frac{1}{2}(\partial_i u_j + \partial_j u_i). \tag{2.28}$$

Here ∂_i denotes the partial derivative with respect to the x_i coordinate. From (2.28) it can be seen that the strain tensor is symmetric: $\epsilon_{ij} = \epsilon_{ji}$. This is also the case for the elasticity tensor and stress tensor (this follows from Hooke's law (2.27)). The symmetry reduces the number of independent components, hence simplifying the tensors.

The strain relationship (2.28) can be implemented into Hooke's law (2.27):

$$\tau_{ij} = c_{ijkl}\partial_k u_l. \tag{2.29}$$

Inserting equation (2.29) into equation (2.26) gives the elastic wave equation in the time domain:

$$\rho \ddot{u}_i = \partial_j(c_{ijkl}\partial_k u_l) + f_i. \tag{2.30}$$

The elastic wave equation can also be described in frequency domain:

$$\rho \omega^2 u_i + \partial_j(c_{ijkl}\partial_k u_l) = -f_i. \tag{2.31}$$

The elastic wave equation is a linear second order partial differential equation, which one wants to solve for the displacement vector $\mathbf{u}$, given density ρ, elasticity tensor $\mathbf{c}$ and $\mathbf{f}$.

2.4   Elastic Wave Propagation

As noted in section (2.2.1) Green's functions are used to express a general solution of the wave equation. Finding the solution for the elastic wave equation difficult, especially for heterogeneous media. Hence, the assumption is made that the medium is elastic isotropic. This is often also in the case of geothermal reservoirs, a reasonable assumption. For such a medium the stiffness tensor $\mathbf{c}$ is given by:

$$c_{ijkl} = \lambda\delta_{ij}\delta_{kl} + \mu(\delta_{ik}\delta_{jl} + \delta_{il}\delta_{jk}). \tag{2.32}$$

Here δ is the kronecker delta, and λ and μ are Lamé's parameters. If one inserts (2.32) into (2.30) the elastodynamic wave equation in vector notation becomes (Madariaga 2007):

$$\rho \frac{\partial^2}{\partial t^2} \mathbf{u}(\mathbf{x}, t) = (\lambda + \mu) \nabla (\nabla \cdot \mathbf{u}(\mathbf{x}, t)) + \mu \nabla^2 \mathbf{u}(\mathbf{x}, t) + \mathbf{f}(\mathbf{x}, t). \qquad (2.33)$$

If one solves the equation for a point source, the Green's tensor for a homogenous medium is found (see e.g. Pujol 2003). For the point source this gives:

$$\mathbf{f}(\mathbf{x}, t) = \mathbf{f}\delta(t)\delta(\mathbf{x} - \mathbf{x}_s). \qquad (2.34)$$

The Green's tensor for a homogenous medium (with constant λ, μ and ρ) can be computed. It contains near field, intermediate field and far field terms. The near and intermediate fields are only relevant close to the source, while far field terms are considered if one is far from the source. In order to distinguish between near field and far field, the far field is defined as: $\frac{\omega|\mathbf{x}-\mathbf{x}_s|}{c_p} \gg 1$, where c_p is the P-wave velocity $c_p = \sqrt{\frac{\lambda+2\mu}{\rho}}$ (e.g. Madariaga 2007).

In this thesis only the far field terms are interesting, and it can be shown that in a heterogeneous isotropic elastic medium there are two types of waves: P-waves and S-waves. For high frequencies one can look for, just as in the case of acoustic wave propagation, travel time T and amplitude A. The travel times satisfy the eikonal equation $|\nabla T_p|^2 = \frac{1}{c_p^2}$ and $|\nabla T_s|^2 = \frac{1}{c_s^2}$ with $c_p = \sqrt{\frac{\lambda+2\mu}{\rho}}$ and $c_s = \sqrt{\frac{\mu}{\rho}}$. In this thesis I focus only on P-waves and use (Dahlen et al. 2000):

$$\mathbf{G}_{rs} = \mathbf{p}_r \mathbf{p}_s (\rho_r \rho_s c_r c_s^3)^{-\frac{1}{2}} R_{rs}^{-1} e^{i\omega T_{rs}}. \qquad (2.35)$$

Here $\mathbf{p}_s$, $\mathbf{p}_r$ are the slowness vectors at source and receiver respectively, c_r and c_s are the velocity at the source and receiver, ρ_r and ρ_s are the densities at the source and receiver, T_{rs} is the travel time of the ray and R_{rs} is the solution of the transport equation for the P-waves.

Again, note the similarity between the asymptotic acoustic Green's function (2.8) and the elastic isotropic Green's tensor for P-waves (2.35). Both are described by a travel time T and amplitude A, which are found by solving the eikonal and transport equations. The main difference is that the elastic isotropic waves are vector waves, i.e. they are polarized. Therefore the Green's "function" in the elastic isotropic case becomes a tensor.

2.5   Moment Tensors

In this section I give a very brief summary of the concept of a moment tensor and how this is used in seismic modeling. More information on the moment tensors can be found in the books by Stein & Wysession (2003), Aki & Richards (1980) and Dahlen & Tromp (1998).

The moment tensor is a mathematical concept used to describe forces generated by a seismic source (often an earthquake), and is represented by nine couple forces (Dahm & Krüger 2014):

$$\mathbf{M} = M_0 \begin{bmatrix} M_{11} & M_{12} & M_{13} \\ M_{21} & M_{22} & M_{23} \\ M_{31} & M_{32} & M_{33} \end{bmatrix}.$$

Here M_0 is seismic moment, which is a scalar determining the strength of the source. The moment tensor is a convenient tool used in seismology, since it describes both strength and orientation of seismic sources (Jost & Herrmann 1979). Also, the tensor is symmetric, reducing the number of independent components from nine to six.

Moment tensors are mainly used to describe earthquake sources, but can also be used to describe other sources such as explosions, landslides and mix mode ruptures related to fluid injections. There are three different types of sources: double couple, isotropic and compensated linear vector dipole.

2.5.1   Moment Tensor Density, Moment Tensor and Double Couple Sources

For a general seismic source the moment tensor density m_{pq} can be written as:

$$m_{pq} = d_i n_j c_{ijpq}. \tag{2.36}$$

Here $\mathbf{d}$ denotes the slip vector, while $\mathbf{n}$ is the normal vector to the fault plane. For an isotropic medium equation (2.32) can be used, and one has that (Aki & Richards 1980):

$$m_{ij} = \lambda(n_k d_k)\delta_{ij} + \mu(n_i d_j + n_j d_i). \tag{2.37}$$

The first term describes forces expressed on the diagonal (isotropic and compensated linear vector dipole), while the last term express double couple forces. $\mathbf{m}$ is related

to **M** by:

$$M_{pq} = \int_{fault} m_{pq} \, d\Sigma, \tag{2.38}$$

where Σ is the fault surface. If m_{pq} is constant along the fault surface then:

$$M_{pq} = m_{pq} \int_{fault} d\Sigma, \tag{2.39}$$

and so,

$$M_{pq} = A(n_p d_q + n_q d_p). \tag{2.40}$$

This gives the seismic moment for the double couple source:

$$M_0 = \sqrt{0.5 M_{pq} M_{pq}} = \mu A \bar{d}, \tag{2.41}$$

where $\bar{d}$ is average slip along the fault. The green box in Figure 11 shows double couple forces.

2.5.2   Isotropic Sources

Isotropic sources are associated with the three diagonal elements of the moment tensor, and exert the same amount of energy in all directions. Examples of isotropic sources are explosions and implosions. Isotropic sources are associated with volume change. From the seismic moment M_0 it is therefore possible to predict volume change ΔV within a source region, using the following equation (Dahm & Krüger 2014):

$$tr = (M_{11} + M_{22} + M_{33})/3 = \Delta V(\mu + 2\lambda) = M_0. \tag{2.42}$$

The red square in Figure 11 represents isotropic forces. The black focal mechanism shows an explosion (positive isotropic component), while the white represents an implosion (negative isotropic component).

For example, isotropic moment tensors are important in the case of geothermal reservoirs. Water injection at geothermal systems often leads to reservoir expansion. Since the volume of the reservoir changes, it is often possible to see large isotropic components for micro-seismic earthquakes occurring at geothermal reservoirs (Guilhem et al. 2014). Volume changes at the reservoir can be estimated using (2.42), if the Lamé constants are known (Guilhem et al. 2014).

2.5.3   Compensated Linear Vector Dipole

Compensated linear vector dipole sources (CLVD) are used to describe forces with no net moment or volume change (Jost & Herrmann 1989). As for the isotropic component the CLVD source is represented by the diagonal elements of the moment tensor, but for CLVD one dipole is -2 times the size of the two other dipoles (Dahm & Krüger 2014). The seismic moment M_0 is then given by:

$$M_0 = (M_{11} + M_{22} + M_{33})/3 = 0. \tag{2.43}$$

The origin of such sources is not clearly understood. For small CLVD components one assumes that the source arises from errors in the estimated Green's tensors and instrument response (Dahm & Krüger 2014). Large CLVD components are uncommon, and are often only present in complicated tectonic environments. For active volcanic areas these events seem to be more frequent. Also two double couple earthquakes with different source mechanisms occurring close to each other might give a CLVD component (Stein & Wysession 2003). For example:

$$\begin{bmatrix} M_0 & 0 & 0 \\ 0 & 0 & 0 \\ 0 & 0 & -M_0 \end{bmatrix} + \begin{bmatrix} 0 & 0 & 0 \\ 0 & -2M_0 & 0 \\ 0 & 0 & 2M_0 \end{bmatrix} = \begin{bmatrix} M_0 & 0 & 0 \\ 0 & -2M_0 & 0 \\ 0 & 0 & M_0 \end{bmatrix}.$$

Here it can be seen that the sum of the two double couple earthquakes is a CLVD source. Examples of CLVD mechanisms are shown in the orange box in Figure 11.

Moment tensor	Beachball	Moment tensor	Beachball
$\dfrac{1}{\sqrt{3}}\begin{pmatrix} 1 & 0 & 0 \\ 0 & 1 & 0 \\ 0 & 0 & 1 \end{pmatrix}$		$-\dfrac{1}{\sqrt{3}}\begin{pmatrix} 1 & 0 & 0 \\ 0 & 1 & 0 \\ 0 & 0 & 1 \end{pmatrix}$	
$-\dfrac{1}{\sqrt{2}}\begin{pmatrix} 0 & 1 & 0 \\ 1 & 0 & 0 \\ 0 & 0 & 0 \end{pmatrix}$		$\dfrac{1}{\sqrt{2}}\begin{pmatrix} 1 & 0 & 0 \\ 0 & -1 & 0 \\ 0 & 0 & 0 \end{pmatrix}$	
$\dfrac{1}{\sqrt{2}}\begin{pmatrix} 0 & 0 & -1 \\ 0 & 0 & 0 \\ -1 & 0 & 0 \end{pmatrix}$		$\dfrac{1}{\sqrt{2}}\begin{pmatrix} 0 & 0 & 0 \\ 0 & 0 & -1 \\ 0 & -1 & 0 \end{pmatrix}$	
$\dfrac{1}{\sqrt{2}}\begin{pmatrix} -1 & 0 & 0 \\ 0 & 0 & 0 \\ 0 & 0 & 1 \end{pmatrix}$		$\dfrac{1}{\sqrt{2}}\begin{pmatrix} 0 & 0 & 0 \\ 0 & -1 & 0 \\ 0 & 0 & 1 \end{pmatrix}$	
$\dfrac{1}{\sqrt{6}}\begin{pmatrix} 1 & 0 & 0 \\ 0 & -2 & 0 \\ 0 & 0 & 1 \end{pmatrix}$		$\dfrac{1}{\sqrt{6}}\begin{pmatrix} -2 & 0 & 0 \\ 0 & 1 & 0 \\ 0 & 0 & 1 \end{pmatrix}$	
$\dfrac{1}{\sqrt{6}}\begin{pmatrix} 1 & 0 & 0 \\ 0 & 1 & 0 \\ 0 & 0 & -2 \end{pmatrix}$		$-\dfrac{1}{\sqrt{6}}\begin{pmatrix} 1 & 0 & 0 \\ 0 & 1 & 0 \\ 0 & 0 & -2 \end{pmatrix}$	

Figure 11: Source mechanisms and corresponding moment tensors. The red box shows isotropic sources. The green box shows double couple sources, while the orange box shows compensated linear vector dipole sources. Modified figure from Stein & Wysession (2003).

2.5.4   Moment Tensor Relationships

In order to derive the wave field due to a moment tensor $\mathbf{M}$, one can use the relation between the moment tensor and body forces.

If one considers the moment tensor components M_{ij}, each of which represents two-point forces acting in opposite directions separated by an infinitesimal distance h_j. The wavefield due to the moment tensor is now given as (Madariaga 2005):

$$u_k(x,t) = \sum_{i,j} (G_{ki}(\mathbf{x}, t, \mathbf{x}_s + h_j e_j, t_0)) * f_i(t) - G_{ki}(\mathbf{x}, t, \mathbf{x}_s, t_0) * f_i. \qquad (2.44)$$

Here u_k represents ground displacement and f_i is the point force in direction i. While $*$ represents convolution. If one lets $h \to 0$ and takes origin time $t_0=0$, one obtains:

$$u_k(x,t) = \sum_{i,j} \left(\frac{\partial}{\partial x_j} G_{ki}(\mathbf{x},t,\mathbf{x}_s,0) * M_{ij}(t) \right). \tag{2.45}$$

Further the sum of the components can be used to represent the ground displacement at the receiver:

$$u_k(x,t) = \sum_{i,j} G_{ki,j}(\mathbf{x},t,\mathbf{x}_s,t_0) * M_{ij}. \tag{2.46}$$

This can now be used together with the asymptotic elastic isotropic Green's tensor (2.35) to derive an asymptotic expression of the P-wave field in the case of a heterogeneous elastic isotropic medium. This is done by first taking the derivative of the P-wave Green's tensor (2.35):

$$\nabla(\mathbf{G}_{rs}) = \nabla\mathbf{p}_r\mathbf{p}_s A_{rs}e^{i\omega T_{rs}} + \mathbf{p}_r\nabla\mathbf{p}_s A_{rs}e^{i\omega T_{rs}} + \mathbf{p}_r\mathbf{p}_s\nabla A_{rs}e^{i\omega T_{rs}} + i\omega\nabla T_{rs}\mathbf{p}_r\mathbf{p}_s A_{rs}e^{i\omega T_{rs}}, \tag{2.47}$$

where $\nabla T_{rs} = \mathbf{p}_s$. If one inserts the derivative into equation (2.46) and use the high frequency approximation. This gives:

$$\mathbf{u} = w(t - T_{rs})A_{rs}(\mathbf{M} : \mathbf{p}_s\mathbf{p}_s)\mathbf{p}_r. \tag{2.48}$$

$w(t - T_{rs})$ represents a source wavelet, and one has that:

$$\mathbf{M} : \mathbf{p}_s\mathbf{p}_s = \sum M_{ij}p_{si}p_{sj} \quad i,j = x,y,z. \tag{2.49}$$

This gives the relationship between moment tensors, Green's tensors and ground displacement for P-waves. It is useful to look at the different terms of equation (2.48):

$$\mathbf{u} = w(t - T_{rs})\boxed{A_{rs}\boxed{(\mathbf{M} : \mathbf{p}_s\mathbf{p}_s)}\mathbf{p}_r}. \tag{2.50}$$

The outer box in this equation gives the amplitude due to the combined effects of the source (the inner box), the raypath expressed by A_{rs} and polarization at the receiver, expressed by $\mathbf{p}_r$. Equation (2.50) is used in Chapter 5 to model waveforms caused by various representative seismic sources at a heterogeneous geothermal reservoir.

A more detailed explanation of the relationship between the radiation pattern at the source and the moment tensor is given in the next subsection.

2.5.5   Radiation Pattern Associated with Body Waves of Moment Tensors

Radiation patterns are crucial to understand how seismic energy radiates from different seismic sources. When considering radiation of body waves in elastic isotropic medium, as in this thesis one needs to distinguish between P and S-waves. Therefore there exists three radiation patterns for each source: one for P-waves and two for S-waves (SH, SV).

First P-wave propagation is considered, these waves are polarized in the direction of the ray path, and is represented by the polarization vector $\hat{\mathbf{p}}$ (Pujol 2003) :

$$\hat{\mathbf{p}} = \left[\begin{array}{c} \sin\theta\cos\phi \\ \sin\theta\sin\phi \\ \cos\theta \end{array} \right].$$

$\hat{\mathbf{p}}$ is denoted in spherical coordinates. The polarization vectors of the S-waves on the other hand are in the transverse directions, and are described by $\boldsymbol{\Theta}$ (SV) and $\boldsymbol{\Phi}$ (SH). These vectors are also denoted in spherical coordinates, and for the SV wave this gives:

$$\boldsymbol{\Theta} = \left[\begin{array}{c} \cos\theta\cos\phi \\ \cos\theta\sin\phi \\ -\sin\theta \end{array} \right].$$

$\boldsymbol{\Theta}$ is the tangent line of the large sphere, at the point where $\hat{\mathbf{p}}$ intersect the surface (see Figure 12), and is also perpendicular to $\hat{\mathbf{p}}$.

$\boldsymbol{\Phi}$ is used when describing the direction of SH waves, and is perpendicular to both $\hat{\mathbf{p}}$ and $\boldsymbol{\Theta}$. For $\boldsymbol{\Phi}$ this gives: $\boldsymbol{\Phi} = \hat{\mathbf{p}} \times \boldsymbol{\Theta}$. Where $\times$ denotes the cross product. $\boldsymbol{\Phi}$ is then given as:

$$\boldsymbol{\Phi} = \left[\begin{array}{c} -\sin\phi \\ \cos\phi \\ 0 \end{array} \right].$$

$\boldsymbol{\Phi}$ is the tangent line of the small circle (Figure 12), and lies in the xy plane (and therefore has no z-component).

$\hat{\mathbf{p}}$, $\boldsymbol{\Theta}$ and $\boldsymbol{\Phi}$ can in combination with the moment density tensor $\mathbf{m}$ be used to

describe energy radiated from a seismic source. For the P- wave radiation this gives:

$$\mathcal{R}^p = \hat{p}_i m_{ij} \hat{p}_j = \hat{p}_1 v_1 + \hat{p}_2 v_2 + \hat{p}_3 v_3, \tag{2.51}$$

while for the SV radiation pattern this gives:

$$\mathcal{R}^{SV} = \Theta_i m_{ij} \hat{p}_j = \Theta_1 v_1 + \Theta_2 v_2 + \Theta_3 v_3, \tag{2.52}$$

and for SH- radiation pattern at the source this gives:

$$\mathcal{R}^{SH} = \Phi_i m_{ij} \hat{p}_j = \Phi_1 v_1 + \Phi_2 v_2 + \Phi_3 v_3. \tag{2.53}$$

v_i is given as:

$$v_i = m_{i1} \hat{p}_1 + m_{i2} \hat{p}_2 + m_{i3} \hat{p}_3. \tag{2.54}$$

From these equations it can be seen that the radiation pattern depends upon the moment tensor. Hence, different moment tensors have different radiation patterns.

In Chapter 5 the radiation patterns from P-waves are studied in more detail.
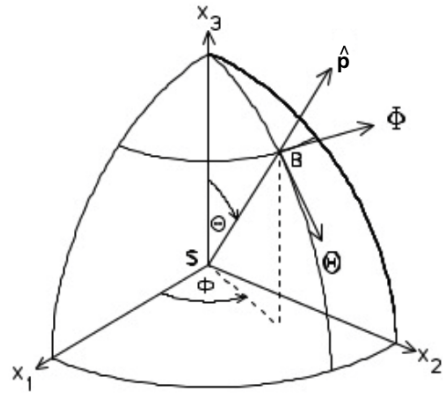
Figure 12: Retrieved from Pujol (2003).

2.5.6   Moment Tensor Inversion

In principle the relationship (2.46) can be used when inverting the moment tensor in the time domain. A similar expression is also used when inverting in the frequency domain. The frequency domain is often used if the source time function is not known.

In order to perform inversion some observed data are required. This data can be fully seismograms or just P and S-wave phases. Inversion can be considered for either surface waves or body waves, and the results from the inversion depend upon the chosen data. In order to obtain good results one should also have a good signal to noise ratio. The solution also depends upon the accuracy of the calculated Green's tensors, which will have some errors related to the velocity model. The Green's tensor also depends on location of the source and the receiver. Hence errors in earthquake location will affect the inversion results in a negative manner (Dahm & Krüger 2014).

In this thesis the focus is on efficient modeling of the waveforms using ray tracing (Chapters 3 and 4) and on the various forms of the radiation patterns for P-waves (Chapter 5), inversion of the moment tensors is beyond the scope of this thesis.

3 Ray Tracing: Theory and Numerical Methods

3.1 Outline

Ray tracing, i.e. solving equations (2.15) and (2.16) is very important in geophysics. It has applications in environmental geophysics, seismic exploration and earthquake seismology. Many theoretical aspects of ray tracing are discussed in books by Chapman (2004) and Cerveny (2001). In many applications hundreds of thousands of calculations are required. An efficient numerical technique is therefore important. However, not much attention is given, either in books or scientific literature, to comparing various numerical techniques. In this chapter I therefore provide a systematic comparison of three popular numerical methods to solve ordinary differential equations. These methods are Euler's method, the midpoint method and fourth order Runge-Kutta.

3.2 Ordinary Differential Equations

Ray tracing involves solving a system of ordinary differential equations with appropriate initial conditions. The equations can be written as (e.g. Kincaid & Cheney 2002):

$$
\begin{cases}
\frac{dx_1}{dt} = f_1(t, x_1, x_2, ..., x_n) \\
\frac{dx_2}{dt} = f_2(t, x_1, x_2, ..., x_n) \\
. \\
. \\
. \\
\frac{dx_n}{dt} = f_n(t, x_1, x_2, ..., x_n),
\end{cases}
\tag{3.1}
$$

with initial conditions $x_i(t_0) = x_{i,0}$ for $i = 1, ..., n$. t is the independent parameter, and in this thesis, stands for time. Often, and also in this thesis, $t_0 = 0$. Here f_i are assumed to be known and the problem is to find x_i. In vector form (3.1) can be written as:

$$
\frac{d\mathbf{x}}{dt} = \mathbf{f}(t, \mathbf{x}).
\tag{3.2}
$$

Equations (3.1) in general can not be solved analytically and in that case need to be solved numerically. The equations (3.1), subject to the initial conditions, can be

numerically solved using different methods, such as in increasing order of complexity Euler's method, midpoint method and fourth order Runge-Kutta. The accuracy of the solution depends upon the methods and step size. Simple methods require fewer calculations than more advanced methods, but can give less accurate results. Moreover higher order does not imply higher accuracy (Press et al. 1992). It is therefore important to compare the methods. In order to illustrate the 3 different numerical methods, I first discuss their implementation for the system (3.1) for the case $n = 1$. In this case one wants to solve:

$$\frac{dx}{dt} = f(t, x), \tag{3.3}$$

with f and given $x(0) = x_0$.

3.3   Eulers Method

Euler's method is a simple numerical method used to find solutions to ordinary differential equations. The method solves the differential equation by approximating the slope and tangent line at the beginning of each interval ($h = t_{i+1} - t_i$), where h is constant, as shown in Figure 13. An expression for the derivative $x' = \frac{dx}{dt}$ is found using Taylor series expansion (Boyce & DiPrima 2010):

$$x(t + h) = x(t) + hx'(t) + \frac{1}{2}h^2 x''(t) + \mathcal{O}(h^3). \tag{3.4}$$

In practice the t values are discrete and denoted by t_i. If one denotes $x(t_i)$ by x_i then:

$$x_{i+1} = x_i + hx'_i + \frac{1}{2}h^2 x''_i + \mathcal{O}(h^3). \tag{3.5}$$

Therefore:

$$\frac{dx_i}{dt} \approx \frac{x_{i+1} - x_i}{h}. \tag{3.6}$$

Inserting in (3.3) gives:

$$\frac{x_{i+1} - x_i}{h} = f(t_i, x_i). \tag{3.7}$$

This can be rewritten as:

$$x_{i+1} \approx x_i + hf(t_i, x_i) + \mathcal{O}(h^2). \tag{3.8}$$

This is the explicit Euler method. Here $x_1 = x(0)$ and $i = 1, ..., n$. Clearly, a smaller step size h, will give better results and decrease the error, but will also increase computation costs. Euler is a quick and simple method to implement. However, the error is of second order $\mathcal{O}(h^2)$, which is relatively large compared to other numerical methods.
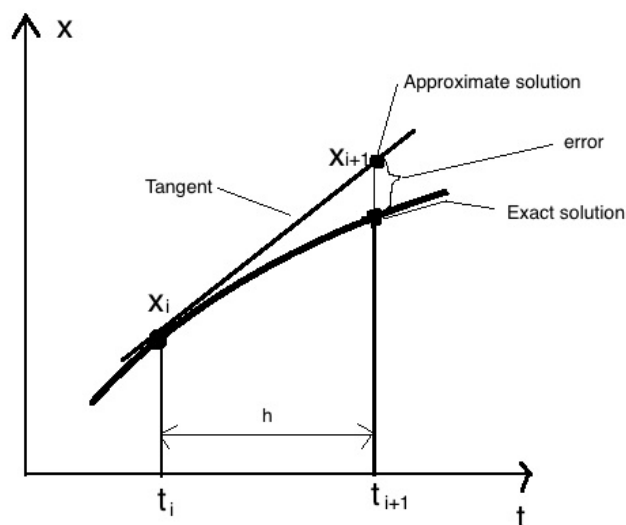
Figure 13: Illustration of Euler's method: the tangent line at the beginning of every interval $[t_i, t_{i+1}]$ is used to determine x_{i+1} from x_i.

3.4   Midpoint Method

The midpoint method is another numerical method used to solve ordinary differential equations. Instead of approximating the slope at the beginning of every interval as in Euler, the midpoint method finds the slope of $f(t_i, x_i)$ at the "midpoint" $x(t_i + \frac{h}{2})$. A tangent line parallel to the tangent line at the midpoint is used to find solutions of the equation, as shown in Figure 14. The method theoretically gives more accurate solutions, than Euler's method. A disadvantage is that the midpoint method requires more calculations. From equation (3.3) it is possible to derive the midpoint method. The explicit midpoint method is a modified version of Euler's method (3.8) (Press et al. 1992):

$$x(t + h) \approx x(t) + hf\left(t + \frac{h}{2}, x\left(t + \frac{h}{2}\right)\right) \tag{3.9}$$

Clearly this is similar to Euler's method. The difference is that the function value is calculated at the midpoint. The value at $x\left(t + \frac{h}{2}\right)$ is not known, but can be approximated using a Taylor expansion:

$$x\left(t + \frac{h}{2}\right) \approx x(t) + \frac{h}{2}x'(t) = x(t) + \frac{h}{2}f(t, x(t)) \tag{3.10}$$

By substituting (3.10) into (3.9) one gets the expression for the explicit midpoint method:

$$x_{i+1} \approx x_i(t) + hf\left(t_i + \frac{h}{2}, x(t_i) + \frac{h}{2}f(t_i, x(t_i))\right) + \mathcal{O}(h^3) \qquad (3.11)$$

A third order error $\mathcal{O}(h^3)$ as in the midpoint method, should, in theory, give better results than a second order error method $\mathcal{O}(h^2)$ as Euler's method.
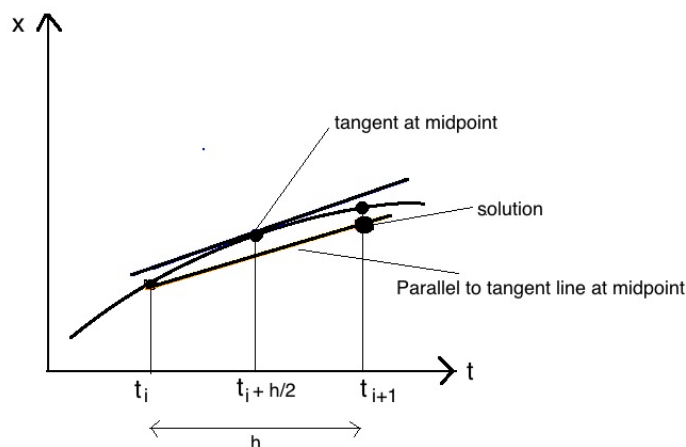
Figure 14: The midpoint method. A parallel line to the tangent at the midpoint $t_i + \frac{h}{2}$, is used to approximate a solution to the ordinary differential equation.

3.5 Fourth Order Runge-Kutta

Fourth order Runge-Kutta is another numerical method, which is used to solve ordinary differential equations (3.1). This method is reckoned to be more exact than both Euler and the midpoint method, but requires a larger number of calculations (Press et al. 1992). h is a constant, as for Euler and the midpoint method. The derivation of the method is quite long, and will not be included here. The algorithm for the fourth order Runge-Kutta given by Kincaid & Cheney (2002) is:

$$K_1 = hf(t_i, x_i), \qquad (3.12)$$

$$K_2 = hf\left(t_i + \frac{h}{2}, x_i + \frac{1}{2}K_1\right), \qquad (3.13)$$

$$K_3 = hf\left(t_i + \frac{h}{2}, x_i + \frac{1}{2}K_2\right), \tag{3.14}$$

$$K_4 = hf\left(t_i + h, x_i + K_3\right). \tag{3.15}$$

Given K_1, K_2, K_3 and K_4 the fourth order Runge-Kutta is given by:

$$x_{i+1} = x_i + \frac{1}{6}(K_1 + 2K_2 + 2K_3 + K_4) + \mathcal{O}(h^5). \tag{3.16}$$

The error is a fifth order in h, $\mathcal{O}(h^5)$, and is therefore small. The method approximates the slope at the initial value (K_1)(Euler's method), twice at the midpoint (K_2, K_3) and at the end value (K_4). This is shown in Figure 15. Even though fourth order Runge-Kutta has a higher order error, Press et al. (1992) note that high orders does not imply high accuracy.
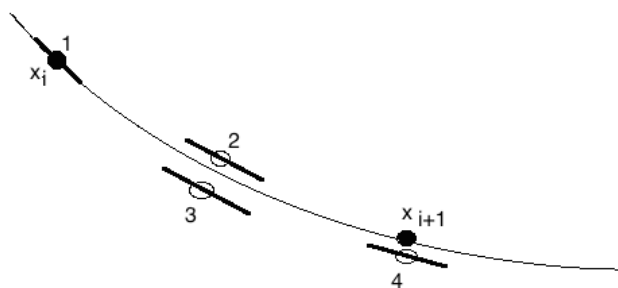
Figure 15: Fourth order Runge-Kutta: The method approximates the slope at the initial value (K_1), twice at the midpoints (K_2, K_3) and at the end value (K_4).

3.6   Interpolation Methods

Given a set of discrete points (in 2D and 3D) and a function f defined at these points only, it is often necessary, to estimate f at another point within the grid. In order to do this interpolation is needed.

There are multiple interpolation schemes (e.g. Press et al. 1992), and the choice of method depends upon the problem, which is to be solved. In this thesis only

linear and spline interpolation will be discussed. These interpolation methods are used in seismology and also in this thesis. In particular I use linear interpolation of the end of ray paths for two-point ray tracing and cubic interpolation is used to determine the velocity and its gradients, which are given on a grid, on points that are not on the grid.

3.6.1 Linear Interpolation

For linear interpolation linear polynomials are used to estimate unknown points within a data set of known points. In order to perform linear interpolation at least two points are required.

For example in 1D interpolation two known points are known: (x_1, y_1) and (x_2, y_2). Here y is a function of x so that $y(x_i) = y_i$, and one wants to estimate a point $y(x)$, where x is known and $x_1 < x < x_2$ (see Figure 16). This can be done using the ratio of the distances between the two points on the x and y-axis, which gives following expression (Press et al. 1992):

$$\frac{y - y_1}{x - x_1} = \frac{y_2 - y_1}{x_2 - x_1}. \tag{3.17}$$

Solving for y the 1D linear approximation of $y(x)$ is found:

$$y = y_1 + \frac{y_2 - y_1}{x_2 - x_1}(x - x_1). \tag{3.18}$$

Linear interpolation is C^0 continuous. So the function is continuous, but its derivative is not necessarily continuous, and this can be a disadvantage. This disadvantage can be overcome using spline interpolation.
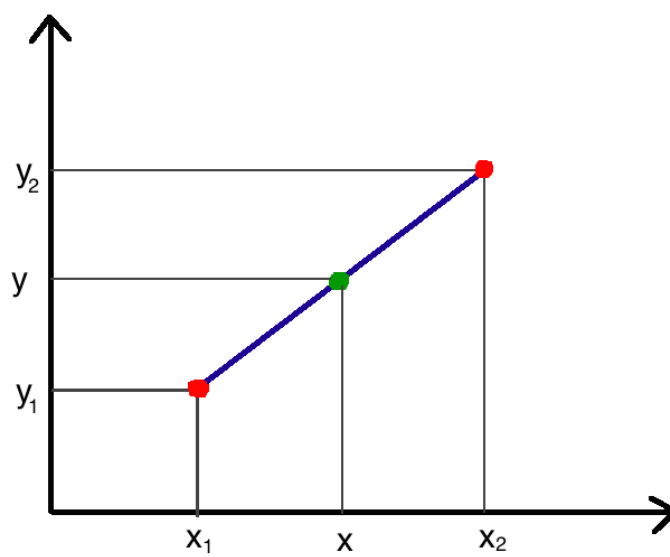
Figure 16: Linear interpolation. The values of the function y at x_1 and x_2 are y_1 and y_2. A straight line is assumed to find y at x.

3.6.2   Cubic Spline Interpolation

For spline interpolation the function value y at a point x is determined from the value of y_i and the points x_i using a polynomial. The advantage with spline inter- polation is that it avoids Runge's phenomena, which is unwanted oscillations caused by a higher order polynomial. The method has a small error even for lower degree polynomials.

For cubic spline interpolation, cubic polynomials are used. This is a very popular method, since it provides accurate results. Also, for spline interpolation one wants to find a function that is C^2 continuous. The method requires more computation time and calculations, than for linear interpolation, but should in principle give more accurate results (Press et al. 1992). An example of 1D cubic spline interpolation is shown in Figure 17.
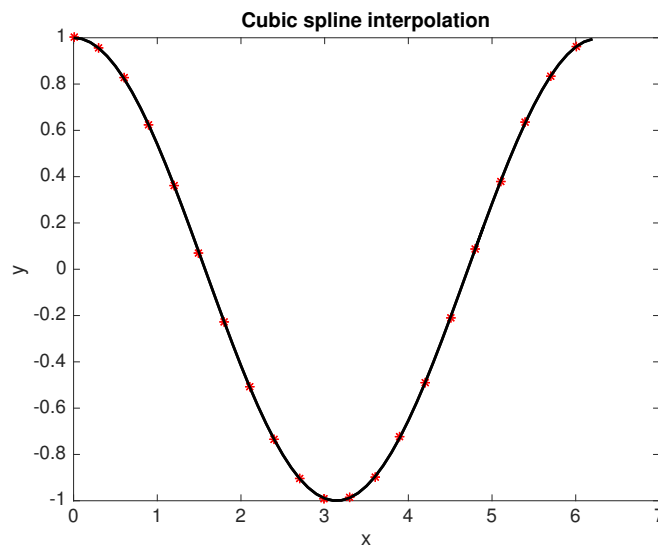
Figure 17: Cubic spline interpolation used to approximate a cosine curve. Red stars show the location where function values are known.

3.7   3D interpolation

For the 3D interpolation, one wants to estimate the function value f at an unknown point (x, y, z) using the known values from the grids x_i, y_i and z_i, and the corresponding values $f_i = f(x_i, y_i, z_i)$. Then (x, y, z) is a point within the boundaries of the grid (Kincaid & Cheney 2002).

For trilinear interpolation eight points are needed, and these are given by the vertices of a cube surrounding the point for interpolation (Press et al. 1992). However, the estimates are not very smooth. Therefore, in this thesis, spline interpolation are used in most cases.

Cubic spline interpolation in 3D can be done using three successive spline interpolations (Press et al. 1992). The interpolation is given by:

$$f(x, y, z) = \sum_{i=0}^{3} \sum_{j=0}^{3} \sum_{k=0}^{3} a_{ijk} x^i y^j z^k, \tag{3.19}$$

Since the interpolation is done three times, the polynomials are no longer "cubic", but actually of ninth order. This interpolation method is costly in terms of computation time and storage. However, the method is used in this thesis since it gives good approximations.

3.8   Implementation

In ray tracing a specific set of ordinary differential equations (equation 2.15 and 2.16) is solved:

$$\frac{d\mathbf{x}}{dt} = c^2 \mathbf{p}, \tag{3.20}$$

$$\frac{d\mathbf{p}}{dt} = -\frac{1}{c} \nabla c. \tag{3.21}$$

Here c is a function of $\mathbf{x}$. In order to relate this to equation (3.2) I write:

$$\frac{d\mathbf{y}}{dt} = \mathbf{f}, \tag{3.22}$$

where:

$$\mathbf{y} = (\mathbf{x}, \mathbf{p}), \tag{3.23}$$

and $\mathbf{f}$ is:

$$\mathbf{f} = (c^2 \mathbf{p}, -\frac{1}{c} \nabla c). \tag{3.24}$$

When solving the system, it is important that the same numerical method is applied to whole array. Initial conditions are given for both slowness (Equation (2.18) and (2.19)) and initial source position. For the initial conditions for slowness spherical coordinates are used for 3D, while polar coordinates are used for 2D ray tracing.

3.8.1   Euler's Method

Euler's formulae for the ray equations are:

$$\frac{\mathbf{x}_{i+1} - \mathbf{x}_i}{\Delta t} = c^2(\mathbf{x}_i)\mathbf{p}_i \tag{3.25}$$

$$\frac{\mathbf{p}_{i+1} - \mathbf{p}_i}{\Delta t} = -\frac{1}{c(\mathbf{x}_i)}\frac{\partial c(\mathbf{x}_i)}{\partial \mathbf{x}} \tag{3.26}$$

This can be rearranged to find the unknowns $\mathbf{x}_{i+1}$ and $\mathbf{p}_{i+1}$ in terms of knowns:

$$\mathbf{x}_{i+1} = c^2(\mathbf{x}_i)\mathbf{p}_i\Delta t + \mathbf{x}_i \tag{3.27}$$

$$\mathbf{p}_{i+1} = -\frac{1}{c(\mathbf{x}_i)}\frac{\partial c(\mathbf{x}_i)}{\partial \mathbf{x}}\Delta t + \mathbf{p}_i \tag{3.28}$$

3.8.2   Midpoint Method

The midpoint implementation is similar to the Euler implementation. The only difference is that the velocity has to be calculated at the midpoint of the interval. This is done using the midpoint method described in section 3.4. To find $\mathbf{x}$ and $\mathbf{p}$ at the midpoint a Taylor expansion is used:

$$\mathbf{x}_{i+\frac{h}{2}} \approx \mathbf{x}_i + \frac{\Delta t}{2}c^2(\mathbf{x}_i)\mathbf{p}_i \tag{3.29}$$

$$\mathbf{p}_{i+\frac{h}{2}} \approx \mathbf{p}_i + \frac{\Delta t}{2}\left(-\frac{1}{c(\mathbf{x}_i)}\frac{\partial c(\mathbf{x}_i)}{\partial \mathbf{x}}\right) \tag{3.30}$$

Where $\mathbf{x}_i$ and $\mathbf{p}_i$ are evaluated at the beginning of every interval. The velocity at the midpoint is then found using spline interpolation on the velocity grid, where one wants to approximate:

$$c_1 = c\left(\mathbf{x}_{i+\frac{h}{2}}\right) \tag{3.31}$$

The new velocity c_1 is further implemented into the ray equations, using the same formulae as for Euler:

$$\mathbf{x}_{i+1} = c_1^2 \mathbf{p}_{i+\frac{h}{2}} \Delta t + \mathbf{x}_i \tag{3.32}$$

$$\mathbf{p}_{i+1} = -\frac{1}{c_1} \frac{\partial c(\mathbf{x}_{i+\frac{h}{2}})}{\partial \mathbf{x}} \Delta t + \mathbf{p}_i \tag{3.33}$$

3.8.3   Fourth Order Runge-Kutta

The fourth order Runge-Kutta is quite extensive to implement. The concept of the implementation is similar to that for the midpoint method, where one has to evaluate the velocity at different parts of the interval. In order to find $\mathbf{K}_1$ and $\mathbf{F}_1$, the slope is first approximated at the beginning of the interval (Euler's method):

$$\mathbf{K}_{1,i} = c(\mathbf{x}_i)^2 \mathbf{p}_i \Delta t, \tag{3.34}$$

$$\mathbf{F}_{1,i} = \left(-\frac{1}{c(\mathbf{x}_i)} \frac{\partial c(\mathbf{x}_i)}{\partial \mathbf{x}} \right) \Delta t. \tag{3.35}$$

To find $\mathbf{K}_2$, $\mathbf{K}_3$, $\mathbf{F}_2$ and $\mathbf{F}_3$ the slope is approximated at the midpoint of the interval. Before being able to find $\mathbf{K}_2$ and $\mathbf{F}_2$, one needs to approximate the values at the midpoint. This is done using $\mathbf{K}_{1,i}$ and $\mathbf{F}_{1,i}$:

$$\mathbf{x}_{i'+\frac{h}{2}} = \mathbf{x}_i + \frac{1}{2}\mathbf{K}_{1,i}, \tag{3.36}$$

$$\mathbf{p}_{i'+\frac{h}{2}} = \mathbf{p}_i + \frac{1}{2}\mathbf{F}_{1,i}. \tag{3.37}$$

The velocity is found from spline interpolation, for simplicity this velocity is called c_2:

$$c_2 = c\left(\mathbf{x}_{i'+\frac{h}{2}} \right). \tag{3.38}$$

$\mathbf{K}_{2,i'+\frac{h}{2}}$ and $\mathbf{F}_{2,i'+\frac{h}{2}}$ can then be found using:

$$\mathbf{K}_{2,i'+\frac{h}{2}} = c_2^2 \mathbf{p}_{i'+\frac{h}{2}} \Delta t, \tag{3.39}$$

$$\mathbf{F}_{2,i'+\frac{h}{2}} = \left(-\frac{1}{c_2} \frac{\partial c(\mathbf{x}_{i'+\frac{h}{2}})}{\partial \mathbf{x}} \right) \Delta t. \tag{3.40}$$

$\mathbf{K}_{3,i''+\frac{h}{2}}$ and $\mathbf{F}_{3,i''+\frac{h}{2}}$ are found in the same way as $\mathbf{K}_{2,i'+\frac{h}{2}}$ and $\mathbf{F}_{2,i'+\frac{h}{2}}$, and are also approximated at the midpoint. The points used for the approximation are given by:

$$\mathbf{x}_{i''+\frac{h}{2}} = \mathbf{x}_i + \frac{1}{2}\mathbf{K}_{2,i'+\frac{h}{2}}, \tag{3.41}$$

$$\mathbf{p}_{i''+\frac{h}{2}} = \mathbf{p}_i + \frac{1}{2}\mathbf{F}_{2,i'+\frac{h}{2}}. \tag{3.42}$$

Then velocity at the given point is found using spline interpolation:

$$c_3 = c(\mathbf{x}_{i''+\frac{h}{2}}). \tag{3.43}$$

$\mathbf{K}_{3,i''+\frac{h}{2}}$ and $\mathbf{F}_{3,i''+\frac{h}{2}}$ are then given by:

$$\mathbf{K}_{3,i''+\frac{h}{2}} = c_3^2 \mathbf{p}_{i''+\frac{h}{2}}\Delta t, \tag{3.44}$$

$$\mathbf{F}_{3,i''+\frac{h}{2}} = \left(-\frac{1}{c_3}\frac{\partial c(\mathbf{x}_{i''+\frac{h}{2}})}{\partial \mathbf{x}}\right)\Delta t. \tag{3.45}$$

For $\mathbf{K}_4$ and $\mathbf{F}_4$ one wants to find the slope at the end of the interval. The end of the interval is given by:

$$\mathbf{x}_{i+h} = \mathbf{x}_i + \mathbf{K}_{3,i''+\frac{h}{2}}, \tag{3.46}$$

$$\mathbf{p}_{i+h} = \mathbf{p}_i + \mathbf{F}_{3,i''+\frac{h}{2}}. \tag{3.47}$$

Then velocity at the given point is found using spline interpolation:

$$c_4 = c(\mathbf{x}_{i+h}). \tag{3.48}$$

$\mathbf{K}_{4,i+h}$ and $\mathbf{F}_{4,i+h}$ are therefore given by:

$$\mathbf{K}_{4,i+h} = c_4^2 \mathbf{p}_{i+h}\Delta t, \tag{3.49}$$

$$\mathbf{F}_{4,i+h} = \left(-\frac{1}{c_4}\frac{\partial c(\mathbf{x}_{i+h})}{\partial \mathbf{x}}\right)\Delta t. \tag{3.50}$$

After finding $\mathbf{K}_1$, $\mathbf{K}_2$, $\mathbf{K}_3$ $\mathbf{K}_4$ and $\mathbf{F}_1$, $\mathbf{F}_2$, $\mathbf{F}_3$, $\mathbf{F}_4$, $\mathbf{x}_{i+1}$ and $\mathbf{p}_{i+1}$ can be approximated using:

$$\mathbf{x}_{i+1} = \mathbf{x}_i + \frac{1}{6}(\mathbf{K}_1 + 2\mathbf{K}_2 + 2\mathbf{K}_3 + \mathbf{K}_4), \tag{3.51}$$

$$\mathbf{p}_{i+1} = \mathbf{p}_i + \frac{1}{6}(\mathbf{F}_1 + 2\mathbf{F}_2 + 2\mathbf{F}_3 + \mathbf{F}_4). \tag{3.52}$$

4 Ray Tracing: Applications to Geothermal Reservoirs

4.1 Velocity Models

For this thesis I am interested in both 1D and 3D velocity models. I use these models to study ray tracing using the three numerical methods introduced in the previous chapter: Euler, midpoint and the fourth order Runge-Kutta. The focus of this thesis is micro-seismicity at geothermal reservoirs. Hence, I use velocity models that mimic geothermal reservoirs and their overburdens.

4.1.1 1D Velocity Model

For this thesis the 1D velocity model used is a P-wave velocity model of The Geysers geothermal field in California. This is given in the paper by Guilhem et al. (2014). The model is layered, with different velocities for each layer, and is constructed by averaging a 3D velocity model. This velocity model is shown in Figure 18, and is displayed in 3D. It should be emphasized that by a 1D velocity model is meant a velocity model defined on a 3D grid which depends only on depth: thus $c(x, y, z) = c(0, 0, z)$ for all x and y. For convenience the velocity at a point $\mathbf{x} = (x, y, z)$ is often written as c(z) in this case.
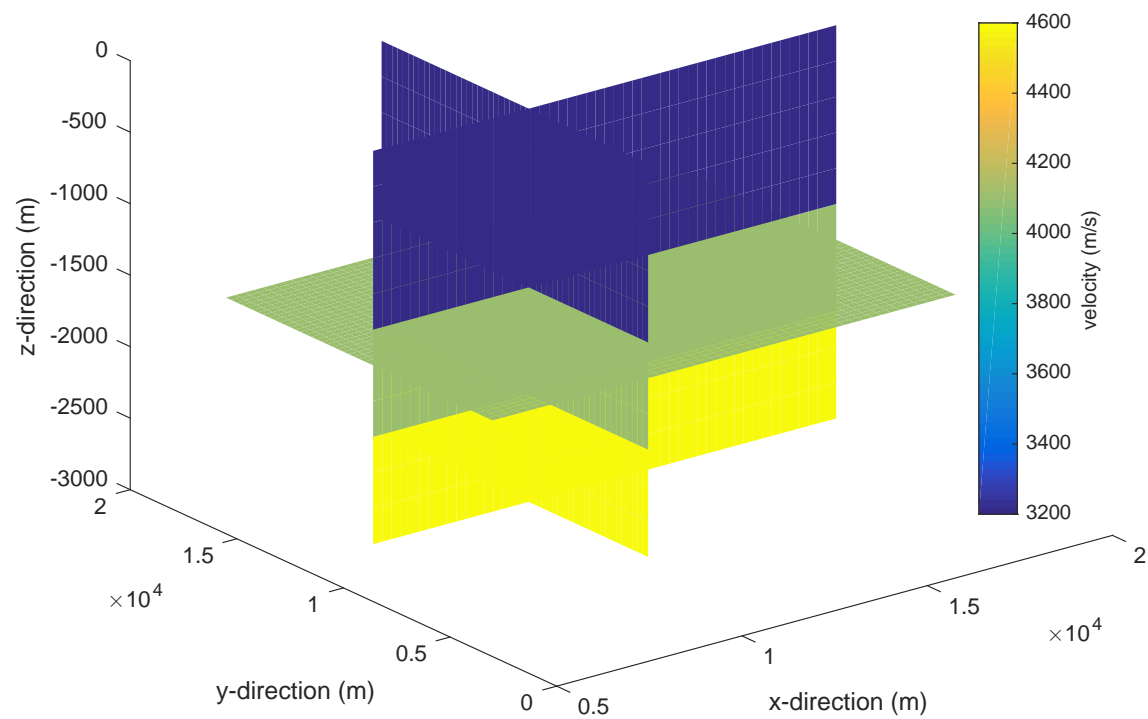
Figure 18: 1D velocity model, The Geysers, Guilhem et al. (2014).

4.1.2   Random Gaussian 3D Perturbations

3D velocity models were constructed using random Gaussian perturbations. The models are constructed from the autocorrelation function $q(r)$ (Baig & Dahlen 2004) defined as:

$$q(r) = \epsilon^2 \sigma^2 e^{-\frac{r}{a^2}} \tag{4.1}$$

Here σ is slowness of the background model and $r = ||\mathbf{x} - \mathbf{x'}||$, a is the correlation length, which is the characteristic length of the perturbation, and ϵ is the RMS strength of the perturbations in percentage, and is given:

$$\epsilon = \frac{\delta\sigma^2(x)}{\sigma^2}, \tag{4.2}$$

where $\delta\sigma$ is the slowness of the perturbation. After constructing the perturbations the background velocity model was added, which in this case is the layered 1D velocity model used at The Geysers (Figure 18).

Two of the constructed velocity models are shown in Figure 19 and 20. For both models I have that ϵ is 5%. However, the correlation length varies. For the first model the correlation length is $a = 500m$ (large scale perturbations), while for the second model the correlation length is $a = 100m$ (small scale perturbations).
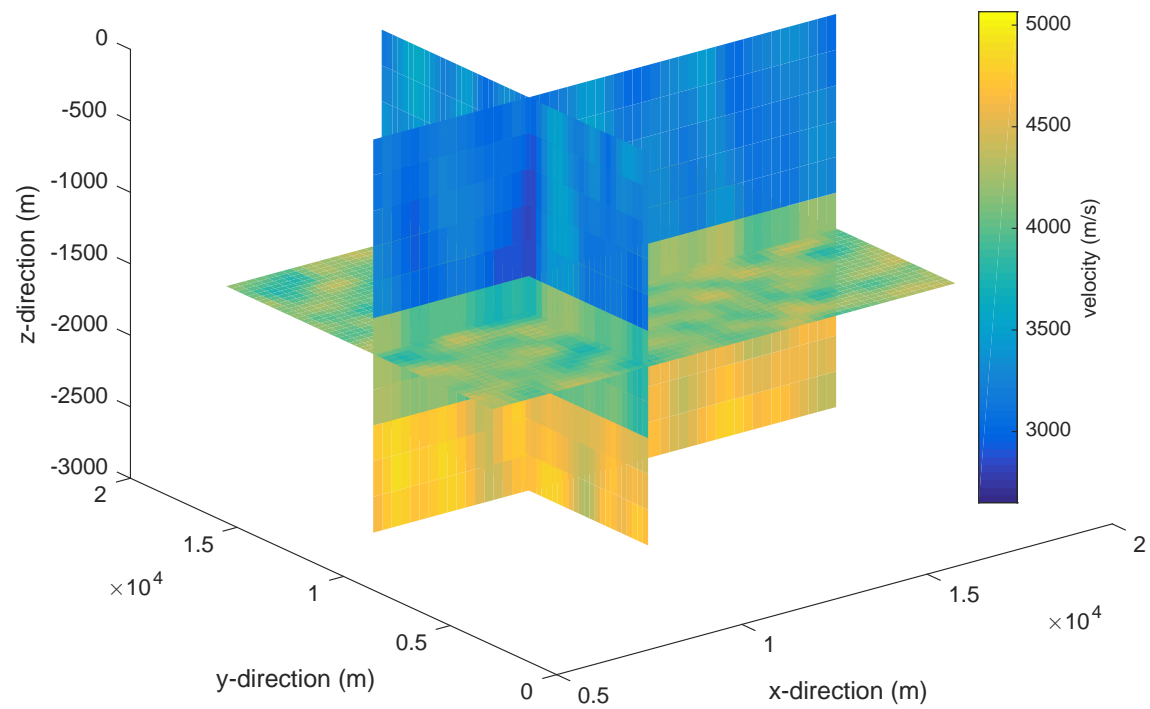
Figure 19: 1D velocity model from The Geysers, with large scale perturbations. Perturbation strength 5%, correlation length 500m.
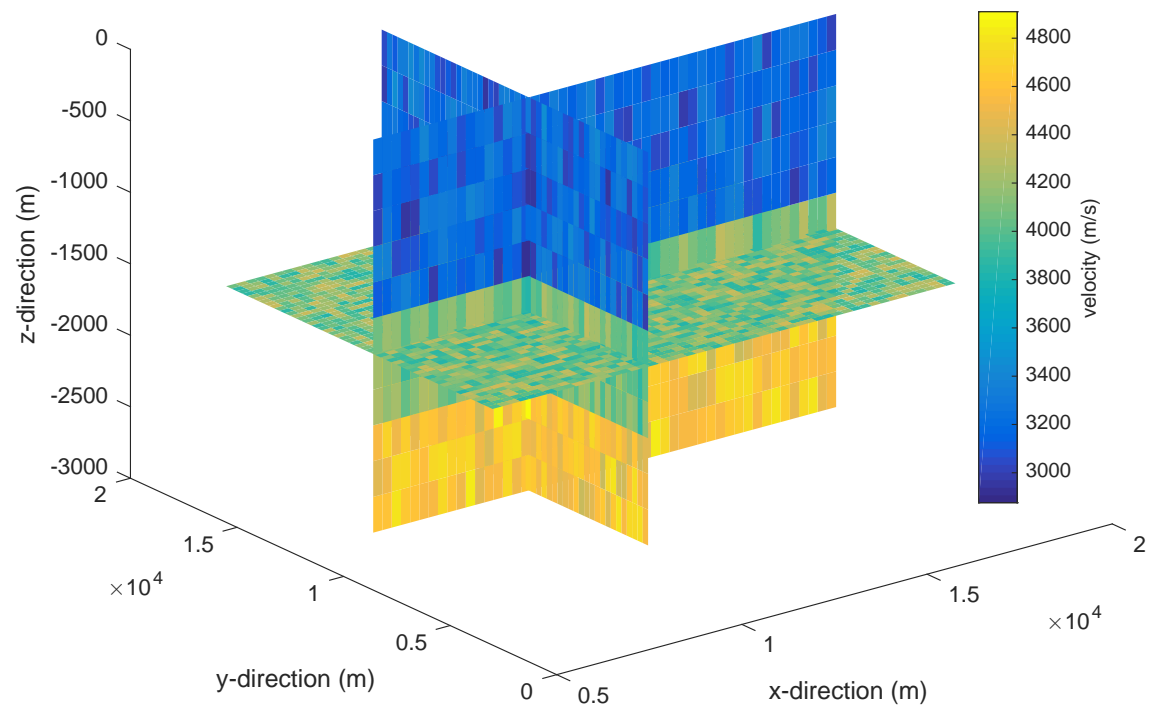
Figure 20: 1D velocity model from The Geysers, with small scale perturbations. Perturbation strength 5%, correlation length 100m.

4.2   One-Point Ray Tracing

Before discussing the comparison between ray tracing methods in this and the next section I briefly discuss implementation concepts in ray tracing: one-point ray tracing and two-point ray tracing.

Ray tracing from a source to the surface using a specific pair of take-off angles θ and ϕ is called one-point ray tracing. An example of one-point ray tracing is shown in Figure 21, using the layered 1D velocity model of The Geysers.
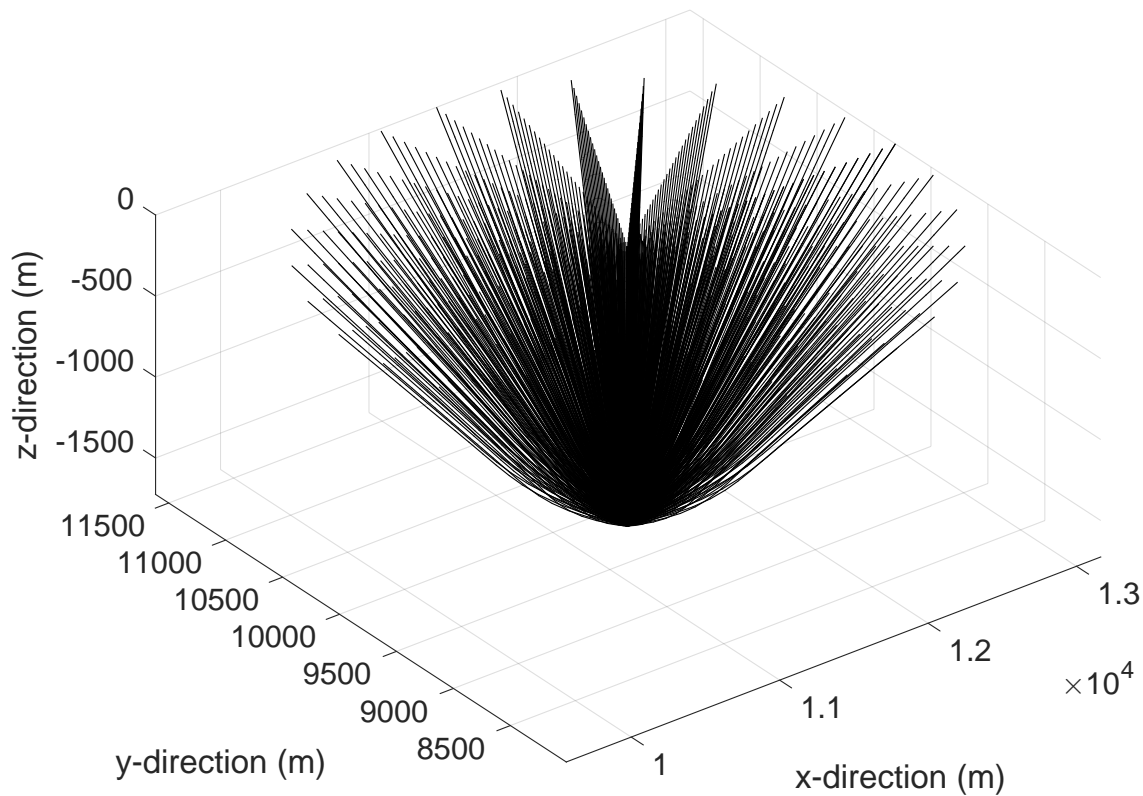
Figure 21: one-point ray tracing for the 1D velocity model at The Geysers.

4.3   Two-Point Ray Tracing

Two-point ray tracing is often used in seismology and seismic exploration in order to acquire both modeling and inversion schemes. For two-point ray tracing one wants

to find the ray path between a starting location (the source) and an end point at the surface $z = 0$ (the receiver) within a given model (Cerveny 2001).

In two-point ray tracing the end location of this ray at the surface is not known beforehand, and some kind of iteration or interpolation method is needed. This is essential when computing seismograms using ray tracing.

In order to do two-point ray tracing, one starts with one-point ray tracing, using a large number of take-off angles and compute the corresponding ray paths. Each take-off angle is associated with a certain ray, which has a specific arrival position at the surface (the red stars in Figure 22). The locations of the red stars are then used in a triangulation, as shown in Figure 22. At the red stars the take-off angles are known, and these known values can be used to predict take-off angles at other positions at the surface (receivers), using linear interpolation within each triangle.

For example, in Figure 23 a receiver indicated by a black star is located within one of the Delaunay triangles. By using the three vertices of the enclosing triangle, it is possible to compute the take-off angles at the receiver using interpolation. Ray tracing can then be performed for these particular take-off angles.

If the new ray gets within a certain distance of the black star, then the "two-point" ray has been found. If not then a new triangle can be chosen, using this failed two-point ray, and the process can be repeated. For the applications in this thesis it turned out not to be necessary. Obviously there is a trade-off between the computation speed (the number of take-off angles used) and the accuracy in the two-point ray tracing. This is not a topic of this thesis, however and therefore not explained further. In Figure 24 two-point ray tracing performed for a grid of receivers is shown.
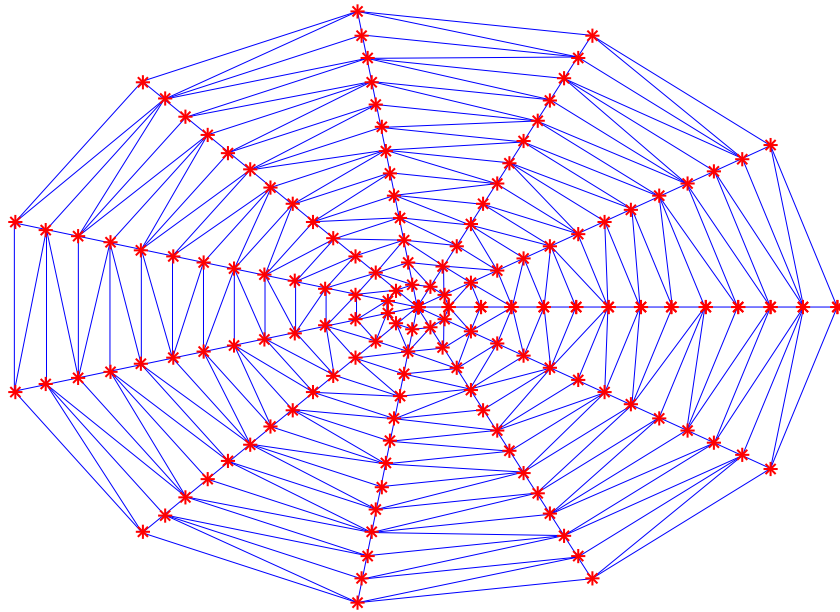
Figure 22: Triangulation at the surface. The triangles are constructed using the arrivals of the one-point ray tracing.
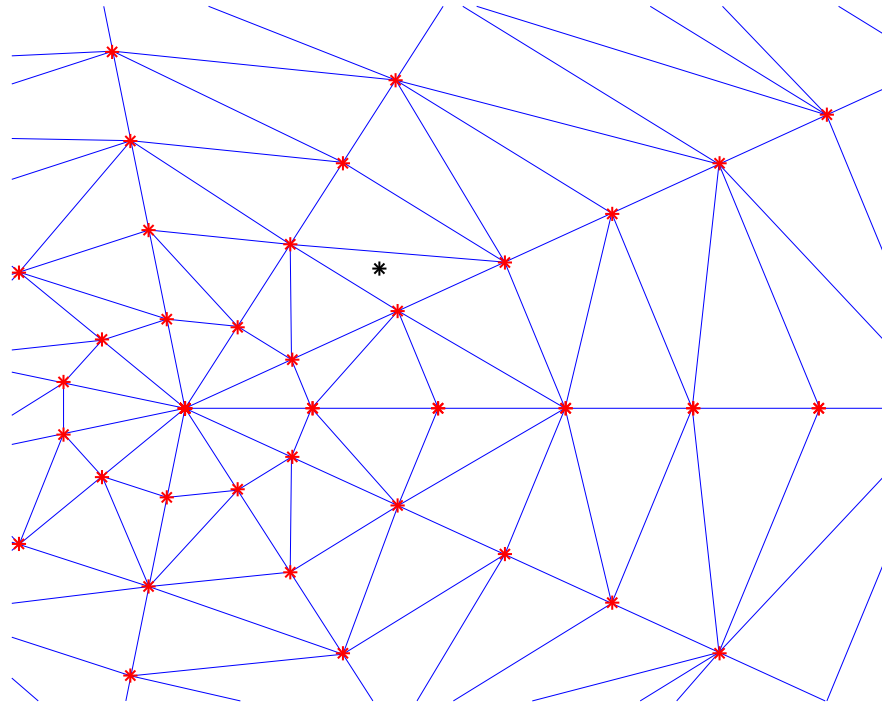
Figure 23: Figure to illustrate two-point ray tracing. In this figure the black star represents a receiver. The take-off angles at the red stars are known, and are used to compute the take-off angle at the receiver by using interpolation. See the text for more information.
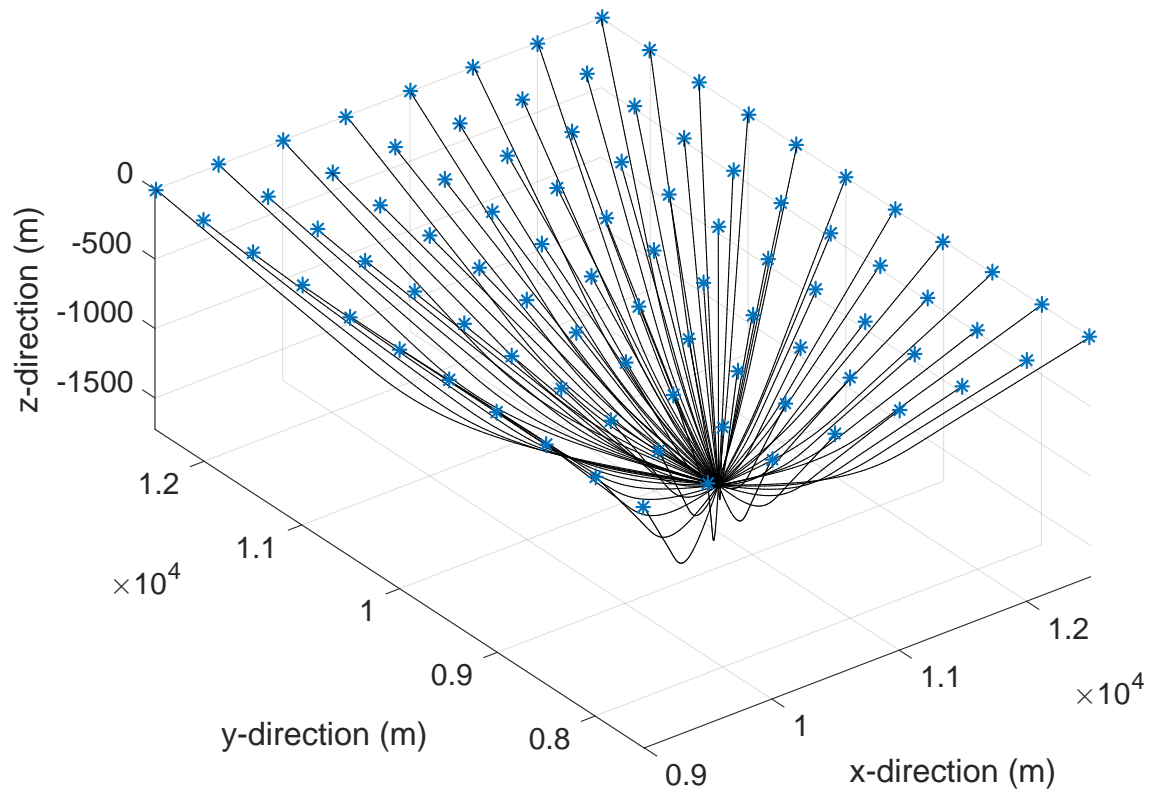
Figure 24: Two-point ray tracing example. The rays travel from the source to a grid of receivers. The blue stars represent the receivers.

4.4   Ray Tracing Results

4.4.1   One-Point Ray Tracing

One-point ray tracing was performed and the three numerical ray tracing methods, Euler, the midpoint method and fourth order Runge-Kutta, were compared.

The comparison was done for three different velocity models, discussed in section 4.1.1 and 4.1.2: the 1D velocity model by Guilhem et al. 2014 (Figure 18) and the two 3D velocity models (Figure 19 and Figure 20), using various time steps. The grid spacing used was 250m.

After some initial testing a time step of 0.04s seemed to be relatively accurate. I therefore decided to use this time step, as well as computing a smaller and two larger time steps. The time steps used for this test were therefore dt=0.009s, dt=0.04s, dt=0.07s and dt=0.1s. For this comparison I assume that the fourth order Runge-Kutta with a small time step (dt=0.09s), provides "exact" results.

For the one-point ray tracing, the comparison between the three methods was by the distance between the various raypaths (depending on method, velocity model and time step) at the surface. The one-point ray tracing was done for different take-off angles, and the differences and the means for each run was used as a comparison.

The source was assumed to be at 1700m depth. This is a typical depth of earthquakes at The Geysers (Guilhem et al. 2014).

Gritto et al. (2013) constructed a 3D velocity model of The Geysers (not the same as the model used by Guilhem et al. 2014, which is older) using a tomography with a node spacing of 600m. The noise in the travel time measurements for this model is 0.01 seconds. This corresponds to a length of 50m, if an approximate P-wave speed of 5km/s is assumed. Therefore, I assume that distances between ray paths of less than 50m provides reliable results.

4.4.2   1D Velocity Model

I first present the one-point ray tracing results for the 1D velocity model. The results for this test are summarized in Figures 25, 26 and 27. In Figures 25 and 26 the distance between the end of the raypaths at the surface is plotted against azimuthal ϕ and incidence θ for Euler vs. fourth order Runge-Kutta and the midpoint method

vs. fourth order Runge-Kutta for each of the four time steps. The angles are given in degrees. In the figures it can be seen that the error increases gradually for larger θ. Also, for the 1D velocity model it can be seen that the curves are rotation symmetric (i.e independent of ϕ) as expected.

As expected: Euler is worse than the two other methods. This is summarized, shown in Figure 27, which shows the mean of the distances at the surface for each of the time steps. For Euler's method these values range from approximately 5m for the smallest time step to an average of 55m for the larger time step. For the midpoint method the differences with fourth order Runge-Kutta are not as large, and are close to zero for the smallest time step, and have a maximum average value of approximately 4.5m for the largest time step.

As mentioned in the previous subsection I only allow an error of 50m. From Figure 25 it can be seen that the two last time steps of Euler exceeds this value, hence giving invalid results.

For the largest time step of the midpoint point method there is a peculiar oscillation effect, which is shown in Figure 26. This is likely caused by an "aliasing" effect. For a relatively large "dt", the ray tracing does not sample the velocity model well enough. The concept is shown in Figure 28. In the figure ray tracing for two different time steps are shown. The rays have the same initial position. This velocity model contains heterogeneities, shown as grey circles (used for illustration). For the largest time step Δt_1 the ray tracing jumps over the first heterogeneity, while the smaller time step Δt_2, includes the velocity heterogeneity, and gives more reliable results.
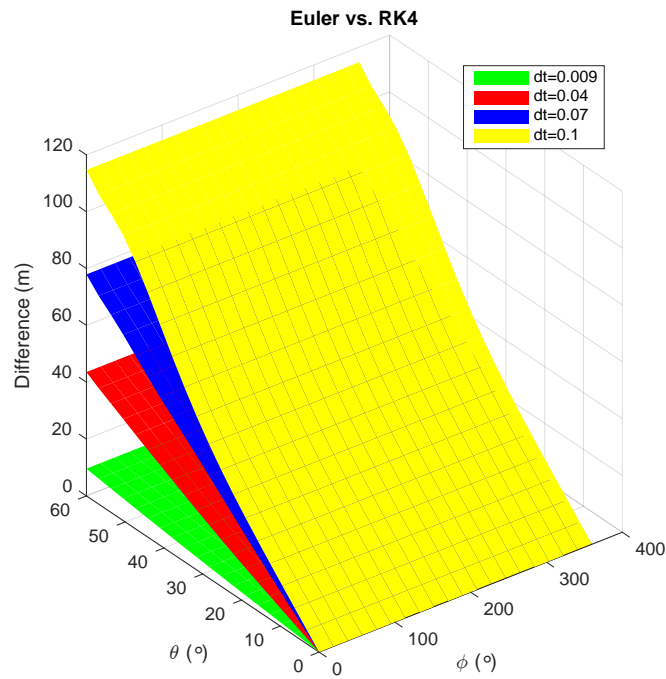
Figure 25: Difference in distance of the arrival positions at the surface between the exact fourth order Runge-Kutta and the different time steps of Euler's method as computed using the 1D velocity model. The results are plotted against azimuth ϕ and incidence angles θ. The angles are given in degrees.
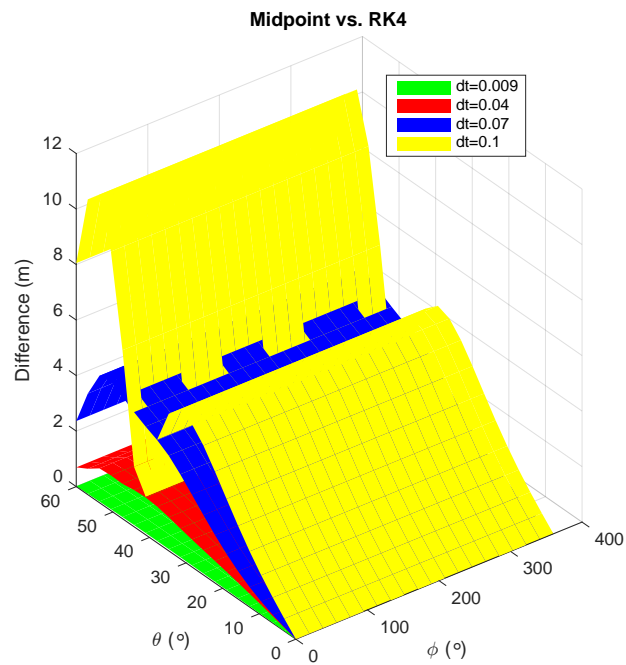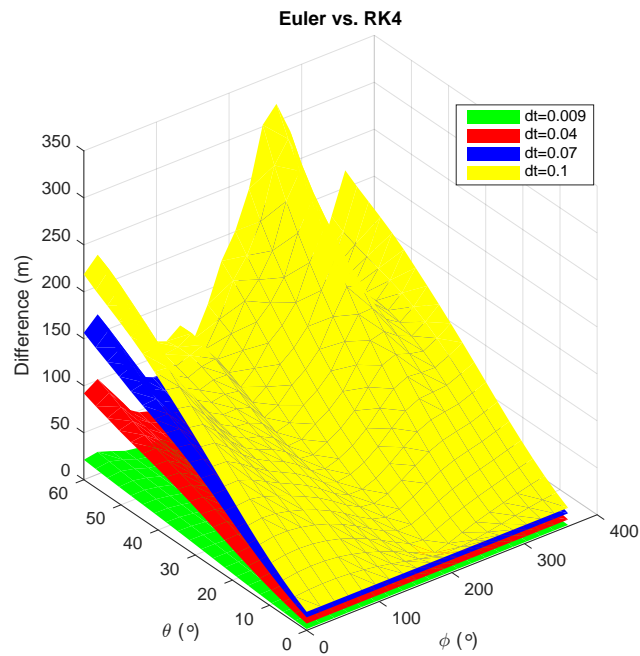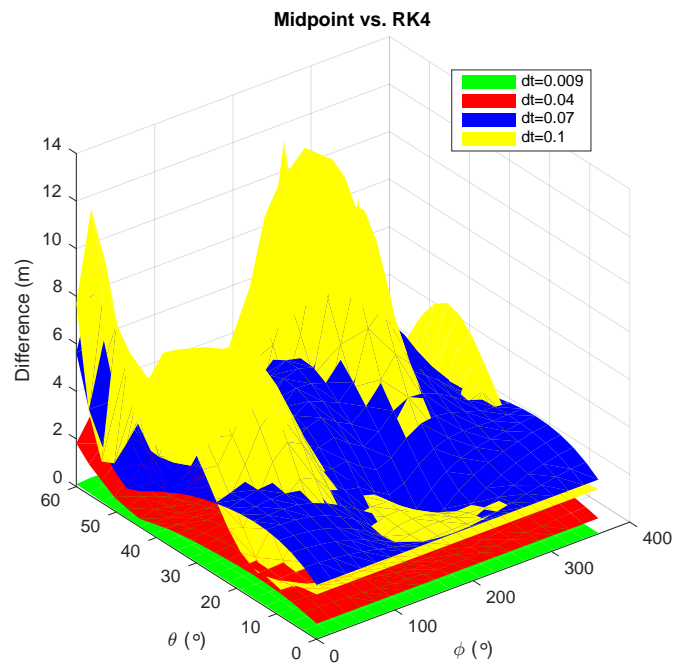
Figure 26: Difference in distance of the arrival positions at the surface between the fourth order Runge-Kutta and the different time steps of the midpoint method as computed using the 1D velocity model.
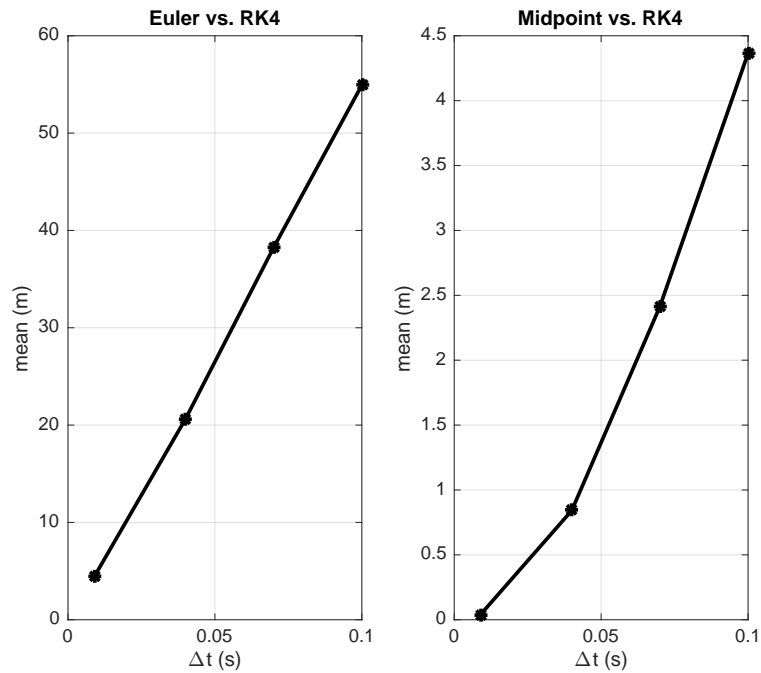
Figure 27: Mean difference in distance at the surface between fourth order Runge-Kutta and the two numerical methods for a 1D velocity model. The left plot shows the mean for Euler's method, while the mean for the midpoint method is shown on the right. Notice the difference in scale on the y-axis between the two numerical methods.
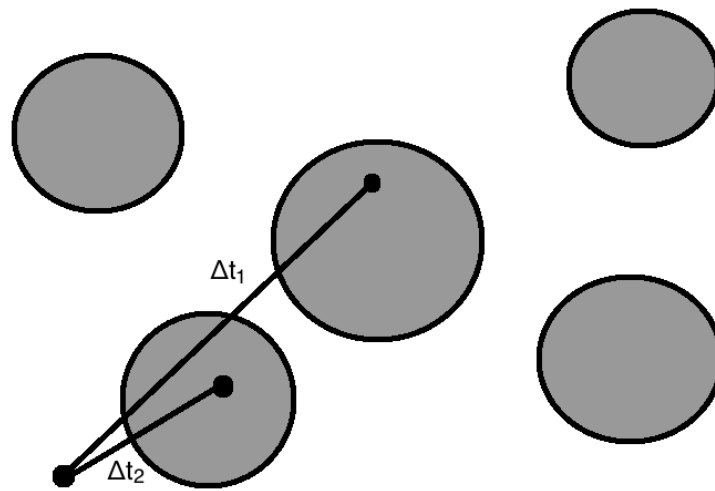
Figure 28: The figure illustrating the "aliasing" effect, which may occur if too large time steps are used for ray tracing.

4.4.3   3D Large Scale Perturbation Velocity Model

The same tests as previously provided for the 1D velocity model, were also performed for a 3D velocity model with large scale perturbations (with a correlation length of 500m). The results are presented in Figures 29, 30 and 31. In Figures 29 and 30 it should be noted that the curves are no longer rotation symmetric, as for the 1D velocity model, and varies over the whole surface. This effect is a result of the 3D velocity variations of the weakly heterogeneous medium. For the 3D large scale velocity model (as for the 1D model) the error increases for larger θ.

The differences between the three numerical methods are larger for the more complex 3D model, than the simpler 1D model. This is particularly clear in Figure 31, which shows the mean of the distance between the rays. The average deviation in difference in distance at the surface between the exact fourth order Runge-Kutta and Euler range from roughly 10m for the smaller time step to approximately 90m for the larger time step (much larger than for the 1D model), while for the midpoint method this range is from zero to ca. 4m. Hence, a small time step of the midpoint method gives almost as good result as the small time step of the fourth order Runge-Kutta.

The "aliasing" effect for the largest time step of the midpoint method also occur for the large scale velocity model, where the error jumps at certain locations (Figure 30) .

Figure 29: Difference in distance of the arrival positions at the surface between the fourth order Runge-Kutta and the different time steps of Euler's method as computed using the large scale 3D perturbation velocity model.

Figure 30: Difference in distance of the arrival positions at the surface between the fourth order Runge-Kutta and the different time steps of the midpoint method as computed using the large scale 3D perturbation velocity model.
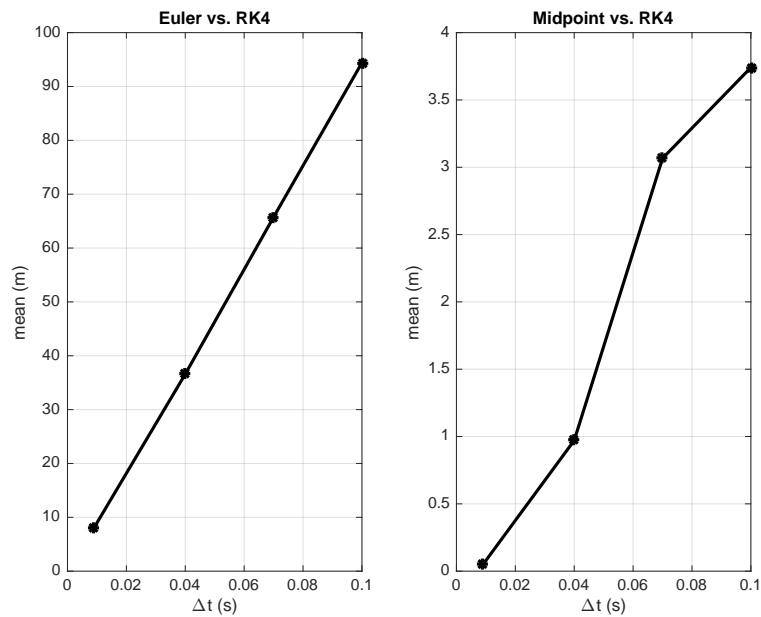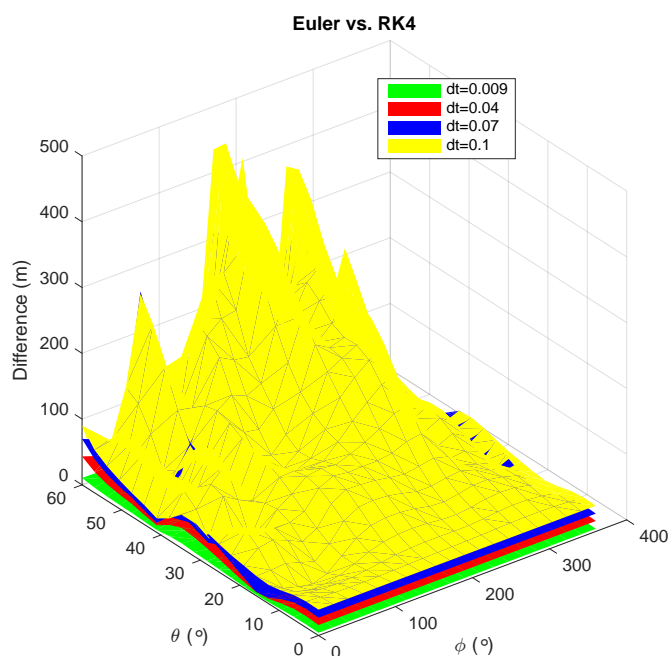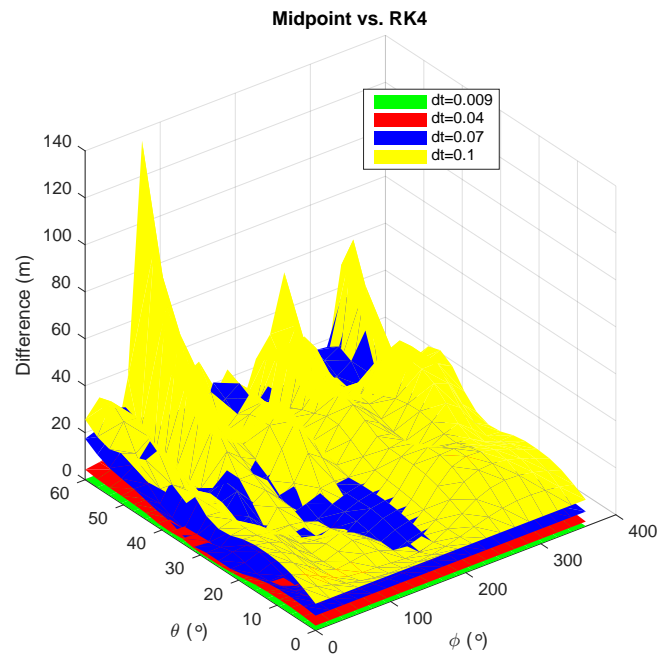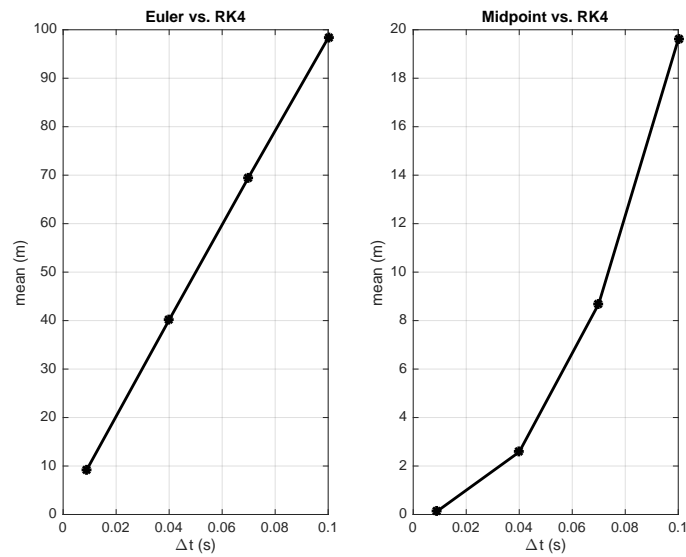
Figure 31: Mean difference in distance at the surface between fourth order Runge-Kutta and the two numerical methods for a 3D velocity model with large scale perturbations. On the left plot, the mean for Euler's method is shown, while the mean for the midpoint method is shown in the plot on the right. Notice the difference in scale on the y-axis between the two numerical methods.

4.4.4   3D Small Scale Perturbation Velocity Model

The same tests were also performed for the 3D velocity model with small scale perturbations (with correlation length of 100m). This model is not as smooth as the two other velocity models, and the ray tracing and difference in distance at the surface strongly depends upon location. This is shown in Figures 32 and 33 where the surfaces are highly varying. For Euler all time steps follow the topography of the largest time step (yellow), this is, unfortunately not clearly shown in the figure. Also, for the largest time step of the midpoint method (Figure 33), I have the same "aliasing" effect as for the two previous models, while the other time steps give only relatively small differences.

Figure 34 shows the means for the small scale perturbation model, which are very similar to those computed for the large scale model, where Euler's method clearly gives unreliable results compared to the two other methods.

Figure 32: Difference in distance of the arrival positions at the surface between the fourth order Runge-Kutta and the different time steps of Euler's method as computed using the large scale 3D perturbation velocity model.
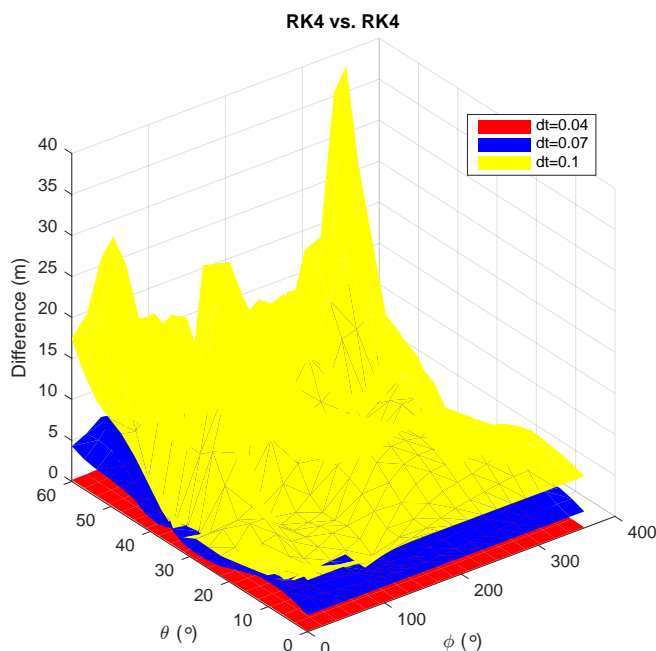
Figure 33: Difference in distance of the arrival positions at the surface between the fourth order Runge-Kutta and different the time steps of the midpoint method as computed using the large scale 3D perturbation velocity model.

Figure 34: Mean difference in distance at the surface between fourth order Runge-Kutta and the two numerical methods for a 3D velocity model with small scale perturbations. On the left plot, the mean for Euler's method is shown, while the mean for the midpoint method is shown in the plot on the right. Notice the difference in scale on the y-axis between the two numerical methods.

4.4.5   Fourth Order Runge-Kutta: One-Point Ray Tracing

The differences in ray arrival at the surface were also calculated for the fourth order Runge-Kutta. This was only done for the 3D velocity models with small scale perturbations, since the results vary the most for this velocity model. The results are shown in Figure 35, and are generally smaller than for the midpoint method. Also, it can be seen that dt=0.04s gives zero difference.

Figure 35: Differences in distance for the arrival position at the surface between the exact fourth order Runge-Kutta and different time steps of the fourth order Runge-Kutta as computed using the small scale 3D perturbation velocity model.

4.5   Two-Point Ray Tracing

For two-point ray tracing I want to investigate the difference between the three numerical methods (Euler, the midpoint method and fourth order Runge-Kutta) for rays arriving at fixed receivers. This is important, for example in travel time, amplitude and waveform modeling.

Hence, the arrival positions at the surface for the rays are the same for Euler, the

midpoint method and fourth order Runge-Kutta. As before, for this comparison I assume that a small time step dt=0.009s of fourth order Runge-Kutta, provides "exact" results. The times steps and velocity models used in the two-point ray tracing tests are the same as for the one-point ray tracing.

I use a hypocenter at the position: $x_s = 10000$m, $y_s = 10000$m and $z_s = -1700$m. The location is almost the same as that used for the seismic modeling in the next chapter.

For the 1D two-point ray tracing I chose to look at a line of receivers at the surface as the 1D ray tracing results are symmetric (see previous section). The line used starts at x=6000m and ends at the epicenter of the source which is at x=10000m.

For the 3D tests a grid of receivers was used. The grid spacing is 500m, and the size is 3km × 3km. The location of the grid is 7000-10000m in the x-direction and 8500-11500m in the y-direction.

The tests for the two-point ray tracing are different from those provided for the one-point ray tracing. First of all, it makes more sense to discuss difference in travel time for two-point ray tracing, since the rays arrive at the same position at the surface (receivers). Hence, travel time difference between the "exact" fourth order Runge-Kutta with a small time step and Euler/midpoint for the four different time steps were calculated.

Another test performed, was to check the trade-off between the slowness vector for the exact ray tracing and the two other methods at the receivers. For this test, the angle between the slowness vectors at the receivers were calculated using the dot product. These angles are given in degrees.

Also, it is interesting to investigate the amplitude difference between the exact method and the two other numerical methods. For this thesis the amplitude is assumed to be: 1/raylength. This difference is given in percentage. This last test is performed by looking at differences in the take-off angles for the rays used when performing two-point ray tracing. This number is also given in percentage. For the 3D case I look at both take-off θ and ϕ, while for the 1D test I only look at the incidence angle θ.

The results from the one-point ray tracing is displayed differently than the results

from the two-point ray tracing. It is important to plot the results against the variables that are constant. For one-point ray tracing these constants are the take-off angles, while for two-point ray tracing the take-off angles are different, and the results are therefore plotted against the receiver locations.

In the next sections I only show figures from the midpoint method. The rest of the results are displayed in an appendix at the end of this thesis.

4.5.1   1D Velocity Model

The first two-point ray tracing tests were performed for a 1D velocity model. As a first test to see if there are any major differences between Euler, the midpoint method and the exact fourth order Runge-Kutta, I plot take-off angle vs. receiver locations. The results are displayed in Figures 36 and 37. For Euler and the midpoint method only the results from the largest time step (dt=0.1s) are plotted. Figure 36 shows that there is a clear difference between the fourth order Runge-Kutta and the largest time step of Euler. The differences are the largest for the receivers located furthest away from the source. In Figure 37 on the other hand the fourth order Runge-Kutta is plotted against the largest time step of the midpoint method, and the differences are small. Hence, the difference between Euler and fourth order Runge-Kutta are larger than for the midpoint method, as expected from my one-point ray tracing tests.

This suggests that the midpoint gives reliable results for almost all time steps. However, the travel time test gave worse results (except for the smallest time step). The results are displayed in Figure 38. The estimated noise for the tomography provided by Gritto et al. (2013) is 0.01s, hence I set this as the accepted difference in travel time. All time steps (except the smallest time step) show larger values. Therefore these time steps should not be used when performing two-point ray tracing. The results obtained for Euler's method are surprisingly similar to those provided for the midpoint method, and are shown in Figure 68 (appendix).

Figure 39 shows the angle between the slowness vectors at the surface between the fourth order Runge-Kutta and the midpoint method. The results are given in degrees. In the figure it can be seen that these differences are very small for the 1D velocity model. The weird looking "jumps" on the curves, are probably caused by errors in the linear interpolation, which is used to compute take-off angles to the given receivers (interpolation was done using Delaunay triangulation: as described in the previous sections). The corresponding results for Euler's method are shown in

Figure 69 (appendix). The values are larger than for the midpoint method, but still relatively small. From the figure it can be seen that the angles calculated for Euler's method gradually increase for distances further away from the source. The actual upper bound of the error in the slowness vectors can only be assessed by computing waveforms.

Figure 40 shows the amplitude difference between the exact results and the different time steps of the midpoint method, the results are given in percentage. Where the smallest time step gives accurate results. For Euler's method the corresponding results are displayed in Figure 70 (appendix). The errors are a little bit larger for Euler than for the midpoint method, but not much.

The last test shows the difference in take-off angle at the source for the rays arriving at the receivers, the results are displayed in Figure 41 for the midpoint method and Figure 71 (appendix) for Euler's method. The errors for Euler's method range from approximately 0.5 - 6%, while these errors are considerably smaller for the midpoint method and only range from 0-0.7%. For the largest time step of the midpoint method in Figure 41 the previously mentioned "aliasing" effect can be seen, where the ray tracing skips an important velocity value.
.
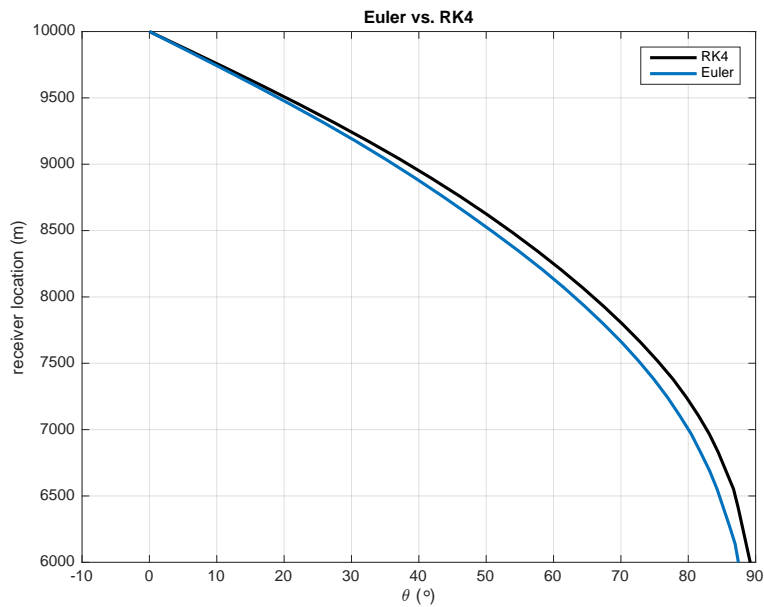
Figure 36: Receiver location vs. takeoff angle for fourth order Runge-Kutta vs. largest time step of Euler as computed using the 1D velocity model.
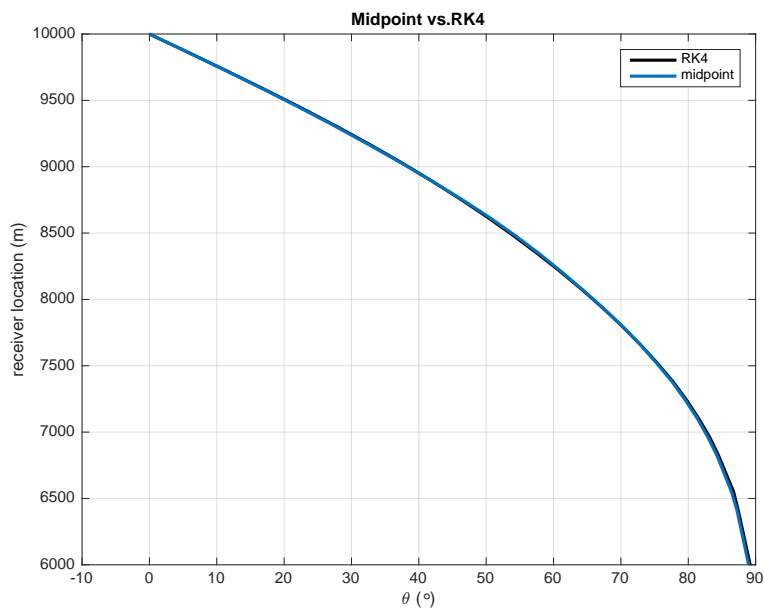
Figure 37: Receiver location vs. takeoff angle for fourth order Runge-Kutta vs. largest time step of the midpoint method as computed using the 1D velocity model.
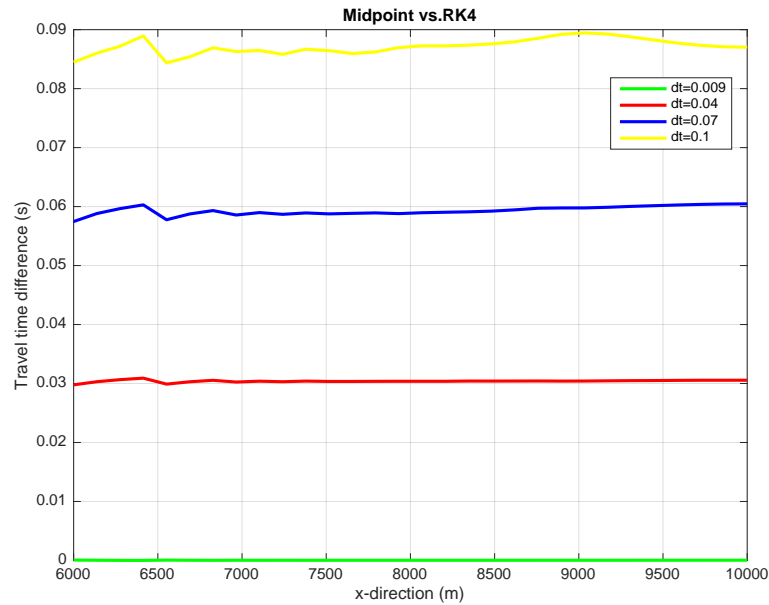
Figure 38: Travel time differences for the midpoint method vs. fourth order Runge-Kutta as computed using the 1D velocity model.
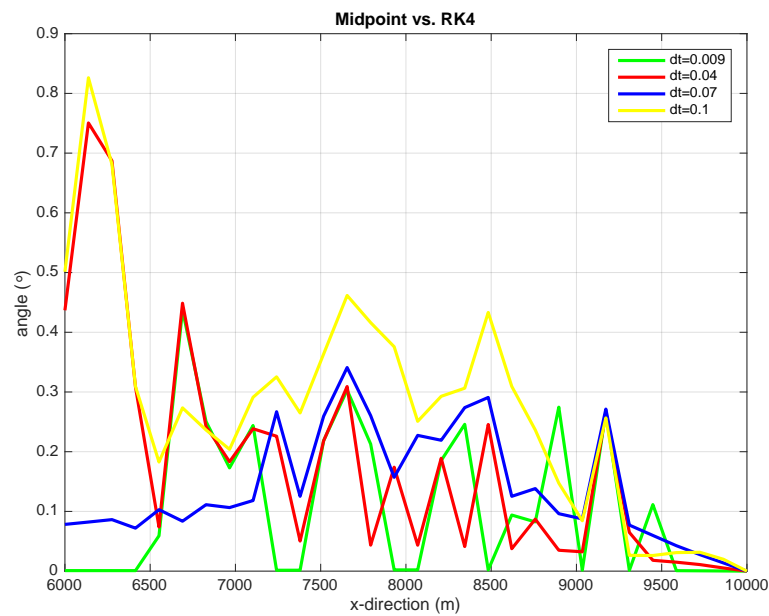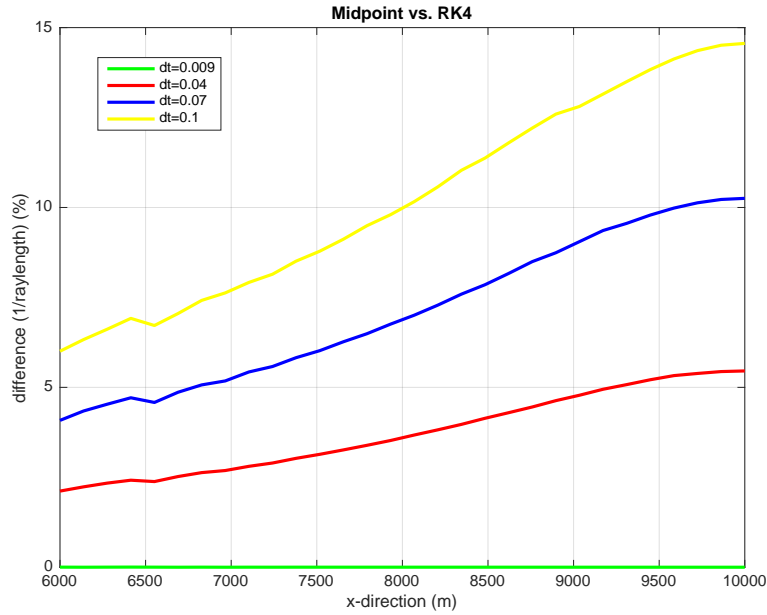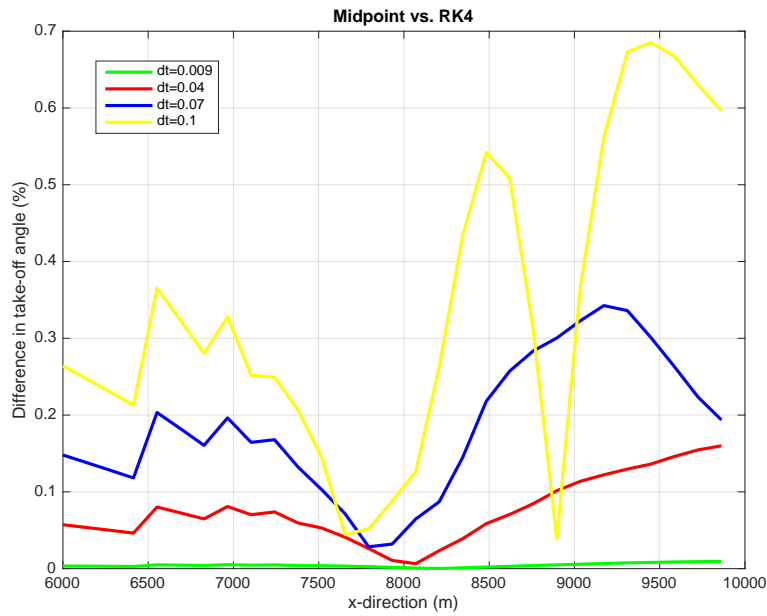

Figure 39: Angle between slowness vector at the surface for the midpoint method vs. fourth order Runge-Kutta as computed using the 1D velocity model.

Figure 40: Amplitude differences for the midpoint method vs. fourth order Runge-Kutta as computed using the 1D velocity model.

Figure 41: Differences in takeoff angle for the midpoint method vs. fourth order Runge-Kutta as computed using the 1D velocity model.

4.5.2   Large Scale Perturbations

The tests were also performed using a 3D velocity model with large scale perturbations. Instead of the line of receivers used for the 1D velocity model, I used a grid of receivers for the 3D velocity model tests.

Also, for the 3D test as for the 1D test, the midpoint method gave disappointing results in terms of travel time. The results are displayed in Figure 42, and show differences in travel time between the exact fourth order Runge-Kutta and different time steps of the midpoint method. Only the smallest time step of the midpoint method gives reliable results, while the other time steps give inaccurate results as defined in the previous subsection. The Euler method gives a similar outcome and is displayed in Figure 72 (appendix). However, the errors from Euler's method are slightly larger than for the midpoint method.

The angle between the slowness vectors at the surface for the fourth order Runge-Kutta and different time steps of the midpoint method, are displayed in Figure 43. The angles are small. The results from the Euler test are shown in Figure 73 (appendix). The angles for Euler's method are larger than the midpoint method and range from approximately $0.5°$ as the smallest value to $6°$ as the largest value.

Figure 44 shows the amplitude difference for the midpoint method, while Figure 74 (appendix) shows the corresponding test when using Euler's method. For the results it can be seen that Euler's method generally has a larger amplitude difference than the midpoint method. However, these differences are not large. The amplitude differences for the large scale 3D velocity model are similar to those given by the 1D velocity model.

The last comparison is the difference in take-off angle for the numerical methods. This is given in percentage. For the 3D velocity models both ϕ and θ need to be considered. In this section, I only give the difference in incidence take-off angle θ for the midpoint method, which are shown in Figure 45. The rest of the results can be found in the appendix and are shown in Figures 75, 76 and 77. The differences are small for both the midpoint method and Euler's method. Also, for this test the differences are slightly larger for Euler than the Midpoint method.
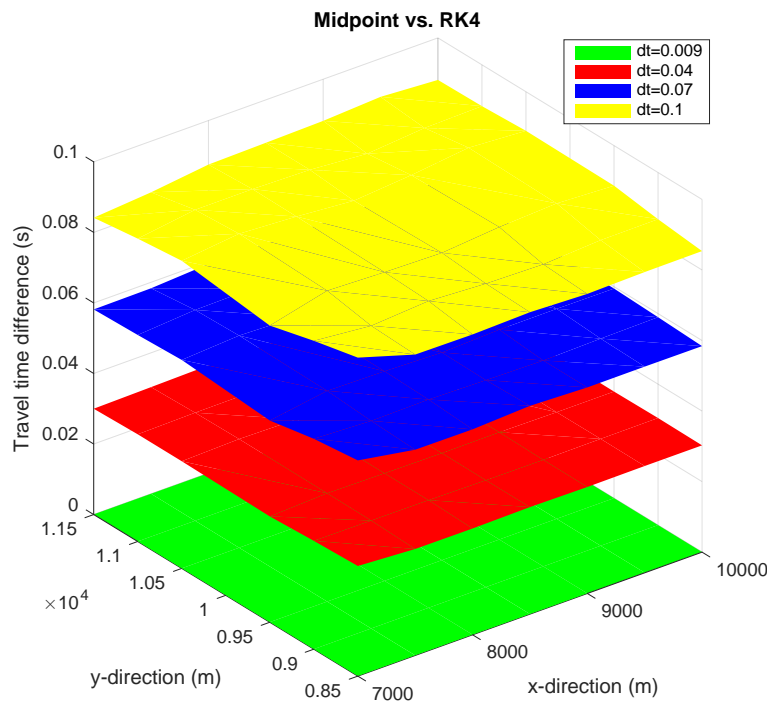
Figure 42: Travel time differences for the midpoint vs. fourth order Runge-Kutta as computed using the large scale 3D perturbation velocity model.
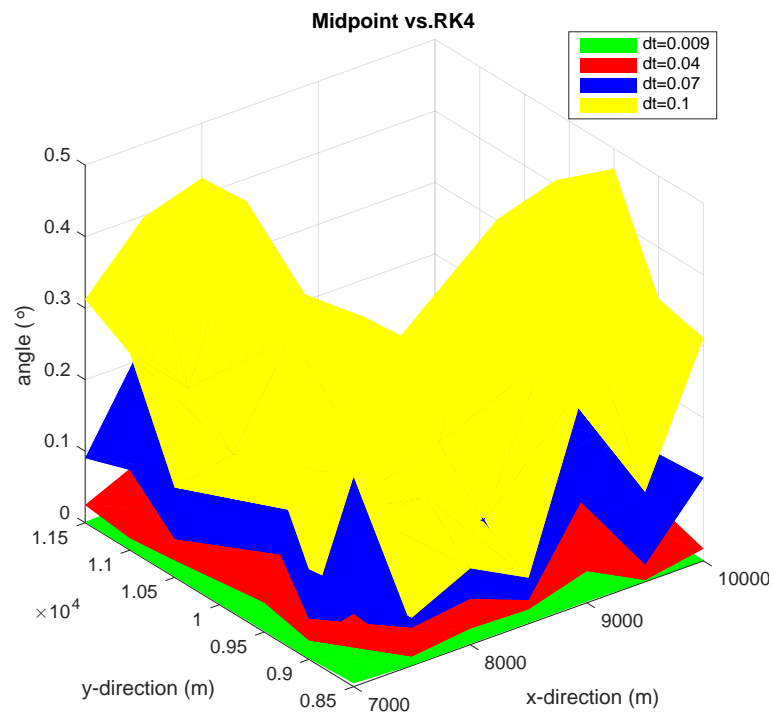
Figure 43: Angle between slowness vectors for the midpoint vs. fourth order Runge-Kutta as computed using the large scale 3D perturbation velocity model.
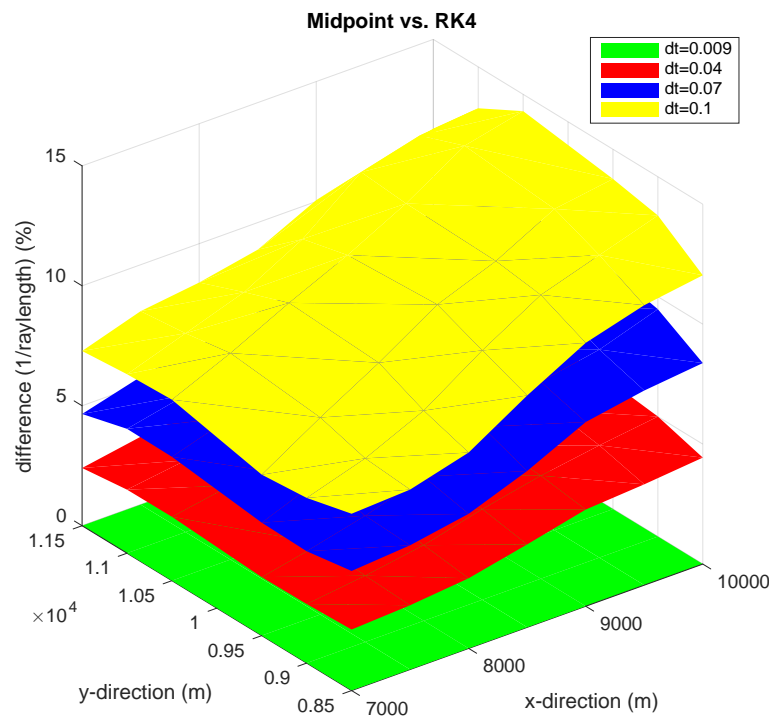
Figure 44: Amplitude differences for the midpoint method vs. fourth order Runge-Kutta as computed using the large scale 3D perturbation velocity model.
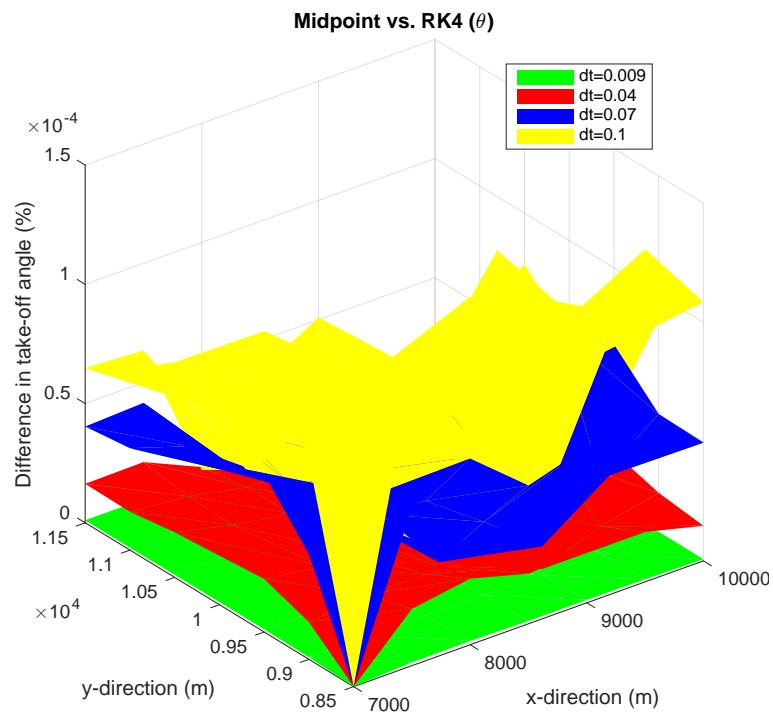
Figure 45: Difference for θ in percentage the midpoint method vs. fourth order Runge-Kutta as computed using the large scale 3D perturbation velocity model.

4.5.3   Small Scale Perturbations

All tests as previously described for the for the 3D large scale perturbation velocity model, were also performed on the 3D velocity model with small scale perturbations.

As for the two other velocity models, the midpoint method provides unreliable results in terms of travel time, except for the smallest time step. The results are shown in Figure 46, where travel time difference between the fourth order Runge-Kutta and the midpoint method can be seen. The errors for Euler's method are larger, and are displayed in Figure 78 (appendix). Also, in this figure the results are highly varying, which are caused by the variations in the small scale velocity model.

Figure 47 shows the angle between the slowness vectors at the surface between the fourth order Runge-Kutta and the midpoint method. The figure generally shows small angles between the slowness vectors, except for a peak for the largest time step, which might be caused by the "aliasing effect". The results from the Euler test are highly variable and shown in Figure 79. From the test it can be seen that the angles close to the source are generally quite small. Further away from the source, the angles are much larger and vary considerably. This might be caused by the fact that possibly not all the rays arrive at the exact receiver location. This is unfortunately often the case for velocity model with a lot of changes, and is most likely caused by multipathing, which occurs for distances far from the source. It is useful to note that the differences here are larger than in the large scale velocity model.

The next test performed was for the amplitude, and the results are given in percentage. The results for the midpoint method are displayed in Figure 48. For the midpoint method I have similar numbers as for the two other velocity models, where the smallest time step gives almost zero difference, while the larger time steps give higher error. The results for the Euler method are similar to those provided for the midpoint method, and are shown in Figure 80. However, at the edges there are jumps, which are caused by multipathing.

For the last test, I look at the difference in take-off angle between the fourth order Runge-Kutta and the midpoint/Euler method. The results for the incident take-off angle θ for the midpoint method are displayed in Figure 49. The differences are very small and are insignificant. The rest of the figures from this test are displayed in Figures 81, 82 and 83 in the appendix. These figures also show that there are only small differences in take-off angles for both θ and ϕ. These numbers are a little larger for Euler's method than for the midpoint method.
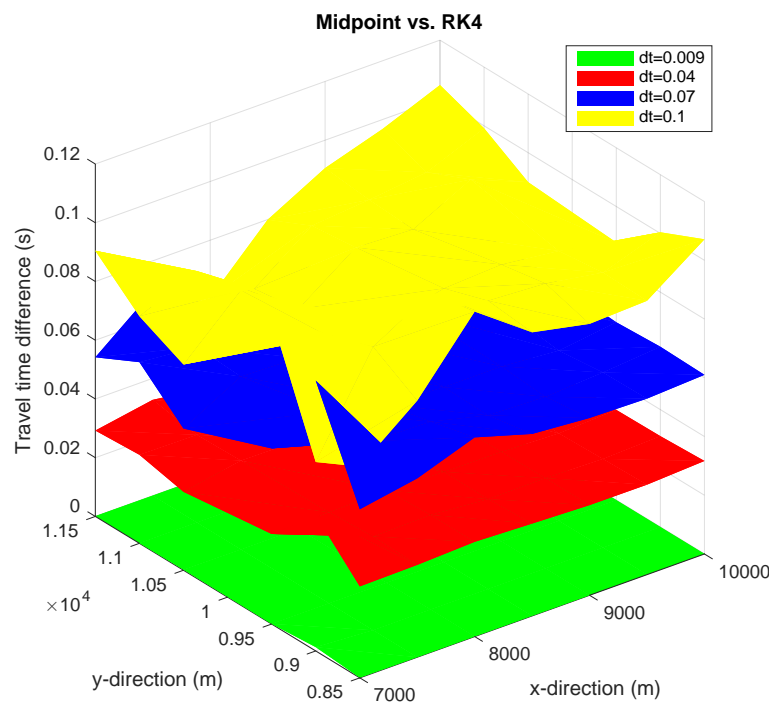
Figure 46: Travel time difference for the midpoint method vs. fourth order Runge-Kutta as computed using the small scale 3D perturbation velocity model.
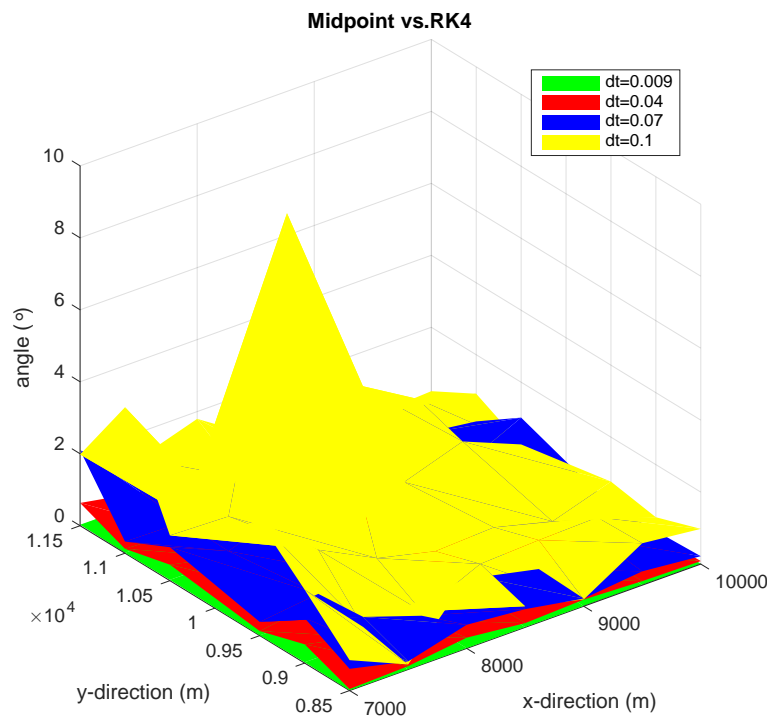
Figure 47: Angle between slowness vectors for the midpoint method vs. fourth order Runge-Kutta as computed using the small scale 3D perturbation velocity model.
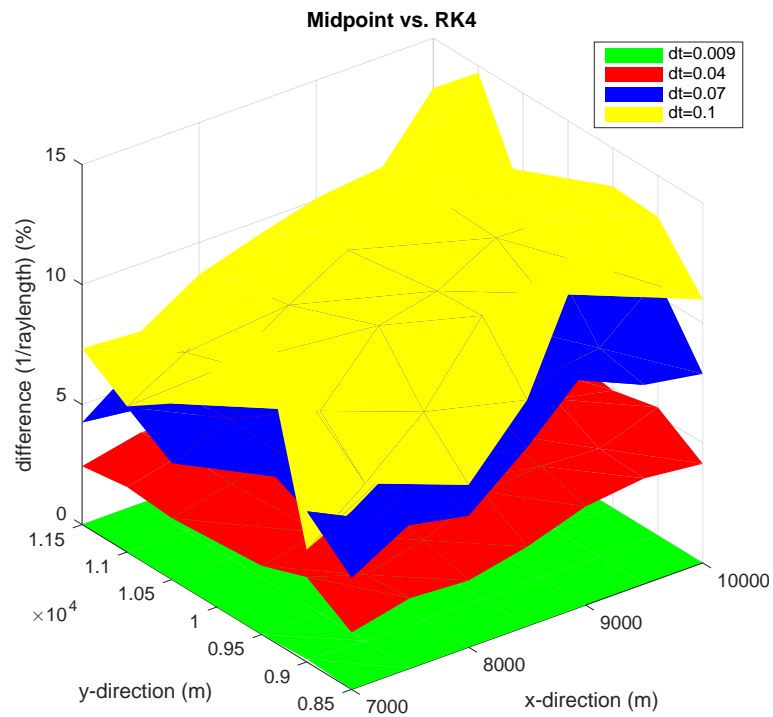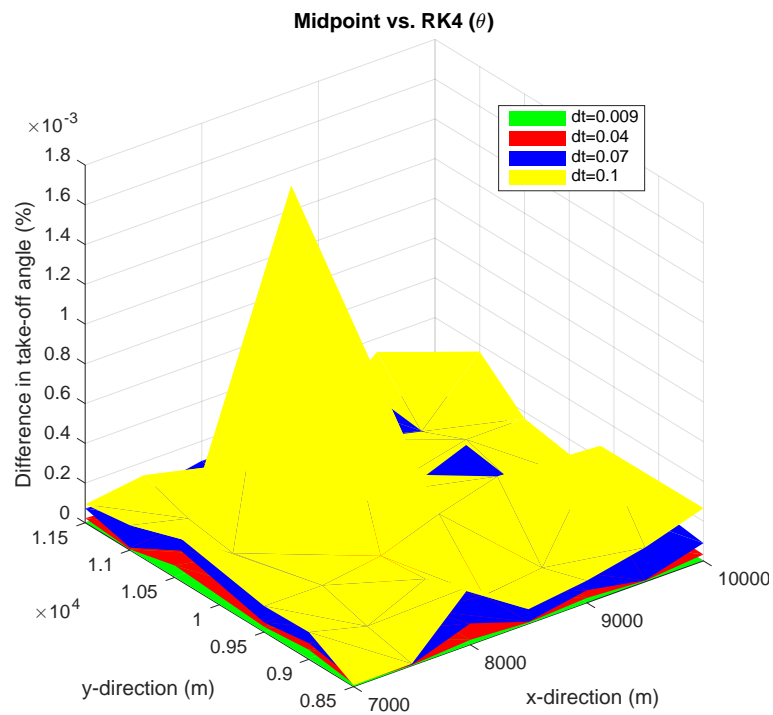
Figure 48: Difference in amplitude (1/raylength) for the midpoint method vs. fourth order Runge-Kutta as computed using the small scale 3D perturbation velocity model.

Figure 49: Difference for θ for the midpoint vs. fourth order Runge-Kutta as computed using the small scale 3D perturbation velocity model.

4.5.4   Fourth order Runge-Kutta: Two-Point Ray Tracing

As for the one-point ray tracing test, I chose to only look at fourth order Runge-Kutta for the 3D small scale velocity model. Here I only focus on travel time. The results are shown in figure 50. Also, the fourth order Runge-Kutta method gave disappointing results in terms of travel time, where dt=0.04s gives a travel time difference of 0.03 seconds, which is larger than the accepted limit of 0.001s.
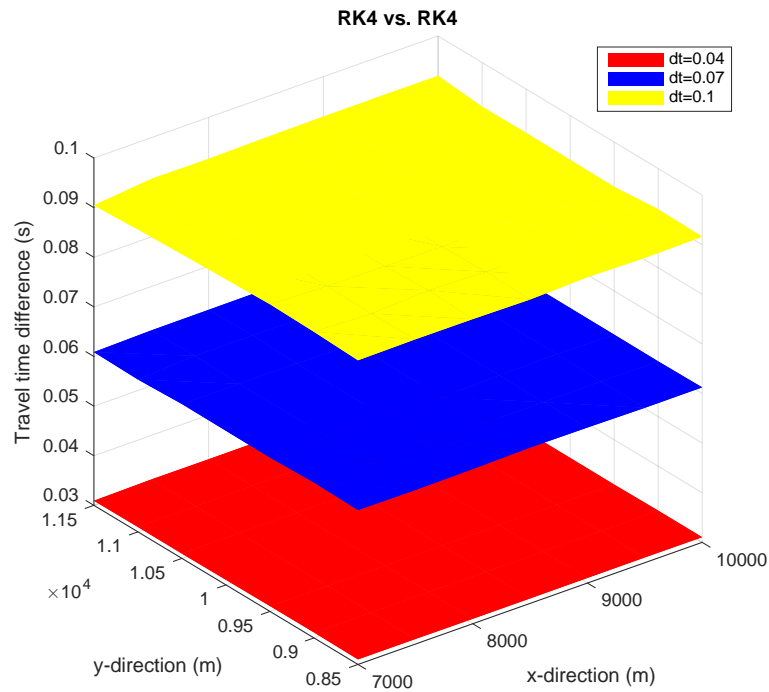
Figure 50: Travel time differences for the fourth order Runge-Kutta vs. fourth order Runge-Kutta as computed using the small scale 3D perturbation velocity model.

5 Elastic Waveform Modeling Using Ray Tracing

3D seismic synthetic tests for a geothermal reservoir, were performed in order to illustrate the use of the ray tracing methods provided in Chapters 3 and 4. The study area for this synthetic test is The Geysers geothermal reservoir in northern California. The Geysers is a hydrothermal system, but EGS technologies have been tested at the Prati-32 well in the northern part of The Geysers.

Essential information for this synthetic test is taken from the paper by Guilhem et al. (2014). In that paper, moment tensor inversions are performed for 15 M3 events. For calculation of the Green's tensors, Guilhem et al. (2014) use a layered 1D velocity model, which is an average of a 3D model (Figure 18). After having developed and tested several ray tracing algorithms, these algorithms can now be used to investigate differences between 1D and 3D velocity models. In order to do all this, I first discuss the numerical computation of Green's tensors, and the synthetic seismograms in sections 5.1 and 5.2. Then in section 5.3, the application of the waveform modeling algorithm to realistic 1D and 3D velocity models for double-couple and non-double couple models of The Geysers is presented.

5.1 Method

For this thesis when constructing synthetic seismogram the causal Ricker wavelet is used as the source wavelet:

$$R(t) = (1 - t^2 f_0^2 \pi^2) e^{-t^2 \pi^2 f_0^2}. \tag{5.1}$$

Here t is time and f_0 is the center frequency, which in this thesis is 1Hz. The Ricker wavelet is often used when constructing synthetic seismograms due to its similarity to seismic sources. Figure 51 shows the Ricker wavelet that was used.

For construction of synthetic seismograms I use equation (2.50) provided in section 2.5.4:

$$\mathbf{u} = w(t - T_{rs}) \boxed{A_{rs} \boxed{(\mathbf{M} : \mathbf{p}_s \mathbf{p}_s)} \mathbf{p}_r}. \tag{5.2}$$

In this thesis I focus on the computation of P-waves. The P-wave synthetic seismograms are calculated in three steps. As a first step, I use the expression in the inner-box of the equation, which represents the radiation pattern at the source. The
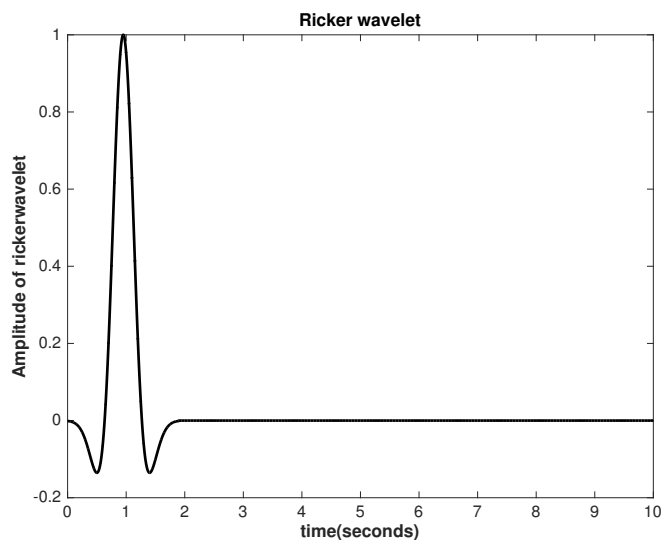
Figure 51: The Ricker wavelet with $f_0 = 1Hz$.

radiation pattern depends upon the seismic moment tensor source $\mathbf{M}$, which is found using equation (2.37). In order to use equation (2.37), I define a normal vector $\mathbf{n}$ and a slip vector $\mathbf{d}$. For the second step, I am interested in the radiation pattern and amplitude A_{rs} which includes the effects of the wave propagation throughout the velocity model as computed by ray tracing at the receiver. The expression for this is shown in the outer-box of equation 2.50. I only compute the z-component. For the last step, synthetic seismograms are calculated. This is done including the last term, and includes the Ricker wavelet and travel time, which is computed using ray tracing.

5.2   Velocity Models and Sources Used in Synthetic Test

For this synthetic test on of the main goals is to check trade-off between 1D and 3D ray tracing. The 1D velocity model used is the layered velocity model shown in Figure 18, while the 3D model is constructed adding large scale Gaussian perturbations to the 1D model (correlation length: 500m, perturbation strength: 7%). The 3D velocity model is displayed in Figure 52.

A list of the 15 M3 earthquakes investigated by Guilhem et al. 2014 is shown in Figure 54. The earthquake used for this test is marked with a red box. This hypocenter

is at the position: $x_s = 11357$m, $y_s = 9812$m, $z_s = -1725$m.

For this test, a grid of receivers at the surface with a spacing of 500m is used. For the receiver locations I want to cover as much as possible of the area shown in Figure 53. The receivers are located between 9000-12500m in the x-direction and 7500-12500m in the y-direction. The total number of receivers are 88. The numerical method used for the two-point ray tracing, is the midpoint method with the small time step (dt=0.009s), which from the previously provided comparison between Euler, the midpoint method and fourth order Runge-Kutta is my preferred method.

For the synthetic test, the seismic sources are chosen to be a pure double couple source and a double couple source with a non-double couple component, since this is the trend for the earthquakes investigated by Guilhem et al. 2014. The double couple earthquake, is a strike slip earthquake with a normal vector: $\mathbf{n} = [1, 0, 0]$ and slip vector $\mathbf{d} = [0, 0, 1]$, where the angle between the vectors is 90°. Using the relation (2.37) I get the moment tensor:

$$\mathbf{M} = \begin{bmatrix} 0 & 0 & 1 \\ 0 & 0 & 0 \\ 1 & 0 & 0 \end{bmatrix}.$$

While for the double couple earthquake with a non-double couple component I have $\mathbf{n} = \frac{2}{\sqrt{6}}(1, 0.5, 0.5)$ and $\mathbf{d} = \frac{2}{\sqrt{6}}(0.5, 0.5, 1)$. Here the angle between the normal and slip vector is 33.1°. This gives the moment tensor:

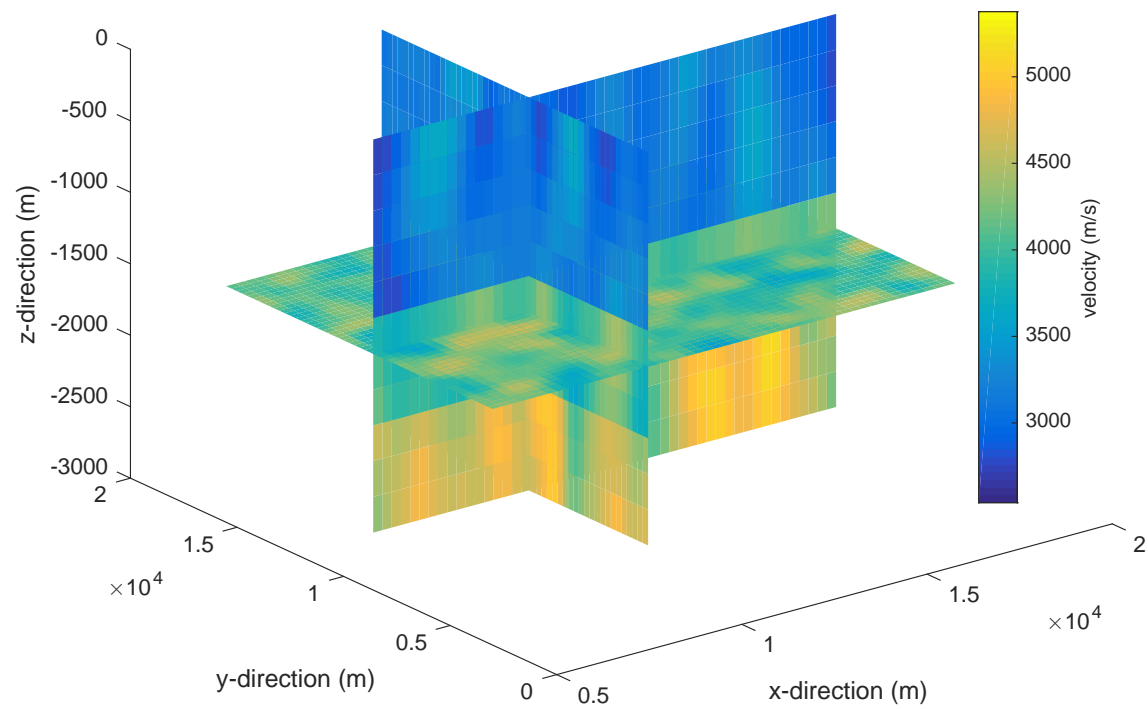$$\mathbf{M} = \begin{bmatrix} 0.67 & 0.5 & 0.83 \\ 0.50 & 0.33 & 0.5 \\ 0.83 & 0.5 & 0.67 \end{bmatrix}.$$

Figure 52: 3D velocity model used for the synthetic test. When constructing the Gaussian perturbations a correlation length of 500m and a perturbation strength of 7% was used.
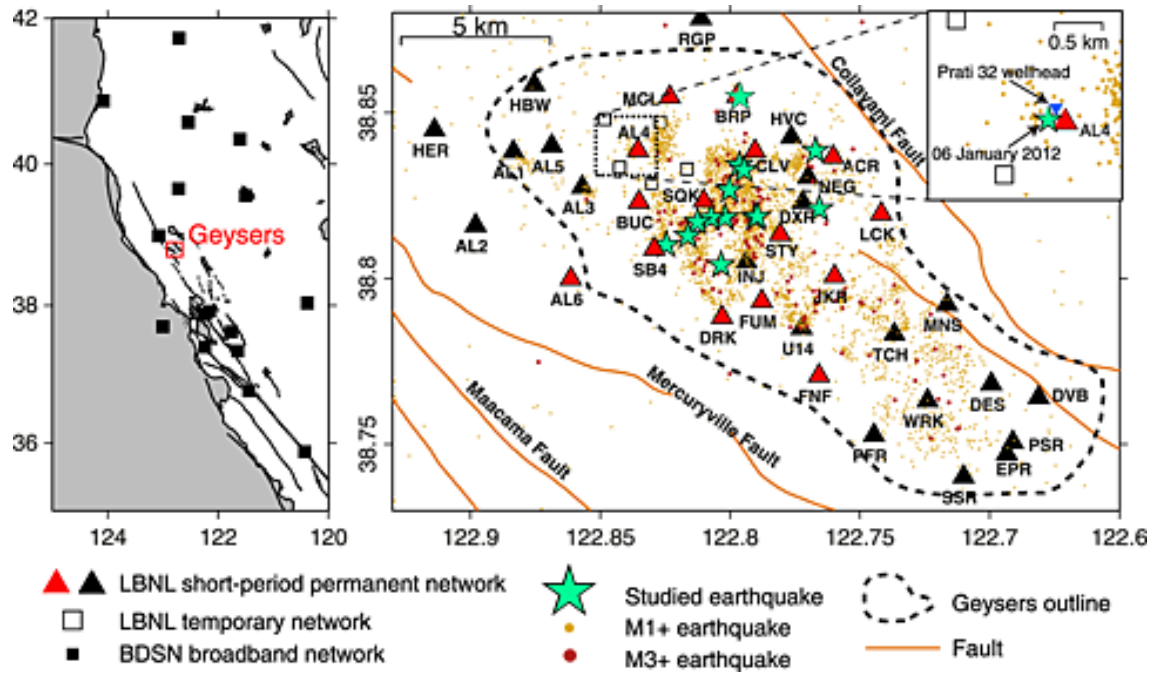
Figure 53: Location of The Geysers geothermal reservoir in northern California (Guilhem et al. 2014).

Date	Lat	Lon	Depth (km)	M LBNL	Ml USGS	Mw BSL	Mw 0.7–1.7 Hz	Mw 0.5–2.5 Hz	Number of Stations	Azimuthal Gap
2009/11/24	38.8184	−122.7904	2.585	3.55	3.41	3.67	3.52	3.55	5	110
2010/1/30	38.8342	−122.7964	3.137	3.61	3.42	3.61	3.62	3.54	4	274
2010/3/4	38.8385	−122.7671	1.845	3.31	3.29	3.41	3.45	3.41	5	198
2010/3/28	38.8102	−122.8245	2.967	3.39	3.26	3.65	3.73	3.67	5	207
2010/4/27	38.8184	−122.8021	1.725	3.15	3.23	3.49	3.31	3.17	6	158
2010/7/15	38.8183	−122.8074	3.251	3.77	3.66	3.95	3.92	3.88	6	110
2010/7/15	38.8171	−122.8125	2.902	3.59	3.51	3.83	3.90	3.89	5	207
2010/7/28	38.8187	−122.7895	3.991	3.34	3.22	3.31	3.32	3.29	5	158
2010/8/15	38.8210	−122.7656	1.717	3.36	3.33	3.33	3.32	3.34	5	204
2010/10/19[a]	38.8547	−122.7961	1.690	3.52	3.41	3.54	-	-	-	-
2010/12/6	38.8041	−122.8035	1.784	3.55	3.61	3.71	3.77	3.80	5	132
2011/3/1[b]	38.8165	−122.8194	3.620	4.03	3.93	4.43	-	-	-	-
2011/4/23	38.8335	−122.7927	3.247	3.35	3.15	3.38	3.43	3.32	4	107
2011/4/26	38.8129	−122.8163	3.659	3.69	3.53	3.90	3.95	3.87	6	92
2011/9/17	38.8266	−122.8003	3.913	3.48	3.38	3.38	3.40	3.37	5	164

[a]Seismic event with very limited seismic data.
[b]An earthquake too large to provide accurate results in the moment tensor analysis given the distance range and frequency bands considered in our study.

Figure 54: The figure shows all the magnitude 3 events between November 2009 and December 2011 at The Geysers geothermal reservoir. The red box represents the earthquake, for which this synthetic test was performed. Modified from Guilhem et al. 2014.

5.3 Waveform Modeling at The Geysers

5.3.1 Double Couple Source

The first synthetic test was performed for a strike-slip earthquake. To check differences in results for the seismic sources and trade-off between the 1D and 3D velocity models the P-wave synthetic seismograms are constructed in three steps as discussed in section 5.1. First the P-wave radiation pattern at the source was calculated, which is shown in Figure 55. The radiation pattern is represented by four lobes, which is characteristic for the pure double couple source (see e.g Pujol 2003).

Figure 56 and 57 show the combined effects of radiation pattern and geometrical spreading (the outer-box in section 5.1) at the receivers for the 1D and 3D velocity models. It is difficult to see clear differences between the two figures. Therefore, in Figure 58 I have calculated the amplitude ratios between the 1D and 3D velocity models at the receivers. It can be seen that the differences are larger for some areas, which is most likely caused by the random position of the perturbations. Since there are amplitude differences between the 1D and 3D velocity models, there will also be differences in the calculated synthetic seismograms.

At a final step, synthetic seismograms were calculated for both the 1D and 3D ray tracing at the 88 stations. The synthetic seismograms for the z-component for one line of receivers (x=11500m and y=7500-12500m) are shown in Figure 59. The thin line represents the synthetic seismograms calculated for the 1D velocity model, while the thick line represents the synthetic seismograms for the 3D velocity model. The amplitudes are large close to the source, and gradually decrease as expected. Also, the amplitude differences between the 1D and 3D are easier to spot close to the source. A significant deviation for the calculated synthetic seismograms are shown at the positions y= 7500-8500m. Here there are polarity differences, where the 1D data is positive and 3D data is negative. To see these differences more clearly I display the synthetic seismogram for the x, y and z components at the location x=11500m and y=7500m in Figure 60. The polarity clearly deviates for all the components. These deviations are significant, and would affect the results from a potential moment tensor inversion in a negative manner.
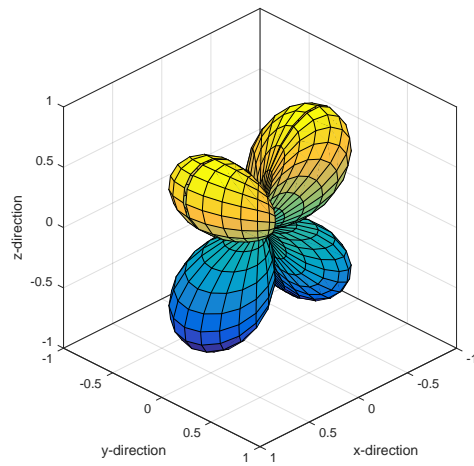
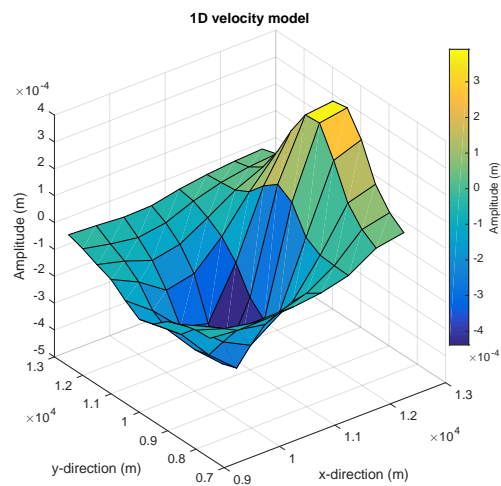Figure 55: Radiation pattern for a double couple source.

Figure 56: Amplitude at the surface for a double couple source for the 1D velocity model.
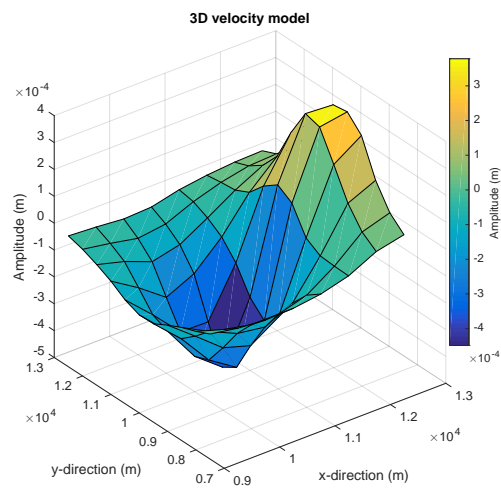
Figure 57: Amplitude at the surface for a double couple source for the 3D large scale velocity model.
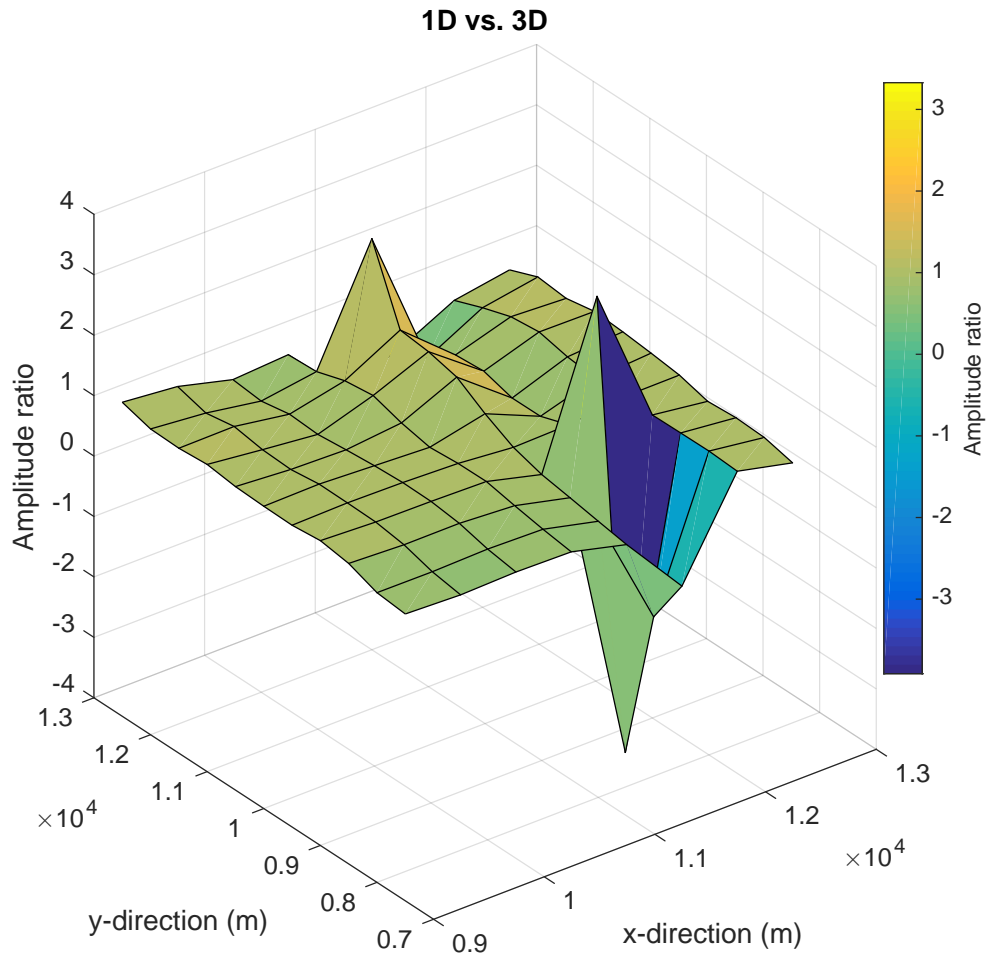
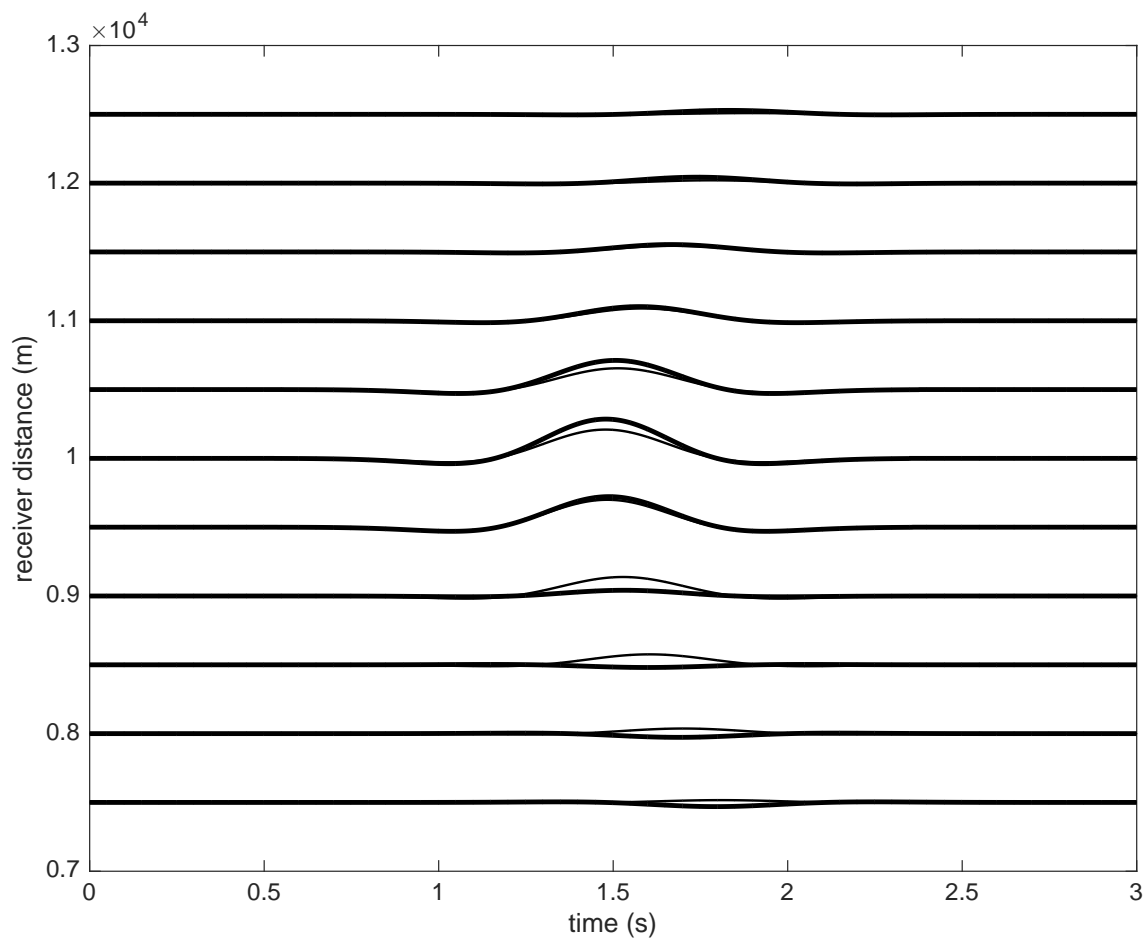Figure 58: Amplitude ratios for the 1D vs. 3D velocity models for the double couple source.

Figure 59: z-component of synthetic seismograms for a line of receivers for the double couple source (see text). The receiver line is shown for x=11500m and y=7500-1300m. The thin line represents the synthetic seismograms for the 1D velocity model, while the thick line represents the synthetic seismograms for the 3D velocity model.
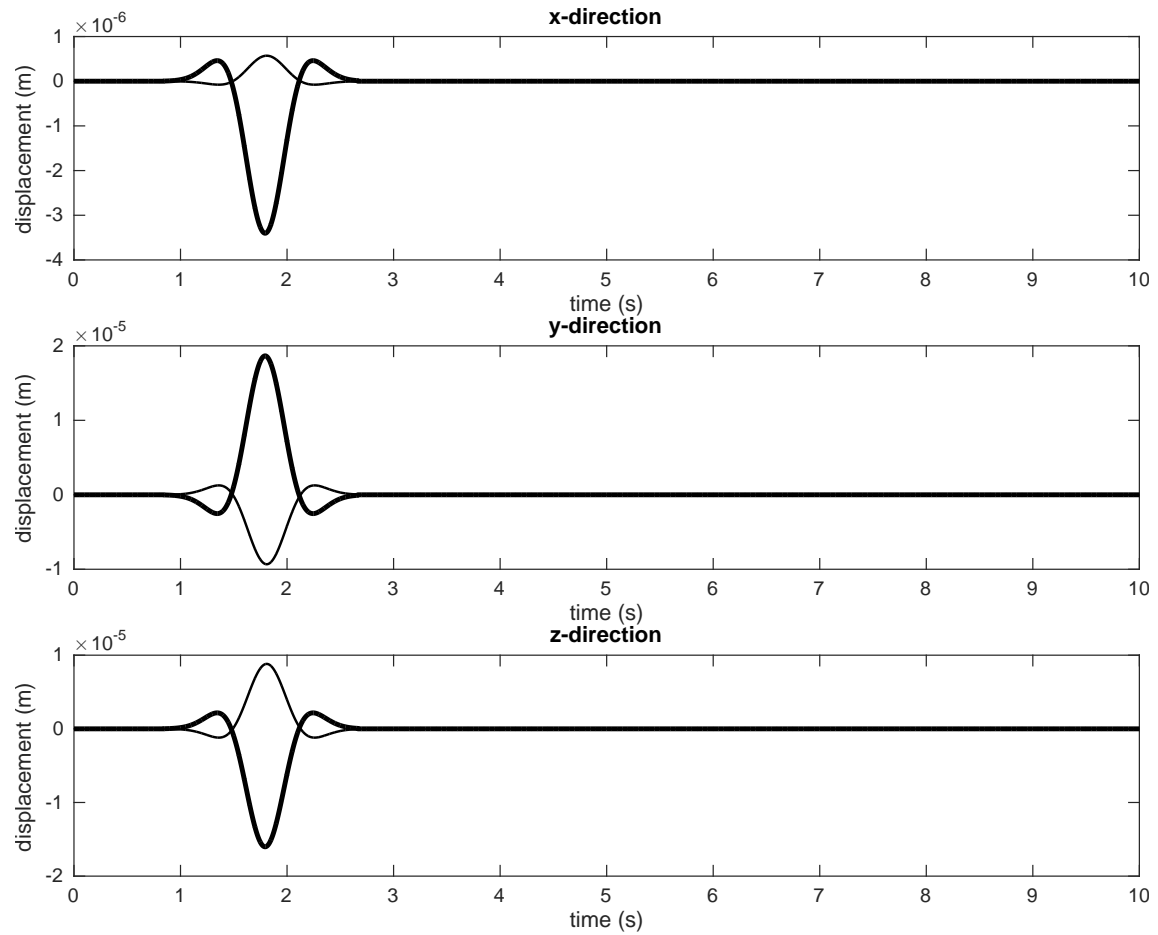
Figure 60: Synthetic seismogram for receiver at x=11500m and y=7500m for a double couple source. The thin line represents the synthetic computed using the 1D velocity model, while the thick line shows the calculated synthetic seismograms for the 3D velocity model.

5.3.2   Double Couple Source with a Non-Double Couple Component

The same procedure as for the double couple source was performed for the source with a non-double couple component. The radiation pattern at the source is displayed in Figure 61. There are only two lobes for the the non-double couple source, as supposed to the double couple source with four lobes (Figure 55).

As a next step, the amplitude at the receiver were calculated. These are shown in Figures 62 and 63. The differences are easier to spot than for the double couple source, for example for the largest amplitudes. The amplitude ratios are shown in Figure 64. Here it can be seen that there are clear difference between the amplitudes obtained by the 1D and 3D velocity models.

Also, notice that the amplitudes at the receivers are different for the double couple and non-double couple source. For the double couple source, the amplitude polarities are both negative and positive (Figures 56 and 57), while for the non-double couple source the amplitudes are mostly positive (Figures 62 and 63). Hence, the amplitude depends upon the seismic source as expected. This is also shown for the calculated synthetic seismograms, which are displayed in Figure 65. These seismograms are for the same receivers as the ones displayed in Figure 59. The results from the two different seismic sources are clearly different. For the receivers located between 11500-12500m, the amplitudes are larger for the double couple source, than for the non-double couple source. Also, it should be noted that the travel time differences between the 1D and 3D ray tracing gradually increase away from the source (see Figure 65).

In Figure 66 the seismograms for the same receiver as in Figure 60 are seen. However, for the seismogram displayed in Figure 66 both the 1D and 3D data have the same polarity. This indicated that the seismic source is significant for the final results.
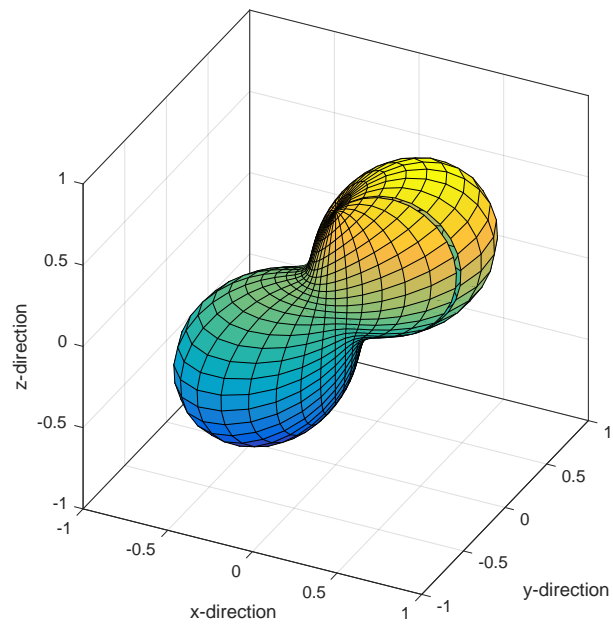
Figure 61: Radiation pattern for a double couple source with a non-double couple component.
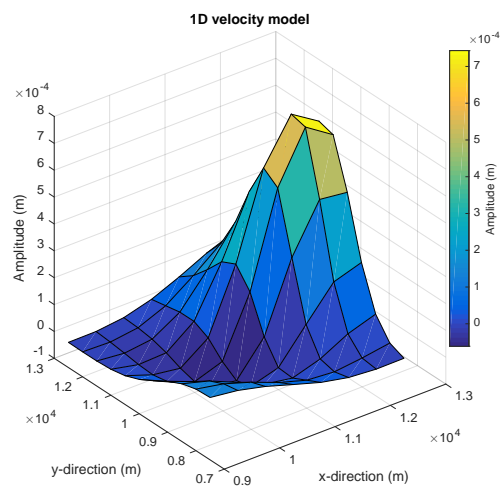

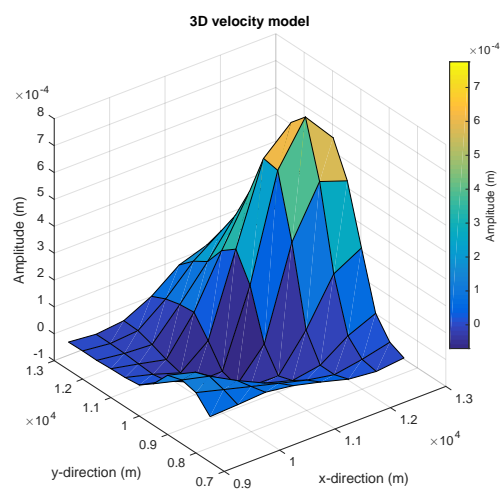Figure 62: Amplitude for a non-double couple source for the 1D velocity model.

Figure 63: Amplitude for a non-double couple source for the 3D large scale velocity model.
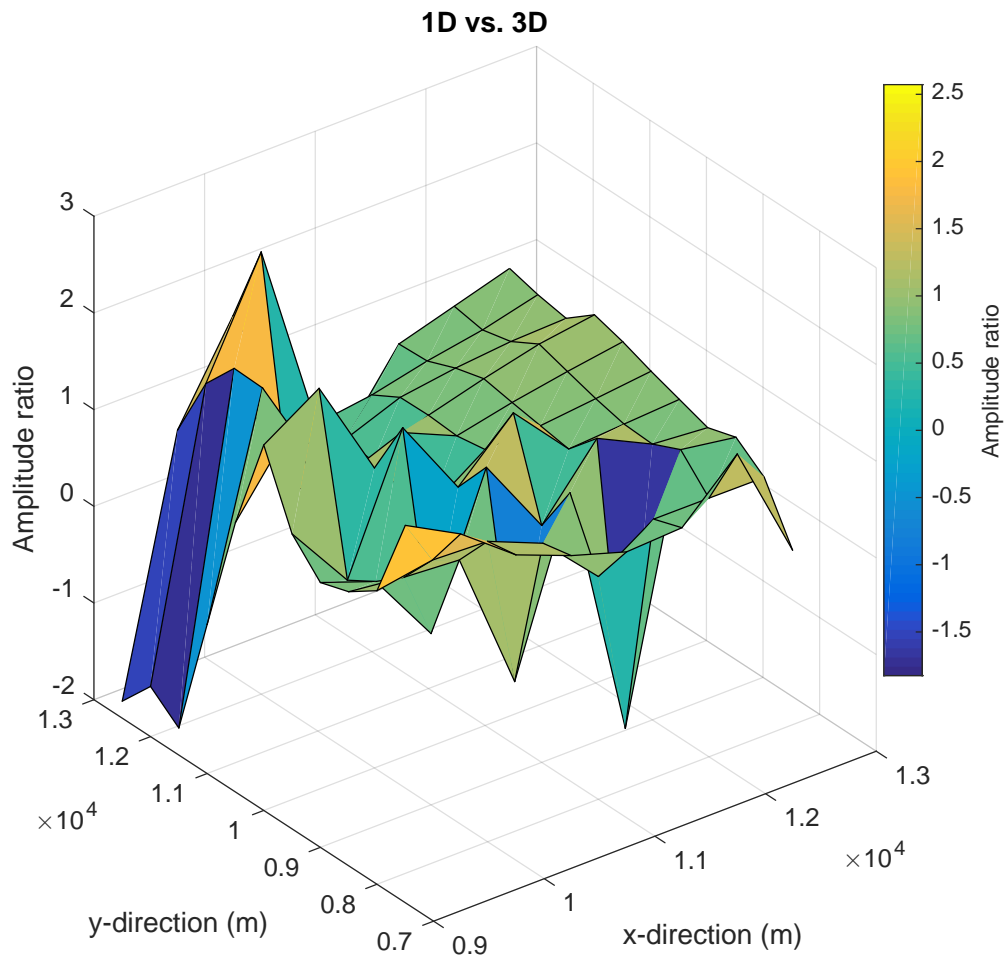
Figure 64: Amplitude ratios for the 1D vs. 3D velocity models for the source with a non-double couple component.
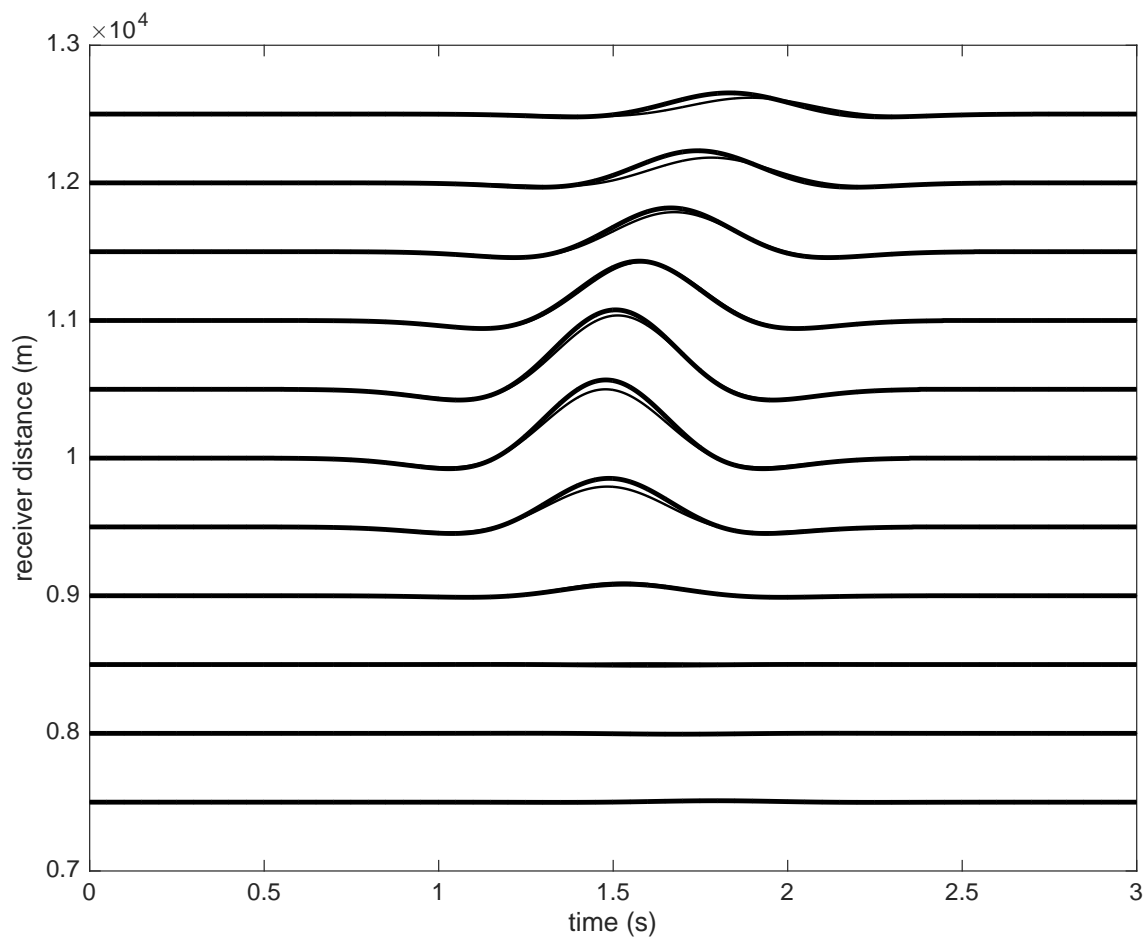
Figure 65: z-component of synthetic seismograms for a line of receivers for the non-double couple source (see text). The receiver line is shown for x=11500m and y=7500-1300m. The thin line represents the synthetic seismograms for the 1D velocity model, while the thick line represents the synthetic seismograms for the 3D velocity model.
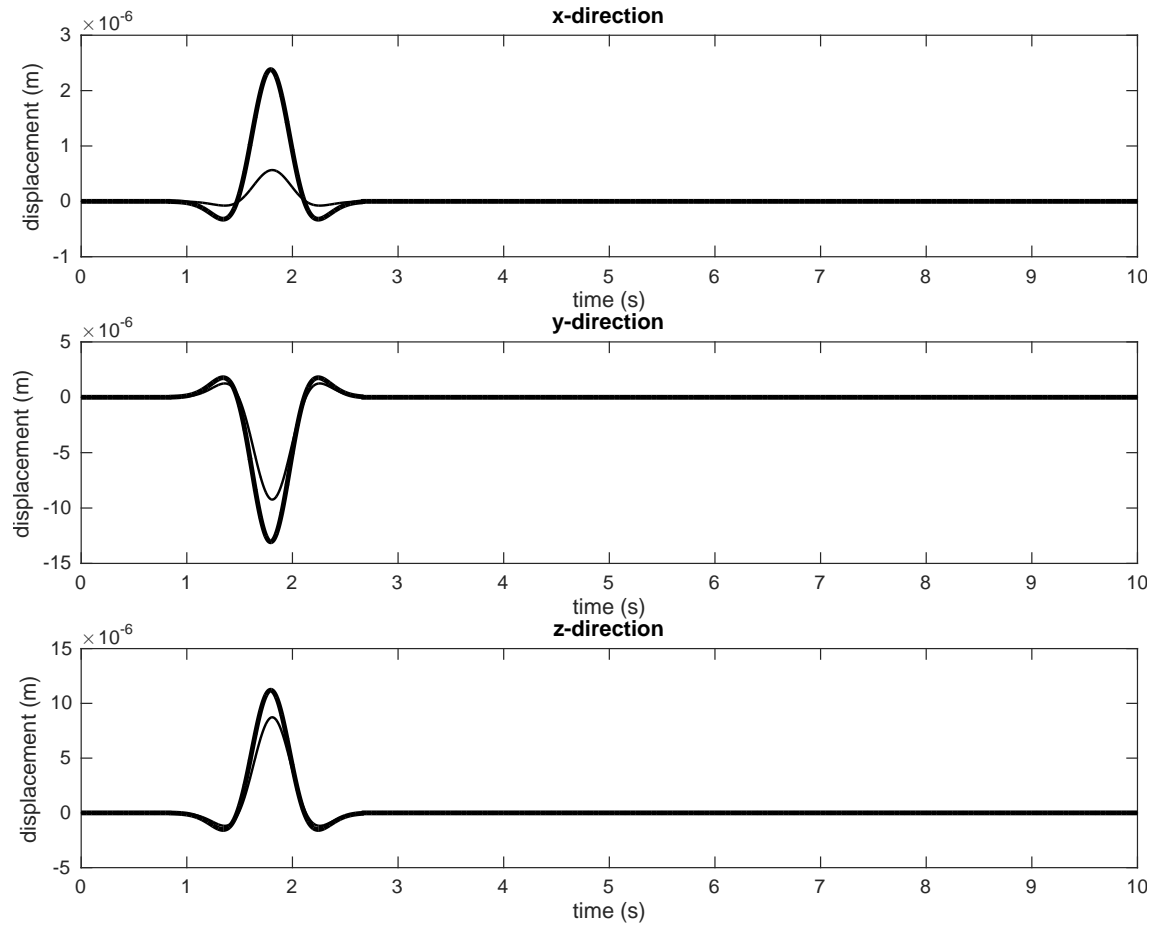
Figure 66: Synthetic seismogram for receiver at x=11500m and y=7500m for the non-double couple source. The thin line represents the synthetic computed using the 1D velocity model, while the thick line shows the calculated synthetic seismograms for the 3D velocity model.

6 Discussion

6.1 Microseismicity at Geothermal Reservoirs

The study of microseismicity at geothermal reservoirs is important for characterization. For example, permeable zones and orientation of fractures can be found by combining moment tensor inversion and earthquake location for micro-seismic events occurring at geothermal reservoirs. In order to perform moment tensor inversion, however it is important to have reliable velocity models.

In this thesis, I first made an overview of existing velocity models and other seismic studies performed at enhanced geothermal systems, since no such overview currently exists. From this overview it can be seen that there exist 1D velocity models for almost all reservoirs. However, this is not the case for 3D velocity models, which are only found at approximately half of the reservoirs. In this thesis I studied differences in 1D and 3D velocity models obtained using seismic waveform modeling results. An important step for efficient seismic modeling consisted of ray tracing, which was therefore studied in detail in this thesis.

6.2 Ray tracing

A systematic comparison between the three numerical methods for ray tracing, Euler, midpoint and the fourth order Runge-Kutta has been performed. From an extensive literature search, it seems like this comparison had not been done before. However, Nolet (2008) notes that the fourth order Runge-Kutta is often the preferred method for ray tracing, but if there are large velocity variations a second order Runge-Kutta (midpoint method) with a fine sampling rate can be used. However, he provides no further comparison between the two methods.

The comparison done for velocity models taken from The Geysers geothermal reservoir in California, showed that Euler deviates from both the midpoint method and the fourth order Runge-Kutta, and is found to be considerably worse than the two other methods. These variations are larger for more complex 3D velocity models, than the simpler 1D velocity models. This can in particularly be seen for the one-point ray tracing, where the arrival position at the surface for Euler's method deviates from the two other methods by hundreds of meters. For the two-point ray tracing, differences in travel time at the receivers for all three numerical methods were calculated. For this thesis, the maximum accepted travel time difference is set to 0.001s (Gritto

et al. 2013). This was obtained from travel time tomography at The Geysers. From this test, it was found that only the smallest time step dt=0.009s of the midpoint method and fourth order Runge Kutta gave reliable results in terms of travel time.

Another problem is related to the choice of too large time steps, is an "aliasing" effect, where ray tracing skips parts of the velocity model, hence giving false results. Small enough time steps should therefore be used in order to avoid this phenomenon. Generally, for all results the error increases for increasing take-off angles/receiver distances. For two-point ray tracing, especially for the small scale model there is multipathing for distances away far from the source.

From all the tests, I found that the fourth order Runge-Kutta and the midpoint method with a small time step (dt=0.009s) provide good results. The fourth order Runge-Kutta is time consuming and requires more calculations. Hence, the midpoint method with a smaller time step is the preferred method.

For these tests, two 3D velocity models with 3D Gaussian perturbations superimposed on the 1D velocity model from The Geysers were used. However, the results from these tests could have been improved by taking the average of 5-10 results, since these test results depend upon position of the perturbations, which is randomly constructed for every velocity model. The important point of the Gaussian perturbation velocity models is that they resemble models obtained using travel time tomography.

6.3 Waveform Modeling

Waveform modeling was performed to check differences between 1D and 3D waveforms and also to investigate differences in radiation pattern/amplitudes when using different seismic sources. For the tests presented in this thesis, two different seismic sources were used: A double couple source, and a (double couple) source with a large non-double couple component.

From the calculated amplitudes/radiation patterns at the receivers, it can be seen that there is a different radiation pattern for the double couple and the double couple source with a non-double couple component. Hence, the amplitudes at the receivers depend significantly upon the seismic source. These differences also affect the synthetic seismograms, with significant amplitude variations at the receiver locations.

For the synthetic seismograms there are clear differences in obtained results between the 1D and 3D ray tracing. The most crucial differences are polarity differences for some of the synthetic seismograms between 1D and 3D data. Hence, therefore I suggest that 3D velocity models should be used, rather than a 1D velocity model, when studying moment tensors.

Johnson (2014) investigated micro-seismic earthquakes related to fluid injection at the northern area of The Geysers. By investigating different moment tensors, he made a source model for induced earthquakes. The source model aimed at predicting whether fractures are being opened or closed. For this prediction, it is crucial that accurate moment tensors are estimated. If a 1D velocity models is used, the wrong conclusion can be made, and in the worst case scenario a zone that is impermeable can be interpreted as permeable or vice versa.

6.3.1   Alternative Numerical Methods

Another ray tracing method is the step size adaptive Runge-Kutta method. For this method the sampling rate (time step) varies along the ray path. This technique can be expensive, since a new time step has to be found for every calculation. The method is not used in this thesis, since I do not assume large variations in the scale of the 3D velocity models (as provided for example by travel time tomography).

An alternative to solving the wave equation, is provided by finite difference modeling (or other fully numerical methods), which is more accurate. However, this method is very time consuming compared to ray tracing. Gritto et al. (2013) note that since the LBNL (Lawrence Berkeley National Laboratory) permanent seismic network was installed at the The Geysers geothermal reservoir in 2003 over 125000 micro seismic events have been detected. Since a lot of data has to be processed, a fast modeling method is very helpful. Another advantage with ray tracing is that effects such as anisotropy and attenuation can be easily incorporated. However, a comparison of the modeling method presented in this thesis with a fully numerical method, would still be useful.

6.4 Further Improvements

6.4.1 Amplitude

For this thesis I assume the amplitude to be 1/raylength. However, some of the velocity models used for this thesis are weakly heterogeneous and the results could be improved by solving the transport equation (equation 2.14).

6.4.2 Computation Time

The computation time varies significantly for the three different methods. Fourth order Runge-Kutta is very slow, while the two other methods are quicker in terms of computation time. This is mostly due to the large number of spline interpolations used for calculation of the fourth order Runge-Kutta. The fourth order Runge-Kutta uses twice as many spline interpolations as the midpoint method, and four times as many as Euler's method. Since the spline interpolations is the most time consuming operation, this also means that the computations for fourth order Runge-Kutta are twice as expensive as the midpoint method for the same time step.

My implementation of the ray tracing was in MATLAB. By implementing the code using other programing languages, such as Fortran or C^{++}, the computation time will be significantly reduced.

6.4.3 Multipathing and Scattering

For heterogeneous 3D media with strong perturbations multipathing occurs for the ray tracing algorithm. Therefore, for strong perturbations the results obtained from the two-point ray tracing is non-unique, since several rays arrive at the receiver (Cerveny 2001). This phenomenon is shown in Figure 67, where multipathing occurs for a velocity model with a perturbation strength of 20% .

Another concept, which was not included is scattering. The ray tracing algorithm only works for direct arrivals, and can for example not be used to reconstruct coda waves. The waveform modeling can be further improved by incorporating these effects.

6.4.4 Inversion and Application to Real Data

In this thesis the focus was waveform modeling using P-wave data. However, Guilhem et al. (2014) use both P- and S-wave data for their inversion. The modeling
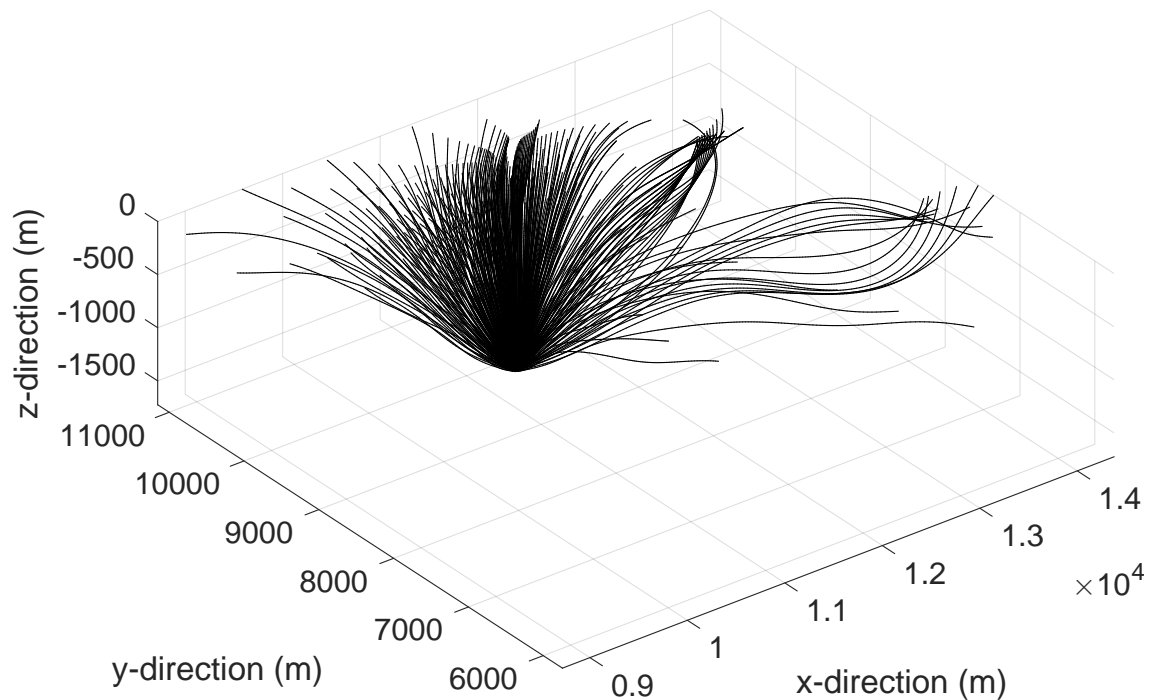
Figure 67: Figure illustrating multipathing. Ray tracing using a velocity model with a perturbation strength of 20% and a correlation length of 500m.

algorithm presented here can be extended to include S-waves.

It would be important to apply the ray tracing and modeling presented here to real data. Applications of these algorithms include travel time tomography, event location and moment tensor inversion. It would also be interesting to compare these results with algorithms that use 1D velocity models. The synthetic results presented here suggests that the use of 3D velocity models is realistic and potentially could lead to significant improvements in geothermal reservoir characterization and management.
.

7 Conclusion

In this thesis I have studied geothermal reservoir characterization using seismic modeling. An overview of seismic studies performed at 15 enhanced geothermal systems was made. It was found that 1D velocity models exist at almost all the geothermal reservoirs. However, this is not the case for 3D velocity models, which exist for only 6 of the reservoirs. I have therefore in this thesis looked at differences in seismic modeling for 1D and 3D velocity models.

The amount of seismic data obtained at a geothermal reservoir can be quite large: tens to hundreds of thousands of events recorded by a hundred or more receivers. Efficient seismic modeling using for example ray tracing, is therefore essential. A ray tracing code was implemented and compared for three different numerical methods: Euler, the midpoint method and fourth order Runge-Kutta. From various, tests it was found that only the fourth order Runge-Kutta and the midpoint method with small time steps provide accurate results. Since the fourth order Runge-Kutta is costly in terms of computation time, I found that the midpoint method with a small time step is the preferred method.

The ray tracing and modeling algorithms could further be improved by incorporating effects such as multipathing and scattering. Also, the effects of anisotropy and attenuation, could be taken into account in the modeling method presented here. Also, Implementation of the ray tracing algorithm in an alternative programing language such as Fortran or C^{++} will significantly reduce computation time.

The ray tracing was used to do waveform modeling for both 1D and 3D velocity models to check trade-offs in terms of travel times, amplitudes and waveforms. The models used were a 1D velocity model for the geothermal reservoir The Geysers in California as given in the literature. The 3D models consisted of this 1D model on which were superimposed 3D perturbations with two different scale lengths. There were significant differences. The most significant deviations were differences in amplitudes and amplitude polarities. Hence, it is suggested that 3D velocity models should be used when doing moment tensor inversions at geothermal reservoirs. It would be interesting to apply the modeling method presented here to real data.

8 References

Aki, K. and P. Richards (1980). *Quantitative seismology.* W. H. Freeman & Co. San Francisco, United Sates.

Asanuma, H., N. Soma, H. Kaieda, Y. Kumano, T. Izumi, K. Tezuka, H. Niitsuma, and D. Wyborn (2005). Microseismic Monitoring of Hydraulic Stimulation at the Australian HDR Project in Cooper Basin. Proceedings World Geothermal Congress 2005.

Baig, A. and F. Dahlen (2004). Traveltime biases in random media and the S-wave discrepancy, *Geophysical Journal International, 158*, 922-938.

Baria, R. (2012). Cornwall's Geophysical Expertise. Available at: `http://www.investincornwall.com/cornwalls-geophysical-expertise/`. Downloaded: 17.04.2016.

Bauer, K., I. Moeck, B. Norden, B. Kallenberg, and M. Weber (2010). Seismic Exploration Around the Geothermal Research Well Gross Schoenebeck (NE German Basin) Combining Tomographic and Reflection Seismic Methods. Proceedings World Geothermal Congress 2010.

Bischoff, M., M. Keyser, T. Plenefisch, U. Wegler, E. Wetzig, L. Ceranna, and C. Bönnemann (2012). Microseismic survey at the geothermal site GeneSys in Hannover, Germany. EGU General Assembly 2012.

Boyce, W. and R. Diprima (2010). *Elementary Differential Equations and Boundary Value Problems.* John Wiley & Sons. Singapore, Singapore.

Breede, K., K. Dzebisashvili, X. Liu, and G. Falcone (2013). A systematic review of enhanced (or engineered) geothermal systems: past, present and future, *Geothermal Energy 2013*, 1-27.

British petroleum (2013). BP energy outlook 2030. Available at: `http://www.bp.com/content/dam/bp/pdf/energy-economics/energy-outlook-2015/bp-energy-outlook-booklet-2013.pdf`. Downloaded: 01.04.2016.

Brogia, A., A. Lazzarottoa, D. Liottab, and G. Ranalli (2003). Extensional shear zones as imaged by reflection seismic lines: the Larderello geothermal field (central

Italy), *Tectonophysics, 363*, 127-139.

Bundschuh, J. and M. Arriga (2010). *Introduction to the Numerical Modeling of Groundwater and Geothermal Systems: Fundamentals of Mass, Energy and Solute Transport in Poroelastic Rocks (Multiphysics Modeling)*. CRC Press. Boca Raton, United States.

Center Research Institute of Electric Power Industry (2006). Evaluation of the first-stage reservoir in the Australian Hot Dry Rock geothermal energy development beneath the Cooper Basin. Available at: `https://books.google.no/books?isbn=4862161901`. Downloaded: 20.04.2016.

Cerveny, V. (2001). *Seismic Ray Theory*. Cambridge University Press. New York, United States.

Chapman, C. (2004). *Fundamentals of Seismic Wave Propagation*. Cambridge University Press. New York, United States.

Charlety, J., N. Cuenot, C. Dorbath, and L. Dorbath (2006). Tomographic study of the seismic velocity at the Soultz-sous-Forets EGS/HDR site. *Geothermics, 35*, 532-543.

Crosby, D. and I. Calman (1996). Seismic Techniques in Geothermal Areas. Proceedings Eighteenth NZ Geothermal Workshop.

Cuenot, N., C. Dorbath, and L. Dorbath (2008). Analysis of the Microseismicity Induced by Fluid Injections at the EGS Site of Soultz-sous-Forets (Alsace, France): Implications for the Characterization of the Geothermal Reservoir Properties. *Pure and Applied Geophysics, 165*, 797-828.

Dahlen, F., S. Hung, and G. Nolet (2000). Frechet kernels for finite-frequency travel times, *Geophysical Journal International, 153*, 157-274.

Dahlen, F. and J. Tromp (1998). *Theoretical Global Seismology*. Princeton University Press. Princeton, United States.

Davatzes, N., K. Feigl, R. Mellors, W. Foxall, H. Wang, and P. Drakos (2013). Preliminary investigations of reservoir dynamics monitored through combined sur-

face deformation and micro-earthquake activity: Brady's Geothermal Field, Nevada. Thirty-Eighth Workshop on Geothermal Reservoir Engineering.

Denlinger, R. and R. Kovach (1981). Seismic-Reflection Investigations at Castle Rock Springs In The Geysers Geothermal Area. *U.S. Geological Survey Professional Paper, 1141*, 117-128.

Department of Energy & Climate Change (2013). Deep geothermal review study. Available at: `https://www.gov.uk/government/uploads/system/uploads/attachment_data/file/251943/Deep_Geothermal_Review_Study_Final_Report_Final.pdf`. Downloaded: 15.04.2016.

DeSanto, J.A. (1992). *Scalar Wave Theory: Green's Functions and Applications.* Springer-Verlag. Heidelberg, Germany.

Drakos, P. (2010). Desert Peak EGS project [PowerPoint presentation]. Available at: `http://energy.gov/sites/prod/files/2014/02/f7/egs_drakos_desert_peak.pdf`. Downloaded: 16.04.2016.

Ehrlich, R. (2013). *Renewable energy: A first course.* CRC press. Boca Raton, United States.

Feng, Q. and J. Lees (1998). Microseismicity, stress, and fracture in the Coso geothermal field, California. *Tectonophysics, 289*, 221-238.

Fritsch, F. and P. Lutz (2006). Power Production at Soultz [PowerPointPresentation]. Available at: `http://engine.brgm.fr/web-offlines/conference-Electricity_generation_from_Enhanced_Geothermal_Systems_-_Strasbourg,_France,_Workshop5/other_contributions/38-slides-0-4_Lutz.pdf`. Downloaded: 18.04.2016.

Garcia, J., M. Walters, J. Beall, C. Hartline, A. Pingol, S. Pistone, and M. Wiright (2012). Overview of the NorthWest Geysers EGS Demonstration Project. Thirty-Seventh Workshop on Geothermal Reservoir Engineering Stanford University.

Gritto, R., S-H. Yoo, and S. Jarpe (2013). Three Dimensional Seismic Tomography at The Geysers Geothermal Field, CA, USA .Thirty-eighth Workshop on Geothermal Reservoir Engineering Stanford University.

Guilhem, A., L. Hutchings, D. Dreger, and L.R Johnson (2014). Moment tensor inversions of M∼3 earthquakes in The Geysers geothermal fields, California. *Journal of Geophysical Research Solid Earth, 119*, 2121-2137.

Häring, M., F. Ladner, U. Schanz, and T. Spillmann (2007). Deep Heat Mining Basel, Preliminary Results. European Geothermal Conference.

Häring, M., U. Schanz, F. Ladner, and B. Dyer (2008). Characterisation of the Basel 1 enhanced geothermal system. *Geothermics, 37*, 469-495.

Heimlich, C., N. Gourmelen, F. Masson, J. Schmittbuhl, S. Kim, and J. Azzola (2015). Uplift around the geothermal power plant of Landau (Germany) as observed by InSAR monitoring. *Geothermal Energy 2015*, 1-12.

Hirschberg, S., S. Wiemer, and P. Burgherr (2015). *Energy from the Earth: Deep Geothermal as a Resource for the Future?* Centre for Technology Assessment. Zürich, Switzerland.

Hutchings, L., B. Bonner, and A. Singh (2014). Micro-earthquake analysis for reservoir properties at the Prati-32 injection test, The Geysers, California. Proceeding, Geothermal Resources Council.

Johnson, L.R. (2014). A source model for induced earthquakes at The Geysers geothermal reservoir. *Pure Applied Geophysics, 171*, 1625-1640.

Johnson, L.R. (2014). Source mechanisms for induced earthquakes at The Geysers geothermal reservoir. *Pure Applied Geophysics, 171*, 1641-1668.

Jost, M. and R. Herrman (1989). A student's guide to and review of moment tensors. *Seismological Research Letters, 60,* 37-57.

Khair, H.A and D. Cooke (2015). Seismic Mapping and Geomechanical Analyses of Faults within Deep Hot Granites, a Workflow for Enhanced Geothermal System Projects. Proceedings World Geothermal Congress 2015.

Kincaid, D. and E. Cheney (2002). *Numerical analysis: mathematics of scientific computing.* Amer Mathematical Society. Rhode Island, United States.

Kind, F., D. Faeh, E. Zechner, P. Huggenberger, and D. Giardini (2001). A 3D Seismic Velocity Reference Model for the City of Basel. American Geophysical Union Fall Meeting 2001.

Krüger, F. and T. Dahm (2014). Moment tensor inversion and moment tensor interpretation. Information sheet.

Küperkoch, L. (2014). Working Towards Highly Accurate Microseismic Event locations at Insheim Geothermal site (Germany)[PowerPointPresentation]. Available at: `http://www.geothermal-energy.org/fileadmin/user_upload/documents/2014-09_Reservoir_Monitoring_IGA_Academy/L_Kueperkoch_low_resolution.pdf`. Downloaded: 16.04.2016.

Kwiatek, G., M. Bohnhoff, G. Dresen, A. Schulze, T. Schulte, G. Zimmermann, and E. Huenges (2010). Microseismicity induced during fluid-injection: A Case Study from the Geothermal Site at Groß Schönebeck, North German Basin. *Acta Geophysica, 58*, 995-1020.

Kwiatek, G., F. Bulut, M. Bohnhoff, and G. Dresen (2012). High-resolution analysis of microseismicity related to hydraulic stimulation in the Berlin Geothermal Field, El Salvador [PowerPointPresentation]. Available at: `http://www.geophys.uni-stuttgart.de/agis/images/presentations/W2%20Kwiatek.pdf`. Downloaded: 16.04.2016.

Madariaga, R. (2007). Seismic Source Theory. *Treatise on Geophysics, 4*, 59-82.

Majer, E.L. (2003). 3-D Seismic Methods for Geothermal Reservoir Exploration and Assessment-Summary. *Department of Energy's (DOE) Office of Scientific and Technical Information*, 33.

Majer, E.L., T. McEvilly, F. Eastwood, and L. Mayer (1988). Fracture detection using P-wave and S-wave vertical seismic profiling at The Geysers. *Geophysics, 53*, 76-84.

Massachusetts Institute of Technology (2006). The Future of Geothermal energy. Available at: `https://mitei.mit.edu/system/files/geothermal-energy-full.pdf`. Downloaded: 02.06.2015.

Matteis, R., T. Vanorio, B. Ciulli, and A. Zollo (2003). 3D Velocity Tomographic Study of the Larderello Geothermal System, Tuscany-Italy. *EUG Joint Assembly.*

Monterrosa, M. (2012). Sustainability Analysis of the Berlin Geothermal Field, El Salvador. *Scandinavian Simulation and Modelling Society Conference Reykjavik, Iceland.*

Morse, P. M. and H. Feshbach (1953). *Methods of Theoretical Physics.* Feshbach Publishing. New York, United States.

Nolet, G. (2008). *A Breviary of Seismic Tomography: Imaging the Interior of the Earth and Sun.* Cambridge University Press. Cambridge, England.

Obermann, A., T. Kraft, E. Larose, and S. Wiemer (2015). Potential of ambient seismic noise techniques to monitor the St.Gallen geothermal site (Switzerland). *Journal of Geophysical Research: Solid Earth, 120,* 4301-4316 .

Oye, V., J. Albaric, N. Langet, I. Lecomte, M. Messeiller, and L. Reid (2012). Microseismic monitoring of the hydraulic stimulation at the Paralana enhanced geothermal system, South Australia. *First Break, 30,* 91-95.

Place, J., M. Diraison, C. Naville, Y. Geraud, M. Schaming, and C. Dezayes (2008). Decoupling of deformation in the Upper Rhine Graben sediments. Seismic reflection and diffraction on 3-component Vertical Seismic Profiling (Soultz-sous-Forets area). *Geoscience, 342,* 575-586.

Press, W., S. Teukolsky, W. Vetterling, and B. Flannery (1992). *Numerical Recipes in Fortran: The Art of Scientific Computing.* Cambridge University Press. New York, United States.

Sethian, J.R. (1999). *Level Set Methods and Fast Marching Methods: Evolving Interfaces in Computational Geometry, Fluid Mechanics, Computer Vision, and Materials Science.* Cambridge University Press. Cambridge, England.

Scott, S., T. Driesner, and P. Weis (2015). Geologic controls on supercritical geothermal resources above magmatic intrusions. *Nature Communications, 6.*

Snieder, R. (2001). General theory of elastic wave scattering. *Pure and Applied*

Science, 528-542.

Stein, S. and M. Wysession (2002). *An introduction to seismology, earthquakes, and earth structure*. Blackwell publishing. Oxford, England.

Tester, W.T., E. Drake, M. Driscoll, M. Golay, and W. Peters (2005). *Sustainable energy*. Massachusetts Institute of Technology. Massachusetts, United States.

Unruh, J., S. Pullammanappallil, W. Honjas, and F. Monastero (2001). New Seismic Imaging of the Coso Geothermal Field, Eastern California. Stanford Geothermal Workshop.

U.S department of energy (2010). Geothermal technologies program, Geothermal Energy Production with Co-produced and Geopressured Resources. Available at: `http://www.nrel.gov/docs/fy10osti/47523.pdf`. Downloaded: 24.04.2016.

Vasterling, M., U. Wegler, A. Bruestle and J. Becker (2016). Real time monitoring of induced seismicity in the Insheim and Landau deep geothermal reservoirs, Upper Rhine Graben, using the new SeisComP3 cross-correlation detector. *Geophysical Research Abstracts, 18*.

Yang, Y., M. Ritzwoller, and C. Jones (2010). Subsurface Characterization of the Coso Geothermal Field and Surroundings by Ambient Noise Tomography. *Geochemistry, Geophysics, and Geosystems, 1*.

9 Appendix

The remaining results from the comparison between the three numerical methods
for the two-point ray tracing in chapter 4 are shown in this appendix. Most of the
figures are for Euler's method, which is the worst of the three ray tracing methods.

9.1 Two-Point Ray Tracing: 1D Velocity Model

The figures in this subsection show results for the two-point ray tracing when using a
1D velocity model. All the figures in this subsection are for Euler's method. Euler's
method generally shows larger errors than the midpoint method (section 4.5.1).

Figure 68: Travel time differences for Euler's method vs. fourth order Runge-Kutta
as computed using the 1D velocity model.
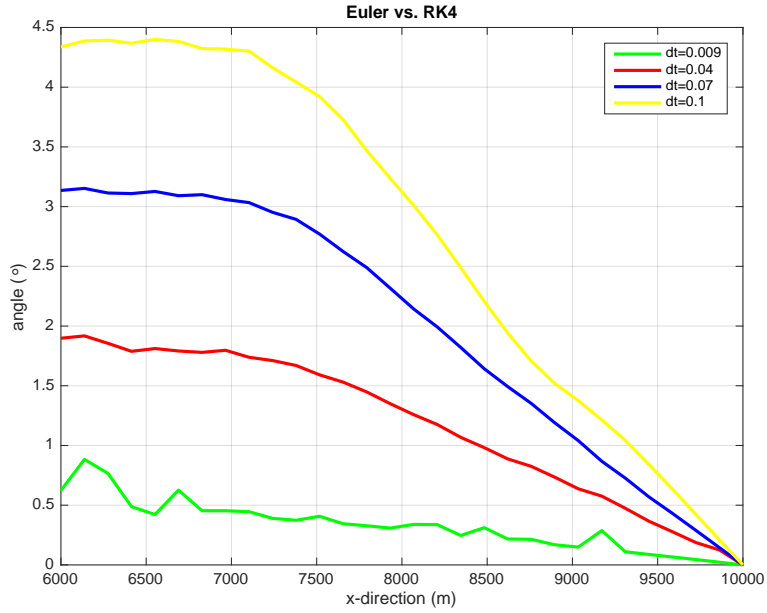
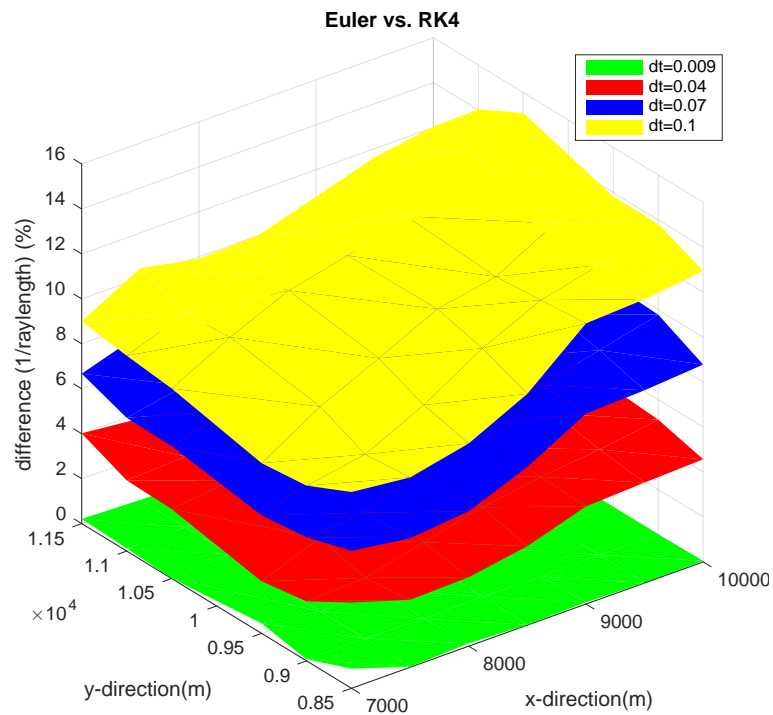Figure 69: Angle between slowness vectors for Euler's method vs. fourth order Runge-Kutta as computed using the 1D velocity model.
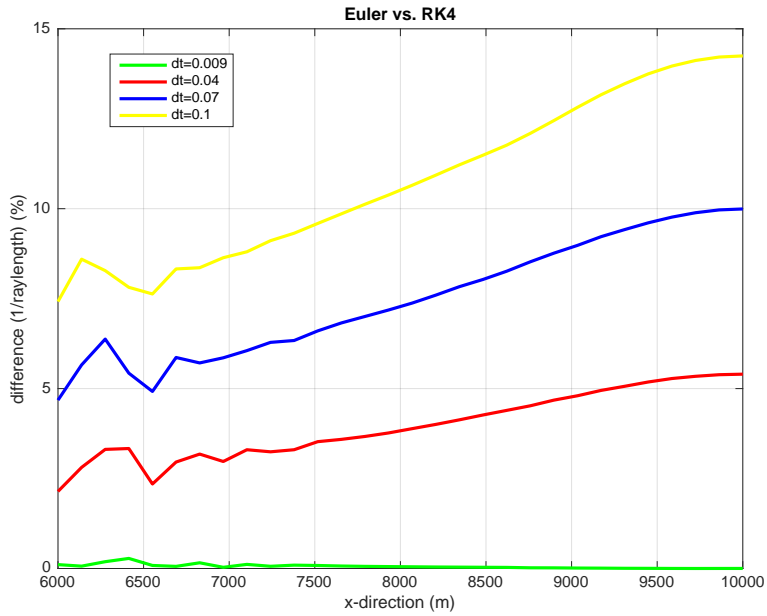
Figure 70: Amplitude differences for Euler's method vs. fourth order Runge-Kutta as computed using the 1D velocity model.
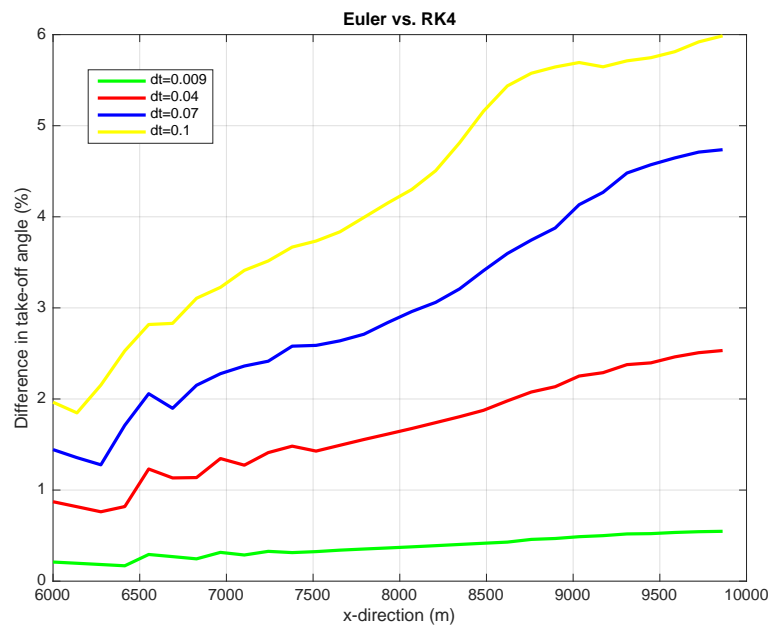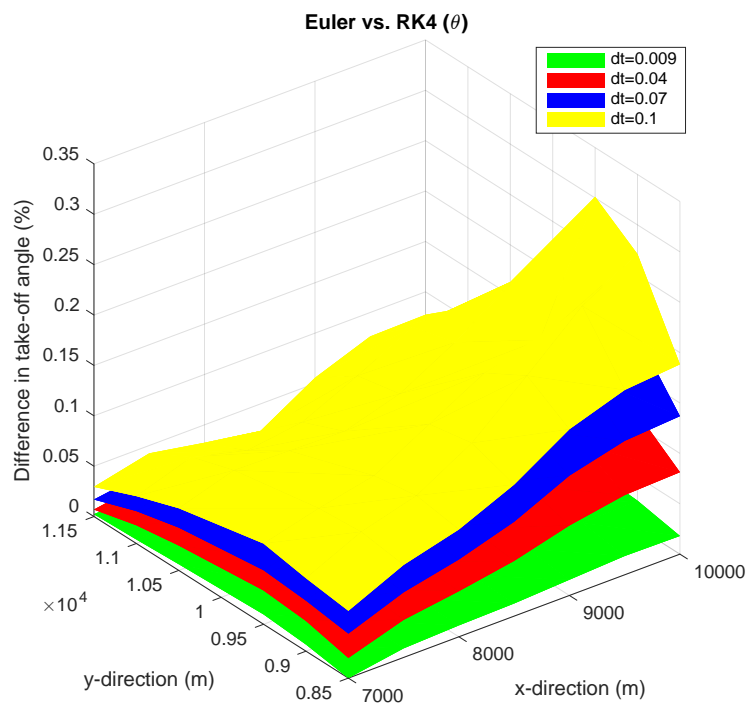
Figure 71: Differences in takeoff angle in for Euler's method vs. fourth order Runge-Kutta as computed using the 1D velocity model.

9.2   Two-Point Ray Tracing: Large Scale 3D Velocity Model

The figures in this subsection show results for the two-point ray tracing when using the large scale 3D velocity model. Euler's method generally shows larger errors than the midpoint method (section 4.5.2).
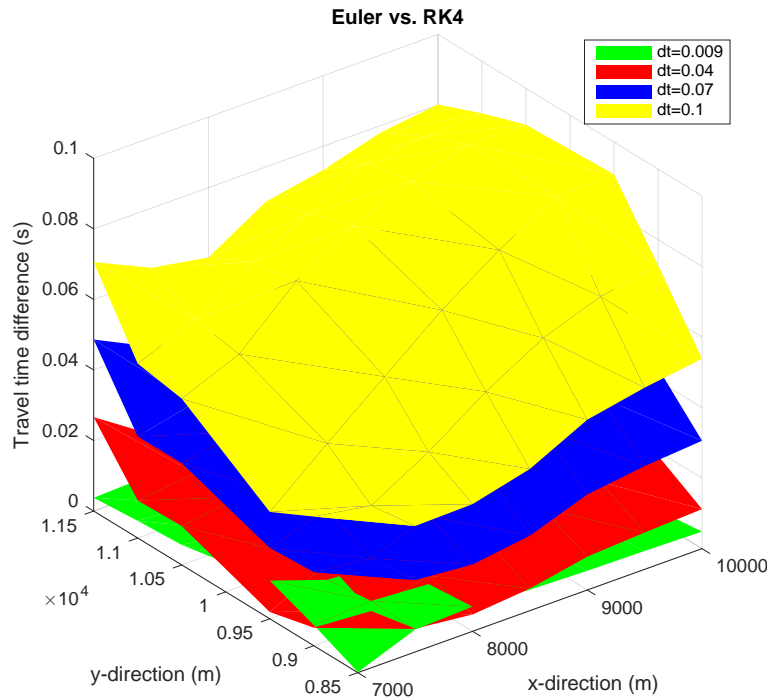
Figure 72: Travel time differences for Euler's method vs. fourth order Runge-Kutta as computed using the large scale 3D perturbation velocity model.
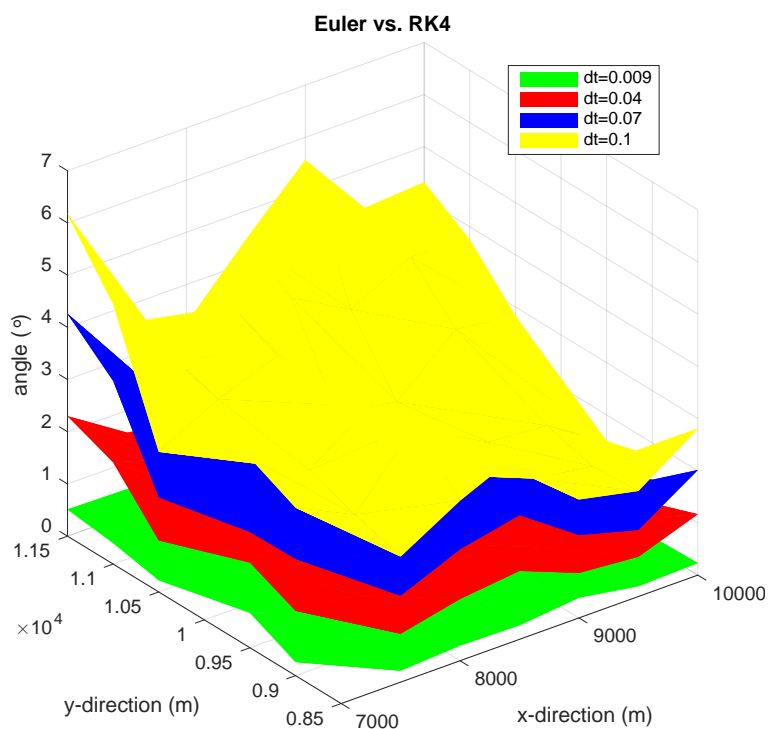
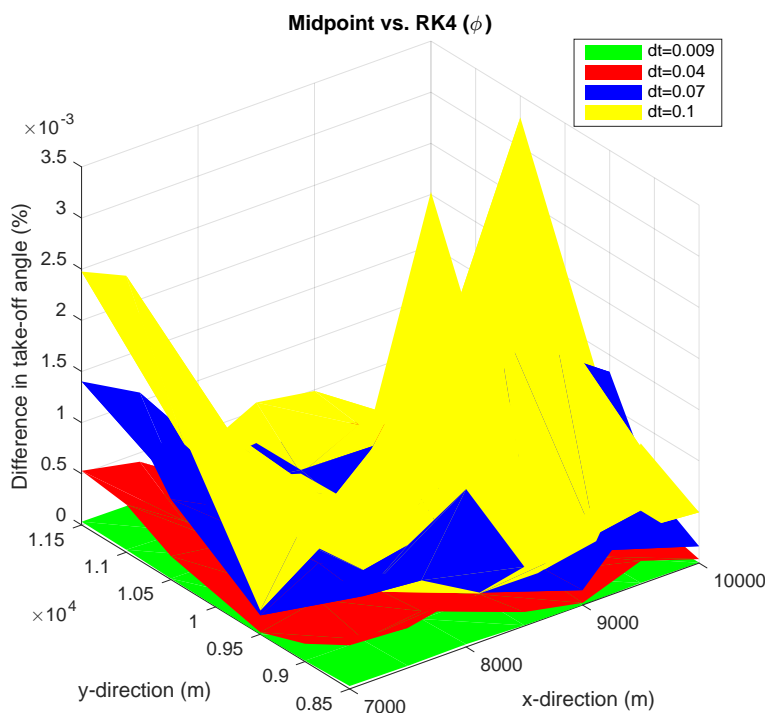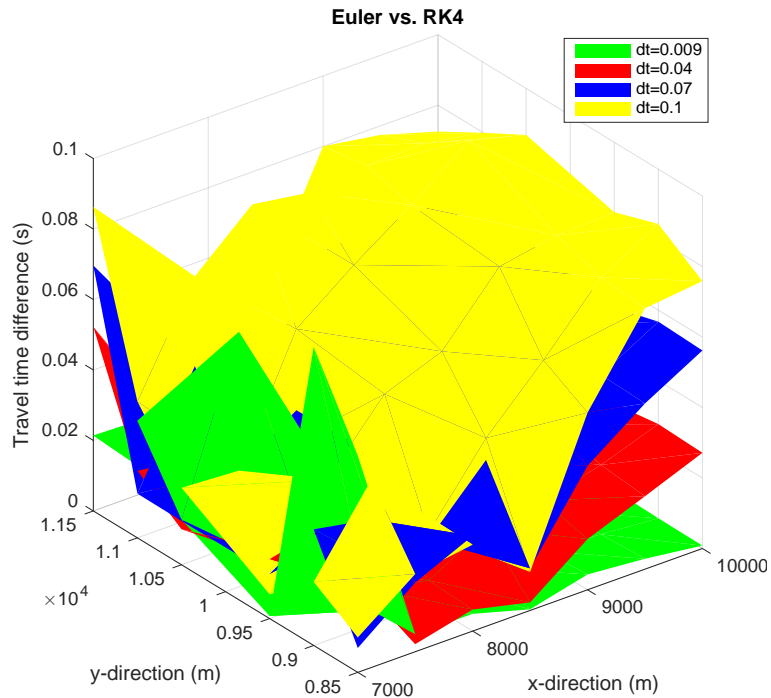Figure 73: Angle between slowness vectors for Euler's method vs. fourth order Runge-Kutta as computed using the large scale 3D perturbation velocity model.

Figure 74: Amplitude differences for Euler's method vs. fourth order Runge-Kutta as computed using the large scale 3D perturbation velocity model.

Figure 75: Differences in θ for Euler's method vs. fourth order Runge-Kutta as computed using the large scale 3D perturbation velocity model.
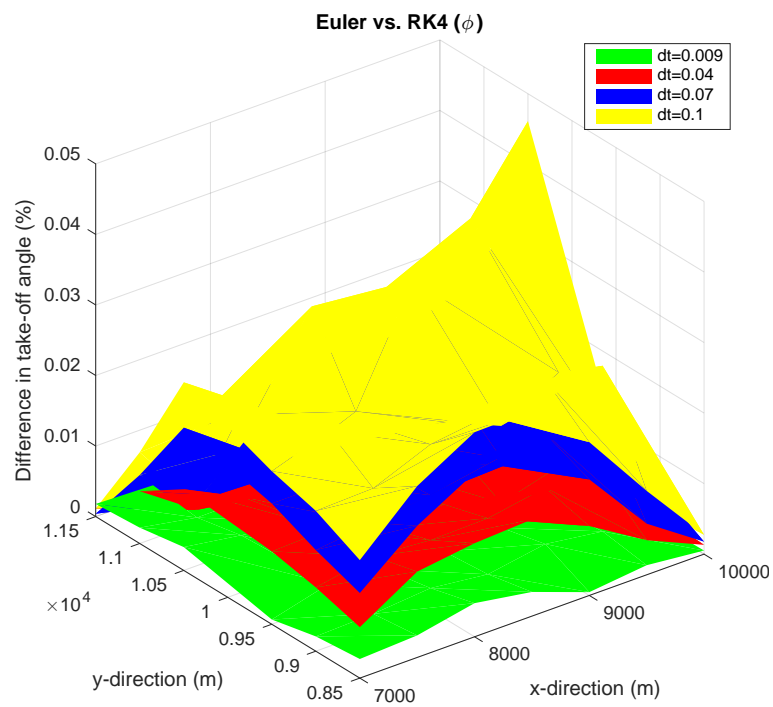
Figure 76: Differences in ϕ for Euler's method vs. fourth order Runge-Kutta as computed using the large scale 3D perturbation velocity model.
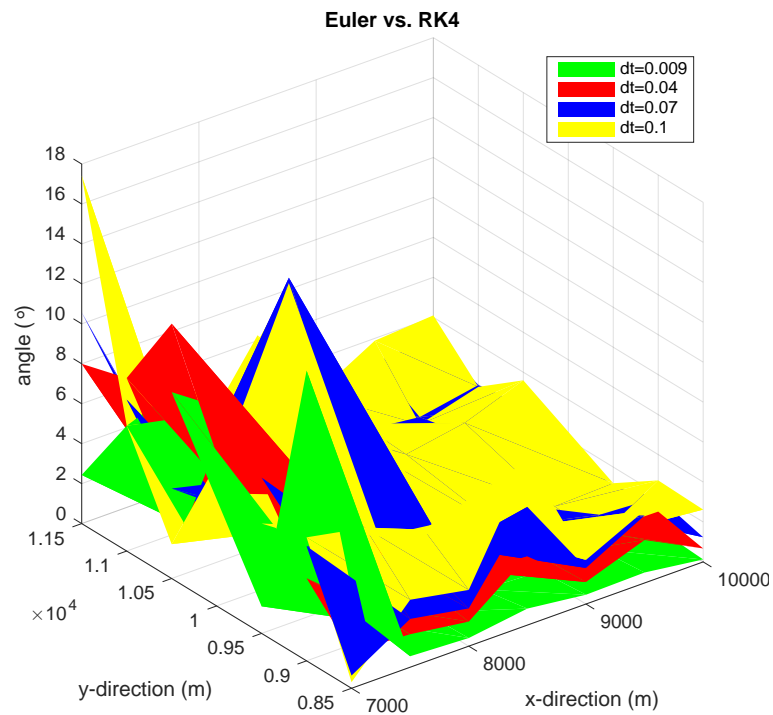
Figure 77: Differences in ϕ for the midpoint method vs. fourth order Runge-Kutta as computed using the large scale 3D perturbation velocity model.

9.3   Two-Point Ray Tracing: Small Scale 3D velocity Model

The figures in this subsection show results for the two-point ray tracing when using the small scale 3D velocity model. Euler's method generally shows larger errors than the midpoint method (section 4.5.3).

Figure 78: Travel time differences for Euler's method vs. fourth order Runge-Kutta as computed using the small scale 3D perturbation velocity model.

Figure 79: Angle between slowness vectors for Euler's method vs. fourth order Runge-Kutta as computed using the small scale 3D perturbation velocity model.
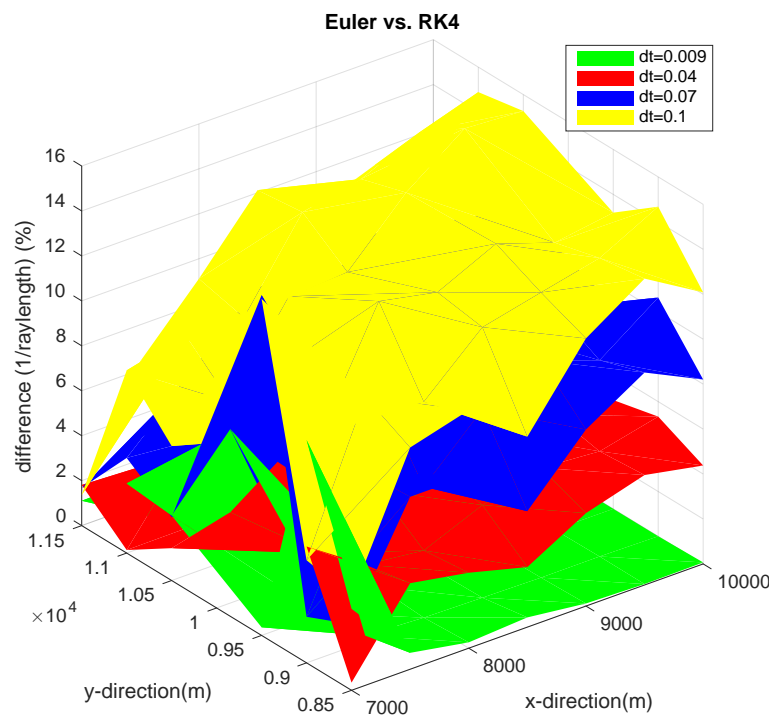
Figure 80: Differences in amplitude (1/raylength) for Euler's method vs. fourth order Runge-Kutta as computed using the small scale 3D perturbation velocity model.
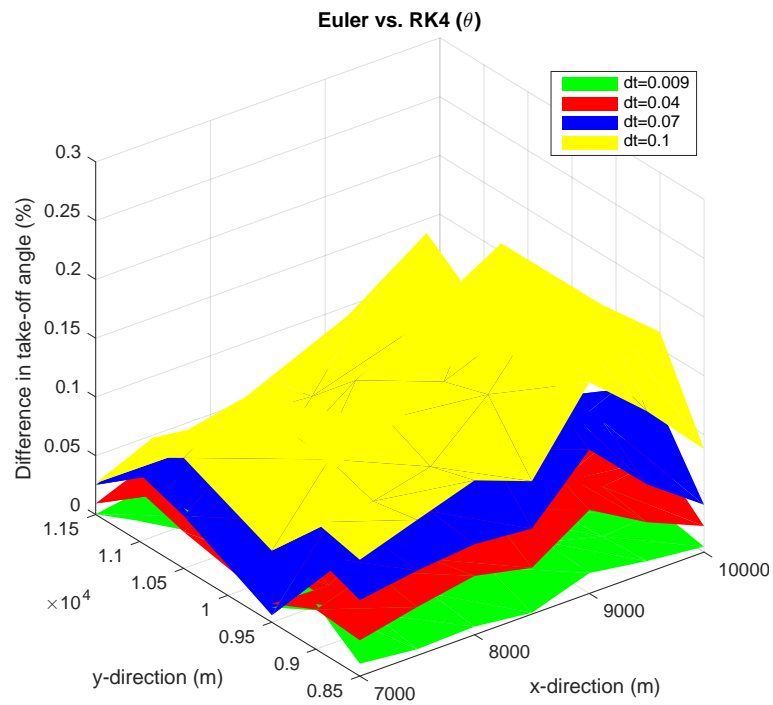
Figure 81: Differences in θ for Euler's method vs. fourth order Runge-Kutta as computed using the small scale 3D perturbation velocity model.
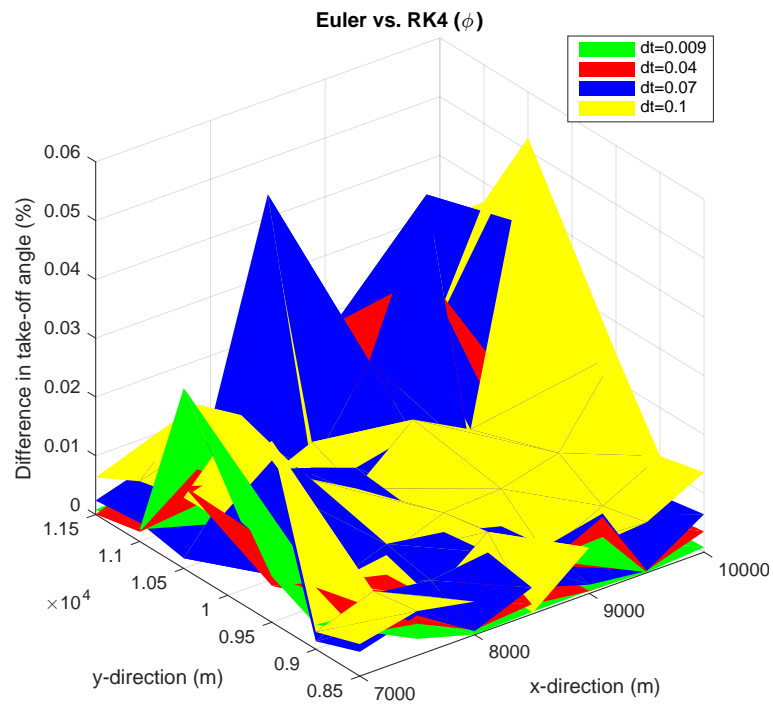
Figure 82: Differences in ϕ for Euler's method vs. fourth order Runge-Kutta as computed using the small scale 3D perturbation velocity model.
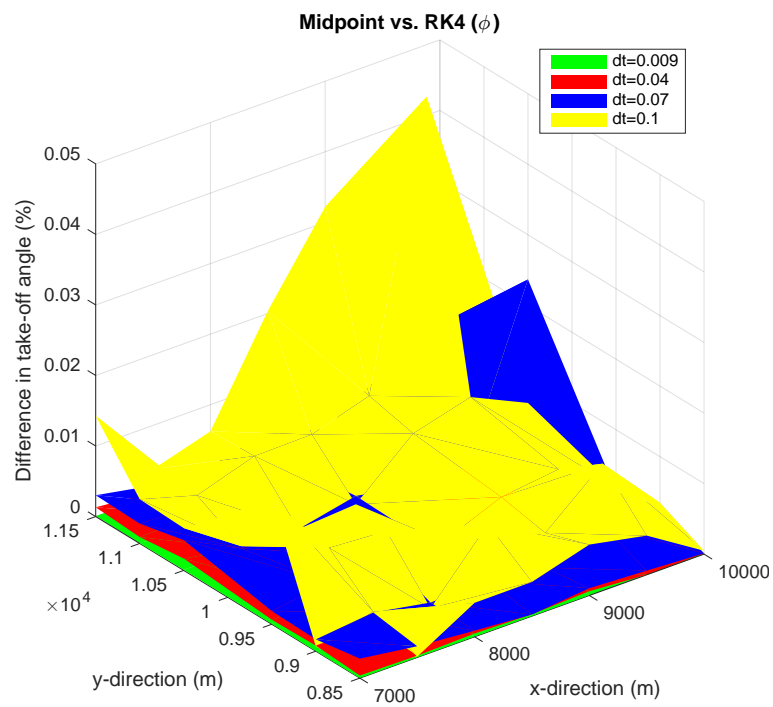
Figure 83: Differences in ϕ for the midpoint method vs. fourth order Runge-Kutta as computed using the small scale 3D perturbation velocity model.